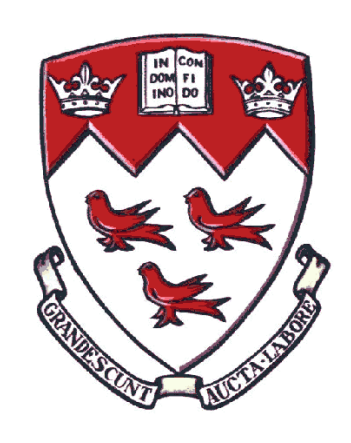
# Spectral Engineering of Dye Sensitized Solar Cells Through Integration of NaYF<sub>4</sub>:Yb<sup>3+</sup>,Er<sup>3+</sup> Upconversion Nanomaterials



Department of Mining and Materials Engineering

McGill University

Montreal, QC, Canada

August 2013

A thesis submitted to McGill University in partial fulfillment of the requirements of the degree of Master of Engineering

© Nathan Dyck, 2013

#### **Abstract**

The scope of this thesis is to investigate the upconversion properties of NaYF<sub>4</sub>:Yb,Er nanomaterials and to optimize their integration into dye sensitized solar cells (DSSCs), a promising new photovoltaic technology. NaYF<sub>4</sub>:Yb,Er converts near infrared light, normally not absorbed by DSSCs, to visible light, therefore potentially increasing the efficiency of the solar cells.

This thesis is manuscript-based, with two primary studies. The first study focuses on optimization and maximization of the upconversion properties of NaYF4:Yb,Er micro and nanophosphors through annealing. As these materials are intended for integration into DSSCs, small particle sizes are preferable; however, small sized upconversion phosphors generally suffer from lower upconversion. Through optimization, different sized (300 nm, 700 nm, and 2.3  $\mu$ m) NaYF4:Yb,Er crystals were produced and successfully annealed without particle size and shape loss while simultaneously maximizing their upconversion luminescence by several orders of magnitude. Quantum yields were achieved (2.5%) that approach that of similar bulk materials.

The second study focuses on integration of the 300 nm UC crystals into DSSCs as an internal scattering layer, aiming to serve the dual purpose of increasing light absorption through scattering and upconversion. Nanocomposite NaYF<sub>4</sub>:Yb,Er@TiO<sub>2</sub> ("core-shell" type) materials were synthesized for this purpose. When integrated as an internal layer in the DSSC, the influence of the  $TiO_2$  shell on the normal electrical functioning of the cells is important. Integration of pure NaYF<sub>4</sub>:Yb,Er materials severely interferes with the cell's normal operation, decreasing overall performance, however when the fraction of  $TiO_2$  in the upconversion material is appropriate, a relative increase of 16% in power conversion is accomplished. This increase was attributed entirely to scattering with negligible contribution from upconversion under standard solar illumination.

#### Résumé

Le but de cette thèse est d'étudier les propriétés de conversion ascendante des nanomatériaux NaYF4:Yb, Er et d'optimiser leur intégration dans des cellules à pigment photosensible (DSSC), une nouvelle technologie photovoltaïque prometteuse. NaYF4:Yb, Er convertit la lumière infrarouge, qui normalement n'est pas absorbée par les DSSCs, en lumière visible, donc elle a le potentiel d'augmenter l'efficacité des cellules solaires.

Ce manuscrit décrit deux études principales. La première étude se concentre sur l'optimisation et la maximisation par recuit des propriétés de conversion ascendante des NaYF4:Yb, Er micro et nanophosphors. Comme ces matériaux sont destinés à l'intégration dans les DSSCs, des petites tailles sont préférable, cependant les phosphores de petite taille souffrent généralement d'une faible conversion ascendante. Grâce à l'optimisation, des particules NaYF4:Yb, Er avec des tailles de 300 nm ont été produites. Par recuit, la taille des particules et leur forme ont été maintenus et la conversion ascendante a été augmentée de plusieurs ordres de grandeur, pour atteindre une efficacité de 2,5%, proche de l'efficacité obtenue par des matériaux massifs de composition similaire.

La deuxième étude se concentre sur l'intégration de ces matériaux comme couche de diffusion interne dans les DSSCs, pour augmenter l'absorption de la lumière par diffusion et conversion ascendante de celle-ci. Des matériaux nanocomposites NaYF4:Yb,Er@TiO2 ont été synthétisés. Comprendre l'influence de celle-ci sur le fonctionnement électrique normale des cellules est important. L'intégration des matériaux NaYF4:Yb,Er purs interfère grandement avec le fonctionnement normal de la cellule, ce qui diminue la performance. Cependant, quand la fraction de TiO2 dans le matériau de conversion ascendante est appropriée, une augmentation relative de 16% dans la conversion d'énergie est obtenue. Cette augmentation est entièrement attribuable à la diffusion avec une contribution négligeable de la conversion ascendante.

## **Acknowledgements**

I would like to acknowledge a number of people who have supported me throughout the course of my degree at McGill.

First, I would like to thank my supervisor, Prof. George Demopoulos, for supporting my research and guiding me throughout the course of my degree. He has been incredibly present, involved in the details and direction of my research, always available to help. I would also like to thank him for sending me to Colorado and Victoria, where I learned valuable characterization techniques for my research.

I would like to acknowledge the entire HydroMET research group (Christoph, Matt, Ivonne, Jessica, Nima, Micah, Jay, Renaud, Amrita, Nesli, Marie-Pier, Marie-Christine, Thomas, Hassane) for making my day-to-day experience at McGill so enjoyable. I am extremely grateful for the open and welcoming environment that has been present within the group. I would especially like to thank Nima for being a constant guide and source of direction with regards to DSSC fabrication and testing, and Hassane for guiding me during the initial stages of the upconversion material synthesis and characterization.

I would like to thank my parents who have supported me all throughout my studies in any way possible. I would especially like to thank my wife, Melissa. She has supported me throughout my degree, and is a big reason why I chose McGill in the first place. Her love and encouragement has been a great help throughout this time, and I know she wants to see me succeed.

Finally, I would like to thank God, who in His infinite patience and grace has blessed me with the intellect and support structure to get where I am today. My aim, as flawed as it is, is to bring glory to His name.

Contributions of Authors and Co-Authors of Works intended for

**Publication in this Thesis** 

Nathan Dyck, Frank C. J. M. van Veggel, George P. Demopoulos, "Size-Dependant

Maximization of Upconversion Efficiency of Citrate-Stabilized β-phase

NaYF<sub>4</sub>:Yb<sup>3+</sup>,Er<sup>3+</sup> Crystals via Annealing." ACS Applied Materials and Interfaces.

Submitted. 2013

Nathan Dyck, George P. Demopoulos, "Integration of Upconverting β-

NaYF<sub>4</sub>:Yb<sup>3+</sup>,Er<sup>3+</sup>@TiO<sub>2</sub> Nanocomposites as Scattering Layers in Dye-Sensitized Solar

Cells" Progress in Photovoltaics: Research and Applications. Submitted. 2013

In all works presented, the first author produced all materials and conducted all

necessary characterization. Prof. van Veggel provided the equipment and guidance

necessary for performing absolute quantum yield measurements in the first

publication and also provided guidance with the discussion of results. Prof.

Demopoulos provided funding and equipment for all materials and characterization

not already mentioned, and also filled the comprehensive supervisory role on both

publications.

The accuracy of the above statements is attested by the student's supervisor.

George P. Demopoulos

Frank C. J. M. van Veggel

iv

# **Table of Contents**

Abstract	1
Résumé	ii
Acknowledgements	iii
Contributions of Authors and Co-Authors of Works intended for Publicatio	
Thesis	
Table of Contents	
List of Figures	viii
List of Tables	xi
Chapter 1: Introduction	1
1.1 Motivation	1
1.2 Objectives and Thesis Layout	2
1.3 References	3
Chapter 2: Literature Review	4
2.1 Introduction	4
2.1.1 Dye-Sensitized Solar Cells	5
2.1.2 Spectral Engineering by Upconversion	7
2.2 Physics of Upconversion Mechanism	7
2.2.1 Lanthanide Ion Upconversion	7
2.2.1.1 Energy Transfer Upconversion (ETU)	8
2.2.1.2 Other Lanthanide Upconversion Mechanisms	13
2.2.1.3 Effect of the Host Material	14
2.2.2 Organic Molecule Upconversion: Triplet-Triplet Annihilation	16
2.3 Current Upconversion Materials and their Applications in Solar Cells	17
2.3.1 Single Ion-Doped Materials	17
2.3.2 Cooperative Ion-Doped Materials	18
2.3.2.1 Yb³+, Er³+ Pair	18
2.3.2.2 Yb³+, Tm³+ Pair	21
2.3.3 Available Host Materials for Lanthanide Doning	22

2	.3.4	Available Materials for Organic Upconversion	23
2.4	R	Review of NaYF4 Synthesis Procedures	25
2	.4.1	Solid-State Methods	26
2	.4.2	Solution-Based Methods	27
	2.4.	-2.1 Co-precipitation	27
	2.4.	.2.2 Hydrothermal/Solvothermal Synthesis	28
	2.4.	.2.3 Thermal Decomposition of Trifluoroacetates	29
	2.4.	.2.4 High Boiling-Point Solvents	30
2.5	R	References	32
Chapt	er 3:	: Size-Dependent Maximization of Upconversion Efficie	ncy of Citrate
- Stabil	ized	β-phase NaYF <sub>4</sub> :Yb <sup>3+</sup> ,Er <sup>3+</sup> Crystals via Annealing	-
3.1	A	Abstract	41
3.2	Ir	Introduction	41
3.3	E	Experimental Section	44
3	.3.1	Crystal Synthesis	44
3	.3.2	Characterization	45
3.4	R	Results and Discussion	46
3.5	C	Conclusions	56
3.6	A	Acknowledgments	57
3.7	R	References	58
Chapt	er 4:	: Integration of Upconverting β-NaYF <sub>4</sub> :Yb <sup>3+</sup> ,Er <sup>3+</sup> @TiO <sub>2</sub> N	anocomposites
-		arvesting Layer in Dye-Sensitized Solar Cells	-
4.1		Abstract	
4.2		Introduction	
4.3	E	Experimental Section	64
4	.3.1	Upconverter Synthesis	64
	4.3.	.1.1 NaYF <sub>4</sub> :Yb <sup>3+</sup> ,Er <sup>3+</sup> Synthesis	64
	4.3.	.1.2 UC@TiO <sub>2</sub> Nanocomposite Synthesis	65
4	.3.2	Dye-Sensitized Solar Cell Fabrication	65
4	.3.3	Characterization	66
	4.3.	.3.1 Upconvertor Characterization	66
	4.3.	.3.2 Dye-Sensitized Solar Cell Characterization	67
1. 1.	D	Recults and Discussion	68

4.4	4.1 Upconversion Nanocomposites	68
4.4	4.2 Dye-Sensitized Solar Cell Integration	73
	4.4.2.1 Electrochemical Impedance Spectroscopy (EIS)	77
4.5	Conclusions	80
4.6	Acknowledgments	81
4.7	References	82
Chapte	er 5: Synopsis	87
5.1	Global Conclusions	87
5.2	Recommendations for Future Work	89
5.3	References	89
Append	dix A: Chapter 3 Supporting Information	91
Append	dix B: Chapter 4 Supporting Information	94
Append	dix C: Y <sub>3</sub> Al <sub>5</sub> O <sub>12</sub> :Yb <sup>3+</sup> ,Er <sup>3+</sup> Upconversion Study	96
Append	dix D: Application of External NaYF4:Yb3+,Er3+ Upconversion	on Layers to DSSCs
		100

# **List of Figures**

Figure 2.1: Plots showing (a) the distribution of absorbed solar energy and corresponding losses in single junction solar cells (reproduced from ref. [3]) (DSSC bandgap shown as white broken line), and (b) the spectral response of a DSSC (IPCE, black) plotted with the standard AM1.5 solar spectrum (blue, ASTM G173-03 Reference Spectra Derived from SMARTS v. 2.9.2) as a function of wavelength
Figure 2.2: Schematic illustrating the basic mechanism of charge generation in dye- sensitized solar cells [5]6
Figure 2.3: Simplified overview of the different upconversion mechanisms using fand d ions [8]8
Figure 2.4: Energy level diagram illustrating simple upconversion in a 3-level system. Dashed arrows indicate non-radiative processes, solid arrows indicate radiative processes [9]9
Figure 2.5: Simplified energy level diagram showing sensitizer (left) and activator (right) [8]12
Figure 2.6: Representation of the time resolved luminescence decay of ETU-based upconversion (left) and ESA-based upconversion (right) [10]13
Figure 2.7: Figure illustrating narrower absorption range in chloride host compared with fluoride host [12]15
Figure 2.8: Diagram illustrating the optical processes possible in the $Er^{3+}$ ion system in different host materials [13]15
Figure 2.9: Diagram illustrating transitions leading to upconversion in the organic molecular system [17]17
Figure 2.10: Energy level diagram showing the energy transfer steps in the Yb³+-Er³+ upconversion system. Solid and dashed arrows represent radiative and non-radiative energy transitions respectively. Numbered arrows indicate possible emissive transitions [31]
Figure 2.11: Yb-Tm energy level system showing upconversion from infrared to blue. Solid, dotted, and curly arrows indicate radiative transitions, non-radiative transitions, and multiphonon relaxations respectively. Figure adapted from [15]
Figure 2.12: (a) Absorption and (b) upconverted fluorescence spectra from 3 different organic upconversion systems. System labels are shown at bottom of the figure and correspond to absorption and fluorescence spectra from right to left, respectively [61].

Figure 2.13: Various NaYF <sub>4</sub> :Yb,Er particle types: (a) "bulk" particles by solid state [33], (b) irregular β-crystals by unmodified hydrothermal [67], (c) β-hexagon prisms by citrate-modified hydrothermal [68], (d) β-nanoflower particles be oleic acid hydrothermal [69], (e) α-nanoparticles by trifluoroacetate decomposition [47], (f) β-nanospheres by trifluoroacetate decomposition [70] (g) β-nanorods by mixed hydrothermal [71], (h) β-nanotubes by hydrotherm [72]
Figure 2.14: Illustration showing (a) the general solvothermal reaction mechanism [83] and (b) the transformation mechanism from $\alpha$ to $\beta$ phase [67]2
Figure 3.1: Experimental setup schematic for measuring quantum yield of upconversion crystals4
Figure 3.2: Upconversion emission for samples annealed at different temperature for UC1 (top), UC2 (middle), UC3 (bottom). The log is taken for the integrate peak values, and each gridline represents a decade4
Figure 3.3: XRD results from UC2 showing gradual phase transformation from β to via annealing. Reference patterns are shown for cubic (JCPDS 06-0342) an hexagonal (JCPDS 28-1192) phases4
Figure 3.4: SEM micrographs of different size upconversion crystals showing the effect of annealing temperature on morphology (UC1 left, UC2 middle, UC1 right)
Figure 3.5: TEM micrograph of UC3 crystals annealed at 350 °C for 2 hours5
Figure 3.6: ATR-FTIR transmission spectra of hydrothermally produce upconversion samples including samples annealed at 400 and 500 °C. A spectra were corrected for the ATR effect using the supplied software5
Figure 3.7: Schematic illustrating the changes in particle morphology wit increasing temperature5
Figure 4.1: TEM images of the UC@TiO $_2$ nanocomposite materials showing UC@T particles produced with 3:1 DIW:TEOT ratio (a,b), and UC@T2 particle produced with 6:1 DIW:TEOT ratio (c,d)6
Figure 4.2: Upconversion fluorescence spectra under 980 nm NIR laser illumination showing (a) the difference between the as-prepared UC and the UC@TiC materials, and (b) the difference between the as-prepared UC@T2 materic (spectrum multiplied by 100 for easier visual comparison) and the anneale UC@T2 material
Figure 4.3: Powder XRD results showing the effect of annealing at 450 °C on the uncoated UC material and the UC@TiO $_2$ material. Reference pattern for $\beta$ -NaYl (JCPDS 28-1192) is included and peaks corresponding to $\alpha$ -NaYF $_4$ and TiO (anatase phase) are indicated with markers

Figure 4.4: Current-voltage characteristics for different UC/scattering layers investigated. Inset: current voltage relationship for UC@TiO2 device under 980 nm laser illumination, illustrating proof-of-concept IR function74
Figure 4.5: Incident photon to electron conversion (IPCE) for different UC/scattering layers studied. All measurements were performed under $\sim 1$ sun light bias. Inset: detailed view of device performance in the NIR region75
Figure 4.6: Equivalent circuit used for extraction of solar cell performance parameters, originally developed by Fabregat-Santiago <i>et al.</i> [43], [44]
Figure 4.7: Electrochemical impedance spectroscopy (EIS) of different UC/scattering layers investigated under 1 sun illumination, showing (a) chemical capacitance $C_{\mu}$ , plotted against $V_F$ , (b) chemical capacitance, $C_{\mu}$ , plotted against $V_{ecb}$ , (c) recombination resistance, $R_{rec}$ , plotted against $V_{ecb}$ , and (d) carrier lifetime, $\tau_n$ plotted against $V_{ecb}$ .
Figure A.1: Upconversion fluorescence under NIR (980nm) laser excitation. Data taken from UC1-600 sample
Figure A.2: TGA scan at 20°C/min for UC3 sample. Solid line indicates weight % and dashed line indicates first derivative, showing maximum weight loss at ~372°C93
Figure A.3: Quantum yield raw data for (a) visible upconversion under 50W/cm <sup>2</sup> NIR excitation and (b) NIR laser profile shown for sample (solid line) and reference (dashed line). Data taken from UC3 hydrothermal sample93
Figure B.1: Heating profile for the DSSC annealing process
Figure B.2: Digital photographs illustrating the effect of scattering on the transparency of the DSSCs as observed from the front (photoanode) side and the back (counter electrode) side
Figure C.1: Upconversion fluorescence spectrum under NIR laser illumination (980 nm) for YAG:18%Yb,1%Er annealed at 1200 °C for 2 hours98
Figure C.2: Integrated upconversion fluorescence values for YAG (a,b) Er <sup>3+</sup> doping study and (c,d) Yb <sup>3+</sup> doping study for as-is samples, and samples annealed at 800 and 1000 °C98
Figure D.1: Upconversion fluorescence spectra of annealed samples under NIR laser illumination (980 nm)100
Figure D.2: (a) Schematic illustrating structure of DSSC device and position of the external upconversion (UC) layer, and (b) the JV characteristics of the DSSC devices with proof-of-concept performance under NIR laser illumination shown inset

# **List of Tables**

Table 2.1: $Er^{3+}$ upconversion emission bands under 1.5 $\mu$ m excitation. Table adapted from [14]
Table 2.2: Summary of available host materials in upconversion studies and corresponding lanthanide dopants23
Table 3.1: Hydrothermal synthesis parameters for different size upconversion crystals studied
Table 3.2: Quantum yields for hydrothermal samples and highest emitting, non-agglomerated annealed samples55
Table 4.1: Detailed PV characteristics for different UC/scattering layers studied. All values are an average of multiple cells made under the same conditions, with the standard deviation of each device set listed as the error on each value 73
Table A.1: Raw integrated values for upconverted fluorescence and green-to-red ratios92
Table C.1: Raw integrated intensity values for all YAG:Yb,Er samples studied 97
Table D.1: PV Characteristics of DSSC devices with external upconversion layers .101

## **Chapter 1: Introduction**

#### 1.1 Motivation

Global energy consumption was 135 528 TWh in 2008 corresponding to an average power consumption of 15.5 TW [1]. World energy consumption has been estimated to rise by 47% by year 2035 [2]. Increasing energy demand and climate change pressures are extremely important topics today and will continue to be important in the decades and centuries to come. Over the course of one hour, the sun can provide more energy at the earth's surface than is needed to fulfill the requirements of humanity for an entire year [3]. Even though an extremely large source of power exists in the sun, only about 70GW of installed solar energy capacity exists globally, supplying a very small fraction of the energy we need [4]. The reason for this is due to the high cost of solar-generated electricity (photovoltaics) compared with more conventional methods of production. The high cost of solar electricity can be attributed to high material and fabrication costs coupled with low power conversion efficiency. Increasing conversion efficiency and decreasing material cost are the two primary methods of reducing the cost of solar electricity.

Dye sensitized solar cells (DSSCs) are a relatively new photovoltaic technology [5] that are positioned as a potentially low-cost alternative to classic, single-junction, silicon solar cells. Recently, these types of cells have reached efficiencies of greater than 14% as confirmed by NREL [6]. Given the bandgap position of DSSCs (~1.6eV in N-719, a standard dye [7]), most of the energy losses are due to sub-bandgap photons that cannot be absorbed by the dye. This makes DSSCs a suitable candidate for spectral engineering by upconversion, a process that converts lower energy photons to higher energy photons that can then be absorbed by the solar cell.

Previous research by the McGill HydroMET group demonstrated feasibility of upconversion integration in DSSCs [8], [9], and more recent research revealed the possibility of drastically improving the efficiency of the upconversion process in

NaYF<sub>4</sub>:Yb,Er through annealing [10]. For these reasons, it has been chosen to further investigate these materials.

#### 1.2 Objectives and Thesis Layout

The main objectives of this work are to study the annealing-induced optimization of the upconversion in Yb³+,Er³+ doped NaYF₄ crystals produced by hydrothermal synthesis and to subsequently demonstrate the integration of these materials into DSSC devices. This thesis is presented as a manuscript based thesis with two primary investigations intended for publication in open literature. The first investigation, presented in Chapter 3, outlines efforts to maximize the efficiency of NaYF₄ particles of varying sizes through annealing. Annealing drastically increases the upconversion luminescence, however also alters the particle morphology, which can be important for integration into DSSCs, especially as internal layers. The second investigation, presented in Chapter 4, outlines efforts to integrate the same materials studied in Chapter 3 into an internal layer of DSSC devices. The impact of these layers on all aspects of device functioning is investigated. Additional investigations not intended for publication are also presented briefly in the Appendices.

#### 1.3 References

- [1] BP, "BP Statistical Review of World Energy June 2009," 2009.
- [2] EIA, "Annual Energy Outlook 2012 with Projection to 2035," 2012.
- [3] O. Morton, "Solar energy: a new day dawning? Silicon Valley sunrise.," *Nature*, vol. 443, no. 7107, pp. 19–22, 2006.
- [4] REN21, "Renewables 2012 Global Status Report," 2012.
- [5] B. O'Regan and M. Grätzel, "A low-cost, high-efficiency solar cell based on dye-sensitized colloidal TiO<sub>2</sub> films," *Nature*, vol. 353, no. 6346, pp. 737–740, 1991.
- [6] "Best Research-Cell Efficiencies," *NREL*, 2013. [Online]. Available: http://www.nrel.gov/ncpv/images/efficiency\_chart.jpg. [Accessed: 17-Jun-2013].
- [7] M. Liu, Y. Lu, Z. B. Xie, and G. M. Chow, "Enhancing near-infrared solar cell response using upconverting transparent ceramics," *Solar Energy Materials and Solar Cells*, vol. 95, no. 2, pp. 800–803, 2011.
- [8] G.-B. Shan and G. P. Demopoulos, "Near-infrared sunlight harvesting in dyesensitized solar cells via the insertion of an upconverter-TiO<sub>2</sub> nanocomposite layer.," *Advanced Materials*, vol. 22, no. 39, pp. 4373–7, 2010.
- [9] G.-B. Shan, H. Assaaoudi, and G. P. Demopoulos, "Enhanced Performance of Dye-Sensitized Solar Cells by Utilization of an External, Bifunctional Layer Consisting of Uniform β-NaYF<sub>4</sub>:Er<sup>3+</sup>/Yb<sup>3+</sup> Nanoplatelets," *ACS Applied Materials & Interfaces*, vol. 3, no. 9, pp. 3239–3243, 2011.
- [10] H. Assaaoudi, G.-B. Shan, N. Dyck, and G. P. Demopoulos, "Annealing-induced ultra-efficient NIR-to-VIS upconversion of nano-/micro-scale  $\alpha$  and  $\beta$  NaYF<sub>4</sub>:Er<sup>3+</sup>,Yb<sup>3+</sup> crystals," *CrystEngComm*, vol. 15, no. 23, pp. 4739–4746, 2013.

### **Chapter 2: Literature Review**

In this chapter the basic knowledge for understanding the principles of DSSC operation, and how spectral engineering via upconversion can be useful for increasing the efficiency of such devices is reviewed. The first part will focus on the physics of various upconversion mechanisms, followed by a review of the currently available upconversion materials including the ways in which they have been already applied to solar cell devices; and will finally finish with a review of the synthesis methods for producing NaYF4:Yb,Er, the most efficient near infrared-to-visible upconverting material and the material selected for use in the experimental research undertaken for the purposes of this thesis.

#### 2.1 Introduction

Single junction silicon solar cells, which account for the majority of commercially available cells, have a thermodynamic limit of  $\sim 30\%$  power conversion efficiency as originally calculated by Shockley and Queisser [1]. Research level silicon cells have reached efficiencies of 25% [2] although commercially available modules typically operate closer to 15-18% efficiency. This thermodynamic limitation is based on the assumption that every incoming photon larger than the material's bandgap (Eg) will generate a single electron-hole pair. This gives rise to two primary types of energy loss through the energy conversion process:

- 1. Sub-bandgap losses. Photons with energy less than the absorbing material's bandgap will pass through the material and not be absorbed.
- Thermalization losses: Photons with energy greater than the material's bandgap will lose excess energy to heat as they relax to the conduction band edge.

The amount of energy lost to these two mechanisms will depend on the position of the material's bandgap in relation to the distribution of energy in the solar spectrum. A plot of the energy losses against material band-gap is shown in Figure 2.1 (a). The bandgap at which the sub-bandgap losses equal thermalization losses is

1.25 eV. Therefore materials that have a band gap larger than 1.25 eV lose more energy to sub-bandgap losses, while materials with a bandgap less than 1.25 eV lose more energy to thermalization.

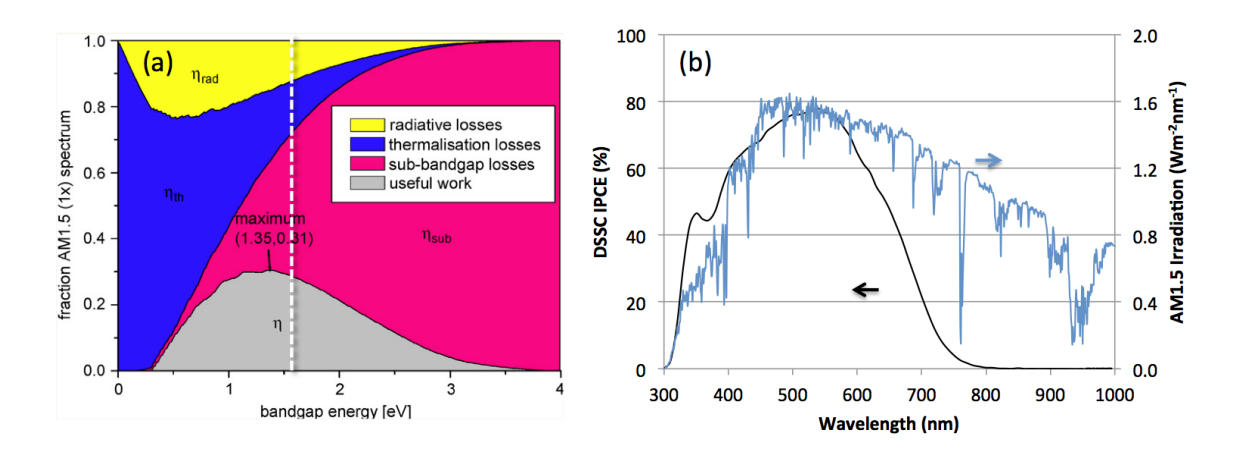


Figure 2.1: Plots showing (a) the distribution of absorbed solar energy and corresponding losses in single junction solar cells (reproduced from ref. [3]) (DSSC bandgap shown as white broken line), and (b) the spectral response of a DSSC (IPCE, black) plotted with the standard AM1.5 solar spectrum (blue, ASTM G173-03 Reference Spectra Derived from SMARTS v. 2.9.2) as a function of wavelength.

#### 2.1.1 Dye-Sensitized Solar Cells

Dye-sensitized solar cells (DSSCs) are a promising new photovoltaic technology originally invented by O'Regan and Grätzel in 1991 [4]. In DSSCs, the light is absorbed by a molecular dye. The molecular dye transfers an excited electron to a network of titanium dioxide, a relatively inexpensive semiconductor material. The electron is then transported through the semiconductor to the photoelectrode interface. The resulting photo-oxidized dye molecule is reduced by an iodide/triodide redox couple, which serves to transport the hole (positive charge) to the counter electrode. A schematic of how a photon generates electric charge in DSSCs is shown in Figure 2.2.

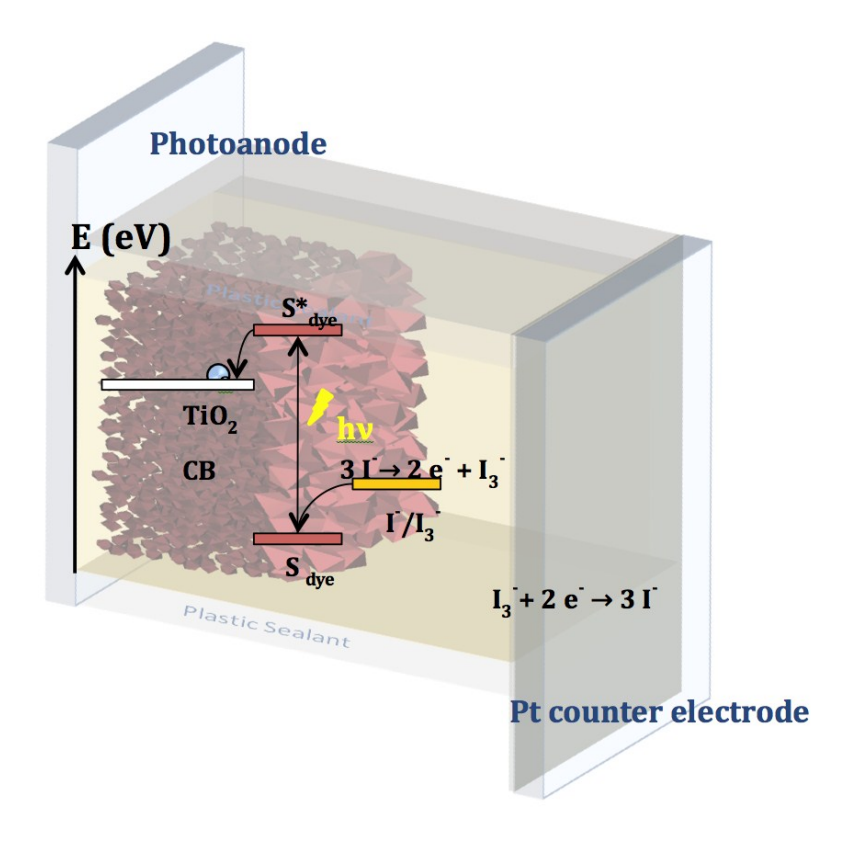


Figure 2.2: Schematic illustrating the basic mechanism of charge generation in dye-sensitized solar cells [5]

For DSSCs, much research has been devoted to developing new molecular dyes, however most research studies as well as the work contained in this thesis still use a red-coloured, ruthenium-based dye known as N-719 as the standard. N-719 has a bandgap (also known as the HOMO/LUMO energy gap) of about 1.6 eV [6]. Assuming that a DSSC's loss mechanisms are similar to single junction semiconductor solar cell with the same band gap, it can be seen from the white dashed line in Figure 2.1(a) that DSSCs lose most of the energy in the solar spectrum due to sub-bandgap losses. The spectral response of a solar cell is given by the incident photon-to-electron conversion efficiency (IPCE), which denotes the number of electrons generated per incident photon at a given wavelength. By plotting a typical DSSC IPCE on the same graph as the standard AM1.5 solar spectrum (incident irradiation at 30° from the zenith) as shown in Figure 2.1(b), it can be easily seen that a great deal of near infrared irradiation (750-1000 nm) is not converted to electrical energy by a DSSC, further demonstrating the loss of sub-

bandgap energy. This makes DSSCs a prime candidate for spectral engineering, generally defined as a method to alter the solar spectrum to better suit the solar cell device.

#### 2.1.2 Spectral Engineering by Upconversion

One way to reduce sub-bandgap energy losses is by photon upconversion. The process for photon upconversion is simple in its underlying principle: the energy from two or more photons is added together to give a single, higher-energy photon  $(hv_1 < hv_2)$ . In the context of solar cells, this means that energy that would otherwise be lost due to transmission can be converted to energy that can be absorbed by the solar cell (as long as  $hv_2 > E_g$  of solar cell absorbing material).

Upconversion is most often accomplished by doping lanthanide element ions into optical host materials. The energy levels of these ions are ideally spaced to absorb light in the infrared region. If the ions can be excited multiple times, subsequent relaxation can result in light emission in the visible or UV regions. Upconversion is also possible via organic molecular systems. A more comprehensive review of the materials used for upconversion is presented in Section 2.3.

#### 2.2 Physics of Upconversion Mechanism

There exist a number of different upconversion mechanisms in which longer wavelength light can be converted into shorter wavelength light.

#### 2.2.1 Lanthanide Ion Upconversion

Most mechanisms of upconversion rely on the discrete energy level spacing found in lanthanide element ions. These ions can be excited by multiple photons into higher excited energy states. Relaxation from these higher excited states can result in emission of photons with higher energy than the original excitation photons. Up until 1966, most upconversion processes were believed to be a result of excited state absorption (ESA) where an already excited ion absorbs a second photon and is excited to a higher energy state. In 1966, Auzel suggested that upconversion could occur via energy transfer between two already excited ions, resulting in one

returning to its ground state and another excited to a higher energy state [7]. The former is known as the sensitizer (S), while the latter is known as the activator (A). These have also been called donors (D) and acceptors (A), respectively, although since these upconversion systems can be used in tandem with semiconductor electronics, this terminology can be confusing and is thus avoided.

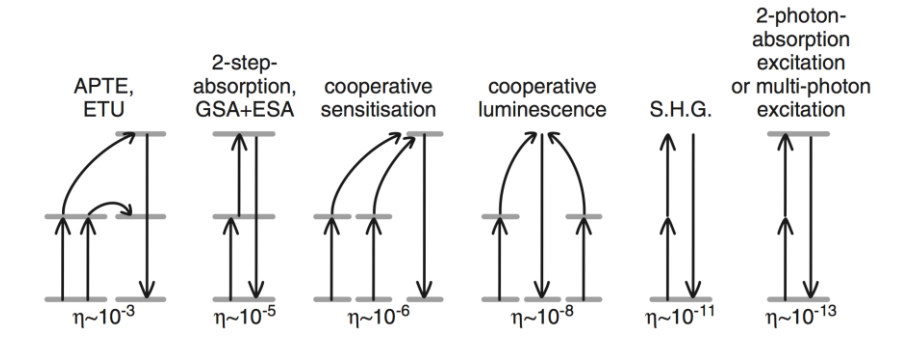


Figure 2.3: Simplified overview of the different upconversion mechanisms using f and d ions [8]

A simplified overview of different upconversion mechanisms in lanthanide-based upconverting materials is shown in Figure 2.3. The figure has the upconversion mechanisms listed in order of decreasing, experimentally observed, conversion efficiency, from left to right. The most efficient upconversion mechanism is known as "addition de photon par transferts d'energie" (APTE) or "energy transfer upconversion" (ETU) and is therefore the focus of most of upconversion literature.

#### 2.2.1.1 Energy Transfer Upconversion (ETU)

ETU is often referred to as GSA/ETU in literature since it requires a ground state absorption step (GSA) and subsequent energy transfer step (ETU). For simplicity, it will be referred to as "ETU" in this review.

All upconversion processes are non-linear, meaning their fluorescence yield does not vary linearly with excitation intensity. The output power as a function of input power can be derived by examining a simple, 3 energy level system, as depicted in Figure 2.4.

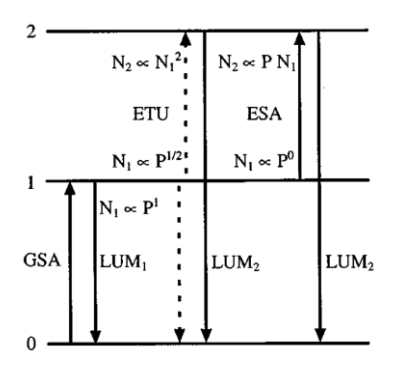


Figure 2.4: Energy level diagram illustrating simple upconversion in a 3-level system. Dashed arrows indicate non-radiative processes, solid arrows indicate radiative processes [9]

This derivation follows Pollnau *et al.* [9] and operates under the following assumptions:

- 1. Constant ground-state population,  $N_0$
- 2. System is pumped by ground state absorption, GSA
- 3. Upconversion occurs by either ETU or ESA (excited-state-absorption)
- 4. The excited states have a finite lifetime, given by  $\tau_i$ , and decay to the ground state, or next-lowest state, described by the rate constant  $A_i = \tau_i^{-1}$

The absorption of the material can be described by the sum of absorptions resulting from transitions between states,

$$\alpha = \sum_{j=0,1,2} \sigma_j N_j \tag{2.1}$$

where  $\sigma_j$  is the absorption cross section of the transition from state j, and  $N_j$  is its population density.

If we assume the sample length is small compared to the absorption length,  $\alpha^{-1}$ , the pump rate of a transition from state i can be described by,

$$R_{i} \approx \frac{\lambda_{p}}{hc\pi w_{p}^{2}} P\sigma_{i} N_{i} = \rho_{p} \sigma_{i} N_{i}$$
(2.2)

$$\rho_p = \frac{\lambda_p}{hc\pi w_p^2} P \tag{2.3}$$

where  $\lambda_p$  is the exciting wavelength, P is the pump power, h is Planck's constant, c is the speed of light, and  $w_p$  is the pump radius.

To determine the power dependence for ETU, the following rate equations are employed,

$$\frac{dN_1}{dt} = \rho_p \sigma_0 N_0 - 2W_1 N_1^2 - A_1 N_1 \tag{2.4}$$

$$\frac{dN_2}{dt} = W_1 N_1^2 - A_2 N_2 \tag{2.5}$$

Here,  $W_1$  is the parameter describing the energy transfer step that eliminates two  $N_1$  states, forming a single  $N_2$  state. The terms on the right hand side of Equation 2.4 are excitation from GSA, elimination by ETU, and decay by luminescence, respectively. The terms on the right hand side of Equation 2.5 are excitation by ETU, and elimination by decay, respectively. ESA is neglected in this scenario.

Assuming steady state, we obtain,

$$\frac{dN_2}{dt} = W_1 N_1^2 - A_2 N_2 \tag{2.6}$$

$$\rho_p \sigma_0 N_0 = 2W_1 N_1^2 + A_1 N_1 \tag{2.7}$$

From Equation 2.6, it follows that  $N_2 \propto N_1^2$ . If we assume that luminescence dominates at energy level 1, we can neglect the ETU term in Equation 2.7, and find from Equation 2.3 and 2.7 that  $N_1 \propto P \to N_2 \propto N_1^2 \propto P^2$ . This gives the quadratic power dependency that is experimentally observed in 2-photon upconversion. Conversely, if we assume that upconversion dominates, we can neglect the linear decay term in Equation 2.7 and we find that  $N_1^2 \propto P \to N_2 \propto N_1^2 \propto P$ .

A similar examination reveals the power dependence of the ESA upconversion mechanism. Assuming ESA is the dominant mechanism, the rate equations become,

$$\frac{dN_1}{dt} = \rho_p \sigma_0 N_0 - \rho_p \sigma_1 N_1 - A_1 N_1 \tag{2.8}$$

$$\frac{dN_2}{dt} = \rho_p \sigma_1 N_1 - A_2 N_2 \tag{2.9}$$

The terms in Equation 2.8 represent excitation by GSA, elimination by ESA, and decay by luminescence respectively. The terms in Equation 2.9 represent excitation by ESA, and decay by luminescence.

Assuming steady-state, Equation 2.3 and 2.9 lead to the conclusion that  $N_2 \propto N_1 P$ . If we assume that luminescence dominates at energy level 1, we can neglect the ESA term in Equation 2.8, and find that  $N_1 \propto P \rightarrow N_2 \propto N_1 P \propto P^2$  which again, gives a quadratic power dependency. Conversely, if we assume that ESA dominates, we can neglect the linear decay term in Equation 2.8 and find that  $N_1$  has no dependence on P, meaning that  $N_2 \propto P$ .

From this derivation, it is clear that when upconversion is small compared to luminescence, both ESA and ETU mechanisms give quadratic power dependence. A more rigorous derivation of multi-level systems by Pollnau *et al.* shows a  $P^n$  power dependence for n-photon absorption upconversion [9]. This shows a power conversion efficiency of the upconversion process that is proportional to  $P^n_{in}/P_{in} = P^{(n-1)}$ . The conversion efficiency is dependent on the order of the upconversion process (number of photons required), making it difficult to compare absolute efficiency values of different upconversion processes. As a result, the efficiency values of upconversion processes are often normalized against the incident power and reported with units of  $(cm^2/W)^{(n-1)}$ .

While both ESA and ETU have quadratic power dependence, from Figure 2.3, it is clear that ETU has higher experimentally observed efficiency than ESA. This increase in efficiency is derived briefly below, following Auzel [8]. The transitions and corresponding probabilities ( $W_{ij}$ ) used for the following derivation are shown in Figure 2.5.

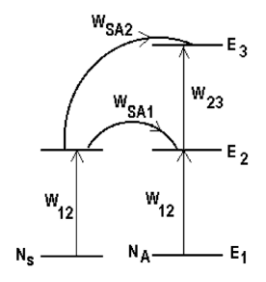


Figure 2.5: Simplified energy level diagram showing sensitizer (left) and activator (right) [8]

Using Figure 2.5 as a reference, the probability of upconversion via ESA is simply the product of the two individual step transitions,

$$W_{13} = W_{12} \cdot W_{23} \tag{2.10}$$

To find the equivalent rate under ETU, the energy transfer probabilities must also be considered,

$$W_{13} \equiv N_S^* W_{SA} N_S^* W_{SA} \tag{2.11}$$

Here,  $W_{SA}$  is the energy transfer probability and  $N_s^*$  is the concentration of excited sensitizers given by,

$$N_{S}^{*} = N_{S}W_{12} \tag{2.12}$$

If we assume that all  $W_{ij}$  probabilities are roughly equal and that  $W_{SA}$  processes are roughly equal, which is typical for rare-earth ions, we obtain the following relations,

$$W_{13} \approx W_{12}^2$$
 in single ion ESA (2.13)

$$W_{13} \approx N_S^{*2} W_{Sd}^2 = N_S^2 W_{12}^2 W_{Sd}^2$$
 in two-ion ETU (2.14)

From Equations 2.13 and 2.14, we can conclude that ETU is greater than ESA by a factor of  $N_s^2 W_{s_4}^2$ .

Since ETU and ESA upconversion mechanisms both have quadratic power dependence, distinguishing between them can be problematic, and they are sometimes confused for one another. They can be distinguished from each other experimentally by examining the time resolved luminescence decay spectra after a short light pulse (order of nanoseconds)[10]. If the mechanism is primarily ESA, all

upconverted states will be populated during the nanosecond pulse and there will be an immediate exponential decay with the lifetime of the upper excited state. If the mechanism is primarily ETU, there is an initial rise time that corresponds to energy migration and energy transfer steps followed by a decay of the upper excited state. This is shown schematically in Figure 2.6.

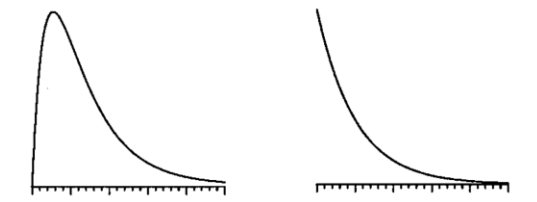


Figure 2.6: Representation of the time resolved luminescence decay of ETU-based upconversion (left) and ESA-based upconversion (right) [10]

#### 2.2.1.2 Other Lanthanide Upconversion Mechanisms

Upconversion mechanisms exist in lanthanide ions other than ETU and ESA as shown in Figure 2.3. Cooperative sensitization and cooperative luminescence are similar in that two excited ions cooperate to emit a single upconverted photon. In cooperative sensitization, a third ion is activated with a real energy state equivalent to double the energy of the sensitizer's excited state. In cooperative luminescence, a virtual state is populated, which emits the upconverted photon. Second harmonic generation (S.H.G.) occurs in nonlinear optical media while 2-photon absorption occurs when the optical intensity is high enough for two photons to be absorbed in a single quantum event (106-109 W/cm²) [11].

Each of these upconversion mechanisms have low experimentally observed upconversion efficiencies (see bottom of Figure 2.3) and/or require excitation intensities that far exceed the integrated intensity of the solar spectrum making them impractical for application to solar cells. Solar concentration could, in principle, help to increase the effectiveness of these mechanisms, however solar concentration presents a number of different challenges itself, and thus the vast majority of research is focussed on ETU and ESA based upconversion in lanthanide ions.

#### 2.2.1.3 Effect of the Host Material

Lanthanide ions are easily doped into optical host materials since most lanthanide ions are trivalent (i.e. Ln³+). This allows them to be exchanged with other trivalent atoms in a crystal lattice. The discrete energy levels that exist in lanthanide ions arise from their unique electronic configuration. Lanthanide ions have a 4fn5s²5p6 electronic configuration where n=0-14, depending on where the element lies in the periodic table. This means there are n electrons that can be in any of the 14 orbitals of the 4f shell, which results in 14/n discrete energy levels. The filled 5s and 5p outer shells serve to shield the inner 4f shell from the surrounding environment, making the ionic energy levels largely independent of the host matrix.

Although the energy levels are shielded in lanthanide ions, the host matrix still affects the optical upconversion process in two primary ways:

- 1. Stark splitting: the surrounding host material creates an electric field that serves to split the energy levels of the absorbing lanthanide ion. This affects the absorption range of the material. The amount of splitting decreases with increasing ionic radius (of host material atoms) leading to a narrower absorption range. For example, chloride hosts have a narrower absorption range compared with fluoride hosts, as can be seen in Figure 2.7 [12].
- 2. Phonon energy: phonons in the host material enable non-radiative relaxations of excited states, and the maximum phonon energy of the host dictates how quickly this will occur. Multiphonon processes are the dominant non-radiative relaxation pathway for excited states and are largely responsible for the decreasing the radiative efficiency of the upconversion process [13]. In general, lower phonon energy host materials such as chlorides, bromides, and iodides have less non-radiative relaxation compared to higher phonon energy host materials like fluorides and oxides [14]. Using the Er³+ upconversion system as an example, different optical processes are possible depending on the host material, as can be seen in Figure 2.8. In the chloride, bromide, and iodide hosts, ESA dominates, resulting in emission at

24000 cm<sup>-1</sup> (blue light). In the fluoride and oxide hosts, multiphonon relaxation means that ETU dominates, resulting in emission at 17500 cm<sup>-1</sup> (green light). Generally speaking, if the energy levels in the active emitter ion are separated by more than 5 times the maximum phonon energy of the host, radiative emission will dominate [15].

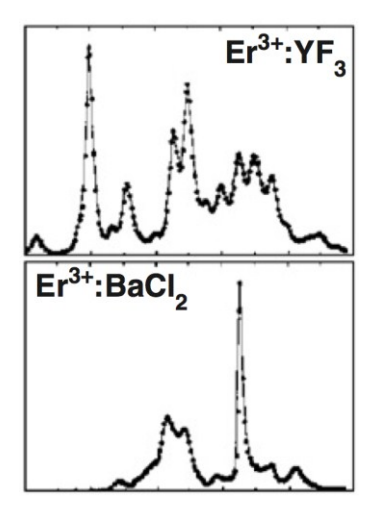


Figure 2.7: Figure illustrating narrower absorption range in chloride host compared with fluoride host [12]

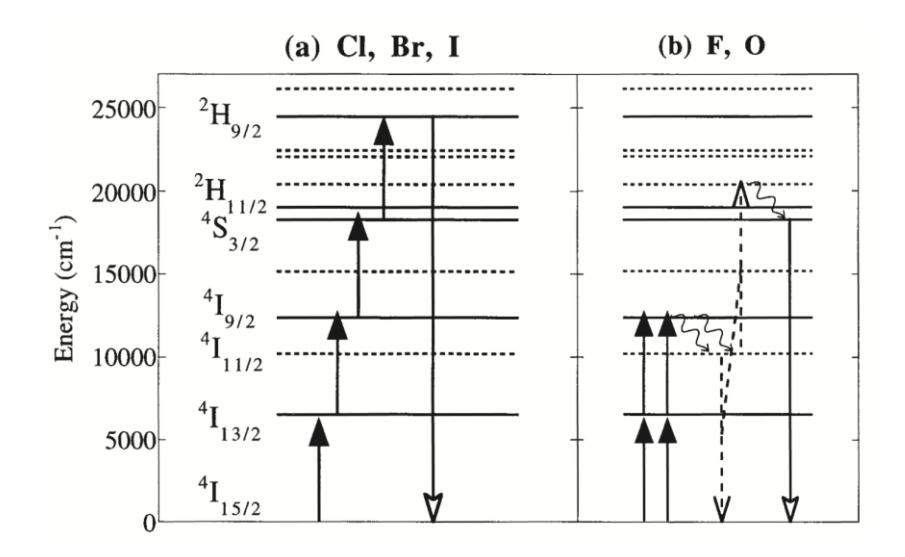


Figure 2.8: Diagram illustrating the optical processes possible in the Er<sup>3+</sup> ion system in different host materials [13].

#### 2.2.2 Organic Molecule Upconversion: Triplet-Triplet Annihilation

There is a great deal of research devoted to the use of organic molecules for upconversion of light. Those used for upconversion are aromatic carbon-based molecules with extended conjugated  $\pi$ -electron orbitals. These conjugated orbitals allow delocalization of the electrons over the entirety of the molecule and give rise to a rich distribution of energy levels. The distribution of energy levels dictates the absorption and emission properties of the molecule, and is dependent on the structure of the molecule. This opens up far more possibilities for engineering of specific energy levels when compared to the limited energy level spacing of lanthanide ions. However, it also introduces a great deal of complexity in optimization of upconversion in organic systems.

Upconversion via organic molecules works in a very similar way to ETU upconversion in lanthanide ion pairs. There is a sensitizer organo-metallic molecule, which has a metallic ion at its center and absorbs light based on metal-to-ligand charge-transfer (MLCT) transitions. The sensitizer molecule is initially excited to its first singlet state, S<sub>1</sub>, after which it decays to its first triplet state, T<sub>1</sub>, via intersystem crossing. This decay occurs before deactivation via fluorescence from the singlet state can occur. Energy transfer then occurs from the sensitizer triplet state to the activator triplet state. Two activator triplet states then promote a single activator singlet state via a process known as triplet-triplet annihilation (TTA) [16]. The singlet state of the activator then fluoresces, producing upconverted light. This process is illustrated in Figure 2.9.

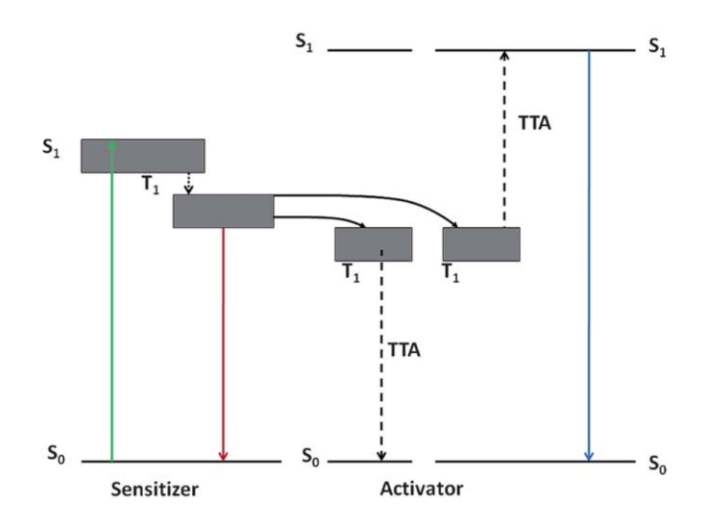


Figure 2.9: Diagram illustrating transitions leading to upconversion in the organic molecular system [17]

In organic upconversion, the triplet state of the activator must be lower than the triplet state of the sensitizer in order to facilitate energy transfer. The singlet state of the activator must also be higher in energy than the singlet state of the sensitizer in order for the emitted photon to have higher energy than the absorbed photons.

#### 2.3 Current Upconversion Materials and their Applications in Solar Cells

This section outlines the different materials that are described in literature for which upconversion has been demonstrated. The applications of upconversion materials to various solar cell technologies will also be discussed.

#### 2.3.1 Single Ion-Doped Materials

Examples of single ions used as dopants for upconversion materials include erbium [18]–[22], ytterbium [23], praseodymium [24], uranium [25], [26], thulium [27], and holmium [28]. Auzel has presented a highly comprehensive review on all the available single-ion-based upconversion materials [8]. Of these ions,  $Er^{3+}$  is the most widely researched for its many energy levels and suitability for infrared applications, particularly with regards to optical communications in the 1.5  $\mu$ m wavelength region. Erbium shows a number of different upconversion bands that are summarized in Table 2.1.

Table 2.1: Er<sup>3+</sup> upconversion emission bands under 1.5μm excitation. Table adapted from [14].

Emission (nm)	Transition	Number of Photons Required
980	${}^{4}I_{11/2} \rightarrow {}^{4}I_{15/2}$	2
810	$^{4}I_{9/2} \rightarrow ^{4}I_{15/2}$	2
660	${}^{4}F_{9/2} \rightarrow {}^{4}I_{15/2}$	3
550	${}^{4}S_{3/2} \rightarrow {}^{4}I_{15/2}$	4
410	${}^{2}\mathrm{H}_{9/2} \rightarrow {}^{4}\mathrm{I}_{15/2}$	5

**Application to solar cells**: Erbium-doped materials have been used in a few instances to help increase solar cell response in the infrared region. Richards *et al.* have applied a 20% Er<sup>3+</sup> doped NaYF<sub>4</sub> upconversion phosphor as a rear reflection layer to bifacial silicon solar cells [29]. Under 2.4W/cm<sup>2</sup> excitation at 1523nm, external quantum efficiency (EQE) of 3.4% (1.4x10<sup>-2</sup> cm<sup>2</sup>/W) was observed. Ahrens *et al.* produced a similar system, using 20%Er<sup>3+</sup>:NaYF<sub>4</sub> on a bifacial silicon solar cell [30]. 2.3W/cm<sup>2</sup> laser light at 1523nm was used and a maximum EQE of 0.008% was observed, much lower than the 3.4% observed by Richards *et al.* [29].

#### 2.3.2 Cooperative Ion-Doped Materials

Upconversion in cooperative ion systems occurs primarily and most efficiently through ETU as already described in Section 2.2.1.1. There are a number of pairs that are often utilized in literature, which are described briefly below.

#### 2.3.2.1 Yb<sup>3+</sup>, Er<sup>3+</sup> Pair

The ytterbium (sensitizer), erbium (activator) ion pairing is the most efficient upconversion pair to date. Yb $^{3+}$ , Er $^{3+}$  doped NaYF $_4$  has the highest upconversion efficiency with up to 50% of absorbed infrared photons being upconverted to visible bands in the high power limit (>600 mW) [15].

In this pairing, the Yb<sup>3+</sup> ion absorbs light in the infrared, near 970nm, and transfers energy to the  $Er^{3+}$  ion. After multiple energy transfer events, upconverted emission occurs in the visible range, primarily as red ( $\sim$ 670 nm) and green ( $\sim$ 540 nm) but also as blue ( $\sim$ 420 nm). The energy band diagram of the Yb<sup>3+</sup>,  $Er^{3+}$  pair is shown in Figure 2.10.

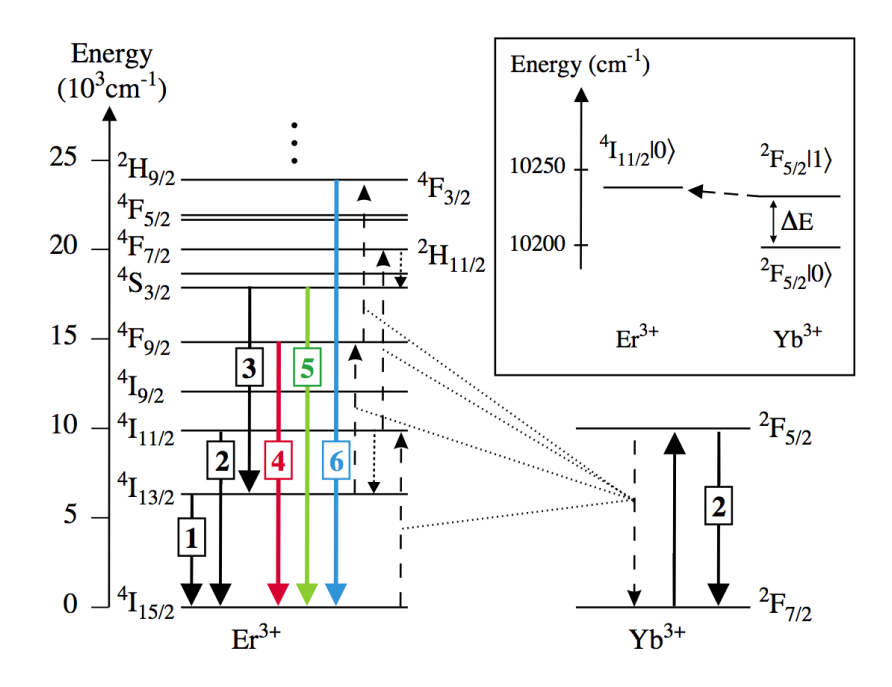


Figure 2.10: Energy level diagram showing the energy transfer steps in the Yb<sup>3+</sup>-Er<sup>3+</sup> upconversion system. Solid and dashed arrows represent radiative and non-radiative energy transitions respectively. Numbered arrows indicate possible emissive transitions [31]

The energy transfer step occurs from the  ${}^2F_{5/2}|1\rangle$  state of the Yb³+ to the  ${}^4I_{11/2}|0\rangle$  state of the Er³+ and is essentially a resonant energy transfer, with a difference of only  $\sim$ 4 cm⁻¹. The upconversion emission in NaYF4:Er³+, Yb³+ is heavily dependent on temperature [31]. This is because upon absorption, the  ${}^2F_{5/2}|0\rangle$  is excited and an energy difference ( $\Delta E$ ) of  $\sim$ 39 cm⁻² must be overcome in order to populate the  ${}^2F_{5/2}|1\rangle$  before energy transfer can occur. The distribution between these two states is dictated by Boltzmann statistics. Using the numbered transitions in Figure 2.10 as a reference, the intensity of emission band 2 is governed by the population density in the  ${}^2F_{5/2}|0\rangle$  state. The intensity of emission bands 1,3-5 is governed by the population density in the  ${}^2F_{5/2}|1\rangle$  state and is given by,

$$I_{i}(T) = I_{i,\infty} \exp \left[ -\frac{p_{i} \Delta E}{k_{B} T} \right] \left[ \sigma_{Yb}(T) \right]^{p_{i}} \quad i \neq 2$$
(2.15)

Here,  $I_{i,\infty}$  is the intensity of the  $i^{th}$  band in the high temperature limit,  $p_i$  is the number of Yb<sup>3+</sup> excitations to excite the  $i^{th}$  band,  $k_B$  is the Boltzmann constant, T is

the temperature,  $\Delta E$  is the energy difference shown in Figure 2.10, and  $\sigma_{Yb}$  is the excitation cross section of the Yb<sup>3+</sup> ion.

The concentration of active ions in the host matrix is also very important. Increasing the concentration of the sensitizer, Yb<sup>3+</sup>, will increase the probability of ETU quadratically, as already shown in Section 2.2.1.1, however the probability tends to reach a maximum at higher concentrations [32]. Increasing the concentration of the activator, Er<sup>3+</sup>, can lead to higher probability of cross-relaxations, increasing the number of non-radiative pathways for higher excited states [33]. In the NaYF<sub>4</sub> lattice, a concentration of 18% Yb<sup>3+</sup> and 2% Er<sup>3+</sup> (atomic percent, replacing Y<sup>3+</sup> in the lattice) has been shown to give the best upconversion properties in the visible range [34].

**Application to solar cells:**  $Er^{3+}$ -Yb<sup>3+</sup> ion pairs are used most often in proof-of-concept studies for demonstrating spectral engineering in solar cells. One of the earliest studies was done by Gilbart *et al.* with a  $Er^{3+}$ , Yb<sup>3+</sup> co-doped vitroceramic material used as a rear reflection layer for a GaAs solar cell [35]. The solar cell was illuminated with 1 W of 891 nm laser light, just below the bandgap of GaAs. The measured solar cell efficiency at this wavelength was 2.5%, demonstrating the possibility of upconversion for capturing sub-bandgap light. Similar studies exist for crystalline silicon solar cells, using the commercial upconversion phosphor, PTIR545/F [36]. The exact composition of PTIR545/F is not publicized, however it is most likely  $Gd_2O_2S$  doped with Yb<sup>3+</sup> and  $Er^{3+}$  [17].

Amorphous silicon has a higher bandgap than crystalline silicon (1.7 eV compared with 1.12 eV, making it better suited for upconversion (see Figure 2.1). De Wild *et al.* have applied an 18% Yb<sup>3+</sup>, 2% Er<sup>3+</sup>: NaYF<sub>4</sub> upconversion phosphor as a rear reflector layer in an a-Si solar cell [37]. Under 3 W/cm<sup>2</sup> 980 nm laser illumination, an EQE response of 0.03% was observed.

The Yb<sup>3+</sup>-Er<sup>3+</sup> upconversion pair has also been applied to DSSCs. Shan *et al.* applied an 18% Yb<sup>3+</sup>, 2% Er<sup>3+</sup>: NaYF<sub>4</sub> nanoplatelet phosphor rear reflector layer to a DSSC [38], achieving approximately 10% increase in photocurrent and overall DSSC

efficiency. This was attributed to dual contributions from upconversion and from light reflection in the upconversion phosphor layer. Liu *et al.* have applied a sintered 3% Yb<sup>3+</sup>, 0.5% Er<sup>3+</sup>: YAG rear reflection layer, observing a photocurrent response of 0.2 mA/cm<sup>2</sup> under 500 mW 980 nm laser illumination [6].

There have also been efforts to implement an internal upconversion layer, specifically for DSSC technology. The potential advantage of an internal layer is increased coupling of the upconverted light to the solar cell. Shan et al. have attempted to implement an internal Yb<sup>3+</sup>, Er<sup>3+</sup>: LaF<sub>3</sub>/TiO<sub>2</sub> nanocomposite layer as a scattering layer in DSSCs [39]. The implementation showed response under 980 nm laser illumination, but limited improvement was observed in overall conversion efficiency under simulated solar light. It was determined that the presence of the upconversion layer increases charge recombination, which offsets the positive impact of the upconversion effect. More recently, better results have been achieved using a similar upconversion system of  $Y_{0.78}Yb_{0.18}Er_{0.02}F_3$  mixed into the  $TiO_2$ photoanode [40]. When the weight ratio of the upconvertor in the photoanode was 7%, a 35% increase in overall conversion efficiency was observed under simulated solar light compared to a DSSC without the upconvertor included in the photoanode. More recently, core-shell approaches have been used to incorporate NaYF4:Yb,Er materials as internal layers in DSSCs. Liang et al. were able to successfully incorporate a NaYF<sub>4</sub>@TiO<sub>2</sub> scattering layer with a 30% relative increase in efficiency [41], while Zhang et al. completely replaced the photoanode layer with a core-shell NaYF<sub>4</sub>@TiO<sub>2</sub> material with a 23% relative increase in efficiency [42].

### 2.3.2.2 Yb<sup>3+</sup>, Tm<sup>3+</sup> Pair

Another well-researched upconversion pair is the ytterbium (sensitizer), thulium (activator) system, which converts infrared light to blue light. The energy level diagram illustrating the upconversion process is shown in Figure 2.11.

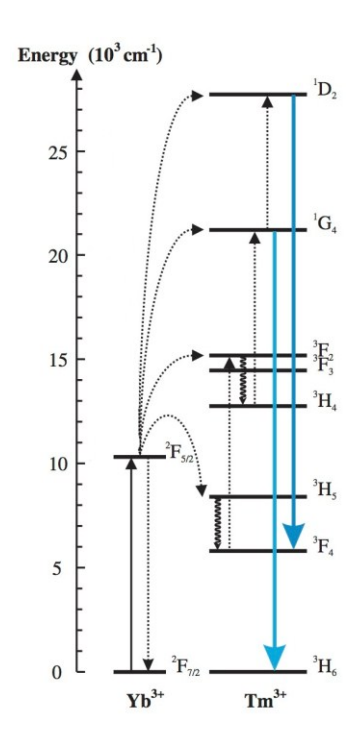


Figure 2.11: Yb-Tm energy level system showing upconversion from infrared to blue. Solid, dotted, and curly arrows indicate radiative transitions, non-radiative transitions, and multiphonon relaxations respectively. Figure adapted from [15].

The optimal concentration of the Yb<sup>3+</sup>-Tm<sup>3+</sup> pair is 25% Yb<sup>3+</sup>, 0.3% Tm<sup>3+</sup> in a NaYF<sub>4</sub> lattice [33], [43]. The efficiency of the upconversion process to blue varies, but is typically much lower than the Yb<sup>3+</sup>-Er<sup>3+</sup> pair, making it less practical for application to solar cells.

#### 2.3.3 Available Host Materials for Lanthanide Doping

Doping of lanthanide ions is done in any crystal lattice that has a trivalent ion that can be replaced by a trivalent lanthanide ion with similar ionic radius. This encompasses a wide variety of materials including oxides, fluorides, chlorides, iodides, and bromides. The impact of the optical host material on the upconversion process has already been discussed in Section 2.2.1.3, and is largely responsible for possible non-radiative processes that quench upconversion fluorescence.

The most efficient and well-documented optical host material is NaYF<sub>4</sub> [31], [33], [34], [44]–[48]. The maximum phonon energy of the NaYF<sub>4</sub> host is about 360cm<sup>-1</sup>

[49], considerably lower than other isostructural fluoride hosts such as LiYF<sub>4</sub> which have phonon energies of up to  $566cm^{-1}$  [50].

Many other host materials have been used for upconversion studies in literature, although none rival NaYF<sub>4</sub> in terms of observed upconversion efficiency. A summary of these host materials is presented in Table 2.2.

Table 2.2: Summary of available host materials in upconversion studies and corresponding lanthanide dopants

Material Classification	Generalized Maximum Phonon Energy [13]	Matrix	Dopant(s)	Reference(s)
	600cm <sup>-1</sup>	Y <sub>3</sub> Al <sub>5</sub> O <sub>12</sub>	Er <sup>3+</sup> /Yb <sup>3+</sup> ; Pr <sup>3+</sup>	[51][52]
		YbPO <sub>4</sub>	Yb <sup>3+</sup>	[53]
Oxide		Vitroceramics	Er <sup>3+</sup> /Yb <sup>3+</sup> ; Tm <sup>3+</sup> /Yb <sup>3+</sup>	[43]
Oxide		$Y_2O_3$	Er <sup>3+</sup> /Yb <sup>3+</sup>	[54]
		$Y_2O_3S$	Er <sup>3+</sup> /Yb <sup>3+</sup>	[54]
		$YVO_4$	Ho <sup>3+</sup> /Yb <sup>3+</sup>	[55]
	355cm <sup>-1</sup>	YF <sub>3</sub>	Er <sup>3+</sup> /Yb <sup>3+</sup> ; Er <sup>3+</sup> ; Tm <sup>3+</sup> /Yb <sup>3+</sup>	[56][19]
		SrF <sub>2</sub>	Er <sup>3+</sup>	[18]
Fluoride		CaF <sub>2</sub>	Er <sup>3+</sup>	[18]
riuoriae		NaYF <sub>4</sub>	Er <sup>3+</sup> /Yb <sup>3+</sup> ; Tm <sup>3+</sup> /Yb <sup>3+</sup>	[33]
		Fluorohafnate glass	Tm <sup>3+</sup> /Yb <sup>3+</sup> ; Ho <sup>3+</sup> /Yb <sup>3+</sup>	[57]
		LiYF <sub>4</sub>	Er <sup>3+</sup> ; Pr <sup>3+</sup>	[18][52]
	260cm <sup>-1</sup>	SrCl <sub>2</sub>	Tm <sup>3+</sup>	[27]
Chloride		BaCl <sub>2</sub>	Er <sup>3+</sup> /Dy <sup>3+</sup>	[58]
Cilioride		Cs <sub>3</sub> Er <sub>2</sub> Cl <sub>9</sub>	Er <sup>3+</sup>	[20]
		Cs <sub>3</sub> Lu <sub>2</sub> Cl	Er³+	[20]
Bromide	172cm <sup>-1</sup>	Cs <sub>3</sub> ErBr <sub>9</sub>	Er <sup>3+</sup>	[20]
		Cs <sub>3</sub> Lu <sub>2</sub> Br <sub>9</sub>	Er <sup>3+</sup>	[20]
		CsCdBr <sub>3</sub>	Ho <sup>3+</sup>	[28]
Iodide	144cm <sup>-1</sup>	Cs <sub>3</sub> Er <sub>2</sub> I <sub>9</sub>	Er <sup>3+</sup>	[20]
Toulde	1440111	$Cs_3Y_2I_9$	Er <sup>3+</sup>	[20]

None of these host materials have been implemented in solar cell studies aside from NaYF<sub>4</sub>, YAG, and vitroceramics, as discussed in the previous sections.

#### 2.3.4 Available Materials for Organic Upconversion

A large number of potential organic sensitizer/activator systems exist for upconversion of light. The number of possibilities is far greater due to the flexibility and degrees of freedom available to the chemist designing the sensitizer or activator

molecules. A comprehensive review on the available sensitizer/activator systems for TTA upconversion has been recently presented by Singh-Rachford *et al.* [59]. Of the systems listed (Table 1 of ref. [59]), the longest wavelength light that can be converted is 780nm to 560nm in the PdTAP/Rubrene sensitizer/activator system [60]. The wavelength ranges of the available systems severely limit the applicability of the organic upconversion systems to solar cells. The absorption and emission spectra of 3 example organic upconversion systems are shown in Figure 2.12.

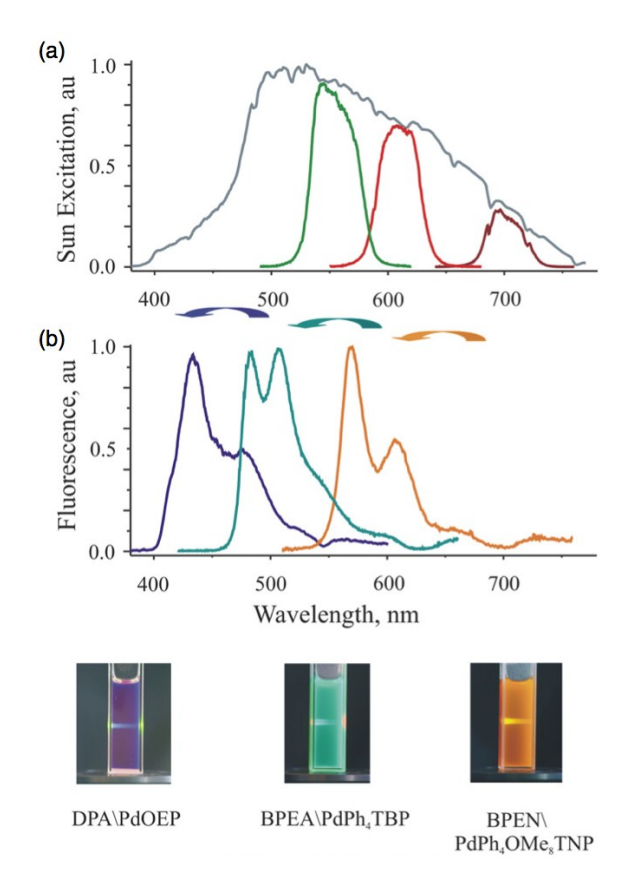


Figure 2.12: (a) Absorption and (b) upconverted fluorescence spectra from 3 different organic upconversion systems. System labels are shown at bottom of the figure and correspond to absorption and fluorescence spectra from right to left, respectively [61].

**Application to solar cells:** Since the upconversion in TTA organic systems is largely visible to visible, there may be competition between the absorption of the upconvertor and the actual solar cell. In general, the upconversion material should absorb in a region where the solar cell does not absorb. The currently available TTA materials are not suitable for silicon solar cells, which absorb infrared light until

 $\sim$ 1100nm, however could be applicable to DSSCs, which absorb light only to about  $\sim$ 770nm. If competition exists between absorption in the solar cell and absorption in the upconvertor, the upconvertor can still be beneficial if the product of the upconversion efficiency and the solar cell quantum efficiency at the upconverted wavelength exceeds the quantum efficiency of the solar cell at the original absorbed wavelength. This is currently unlikely with organic TTA materials, since the upconversion efficiencies are only on the order of a few percent [61]. Great potential exists in organic TTA upconversion materials with a theoretical upconversion efficiency of  $\sim$ 40% [62].

Initial proof of concept studies integrating TTA upconversion materials into solar cells have begun to appear in literature. Recently, Cheng *et al.* have integrated a palladium polyphyrin (sensitizer), rubrene (activator) upconversion system into an a-Si:H solar cell [63]. The systems converted light from long wavelengths of 600-750 nm to shorter wavelengths of 550-600 nm. The peak efficiency enhancement of 1% was seen at 720 nm under an effective irradiation of 48 suns.

There are also organic upconversion materials in literature that rely on two-photon absorption such as Rhodamine B [64], Rhodamine 6G [65], and BPAS [66]. These materials, however, have low efficiencies and require very high excitation energy densities, making them largely irrelevant for application to solar cells.

# 2.4 Review of NaYF<sub>4</sub> Synthesis Procedures

As has already been mentioned in Section 2.3.3, NaYF<sub>4</sub> is the most efficient host material for lanthanide-based upconversion and as such it is the focus of a great deal of research. The optimal doping for NaYF<sub>4</sub> is 18% Yb<sup>3+</sup> and 2% Er<sup>3+</sup> replacing Y<sup>3+</sup> in the NaYF<sub>4</sub> lattice [33], converting infrared light (~980 nm) to visible green (~540 nm) and red (~650 nm). NaYF<sub>4</sub> exists as 2 polymorphs: an  $\alpha$ -cubic phase and a  $\beta$ -hexagonal phase. The  $\beta$ -hexagonal phase is a much better upconversion material [33] and as such the majority of upconversion studies focus on producing this polymorph. A number of synthesis pathways exist for producing upconverting NaYF<sub>4</sub> phosphors with various particle shapes and sizes ranging from nanometers to

micrometers, some of which are shown in Figure 2.13. These synthesis pathways will be briefly reviewed in the following section, with attention given to upconversion properties. As a general note, the abbreviation RE will be used to denote rare-earth elements  $(Y^{3+}, Yb^{3+}, Er^{3+})$  used in synthesis of NaYF<sub>4</sub>:Yb,Er.

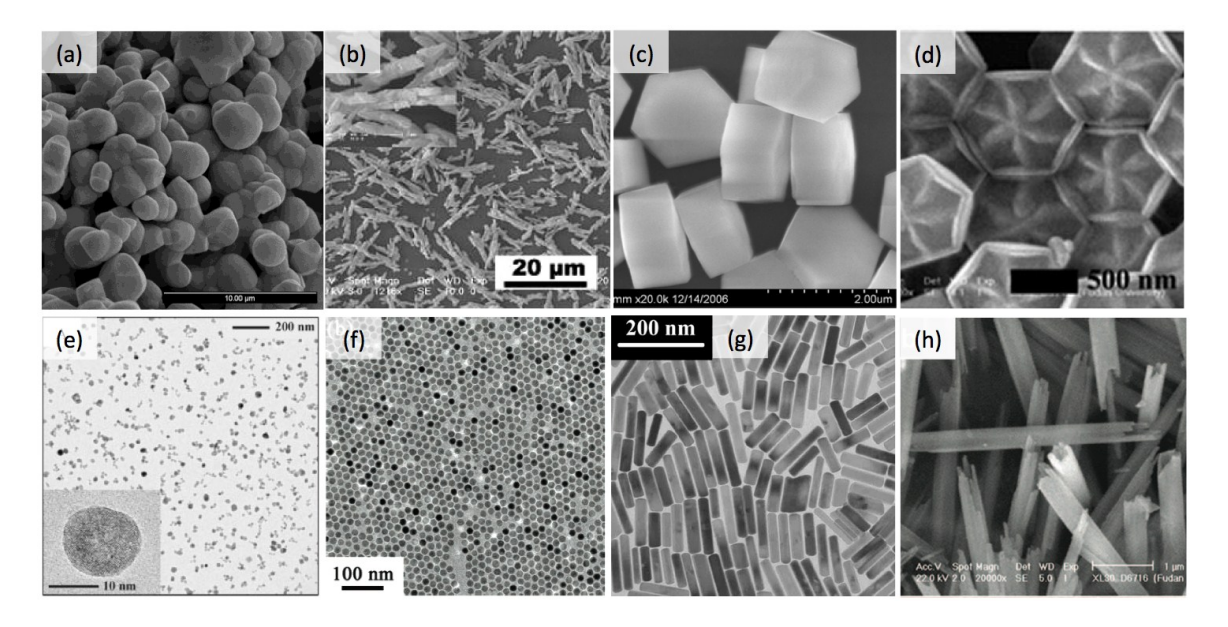


Figure 2.13: Various NaYF<sub>4</sub>:Yb,Er particle types: (a) "bulk" particles by solid state [33], (b) irregular  $\beta$ -crystals by unmodified hydrothermal [67], (c)  $\beta$ -hexagonal prisms by citrate-modified hydrothermal [68], (d)  $\beta$ -nanoflower particles by oleic acid hydrothermal [69], (e)  $\alpha$ -nanoparticles by trifluoroacetate decomposition [47], (f)  $\beta$ -nanospheres by trifluoroacetate decomposition [70], (g)  $\beta$ -nanorods by mixed hydrothermal [71], (h)  $\beta$ -nanotubes by hydrothermal [72].

#### 2.4.1 Solid-State Methods

The first report of NaYF<sub>4</sub>:Yb,Er upconverting materials came in 1972 by Menyuk *et al.* who produced their material by melting stoichiometric amounts of YF<sub>3</sub>, YbF<sub>3</sub>, and ErF<sub>3</sub> with NaF in 20% weight excess [34]. The mixture was heated to 1000 °C, high enough to melt the material according to work done by Thoma *et al.* on the NaF-REF<sub>3</sub> quasi binary systems [73], [74].

Kramer *et al.* were able to improve upon this method by decreasing the required temperature for production of  $\beta$ -NaYF<sub>4</sub>:Yb,Er [33]. In their method, a powdered mixture of REF<sub>3</sub>, NaF, and NaBr compounds were heated under an argon/HF atmosphere to 550 °C. The resulting NaYF<sub>4</sub> produced by a solid-state reaction was ground and heated at 590 °C to produce a highly emitting phosphor. This produced

spherical crystals of 1-3  $\mu$ m that grew into each other, forming a network of particles. This same procedure has been used in a number of other studies [31], [49], [75].

More recently a solid-state approach using a flux coating method has been employed by Suzuki *et al.* for growing NaYF<sub>4</sub>:Yb,Er directly on glass substrates [76]. In this study the NaF and REF<sub>3</sub> precursor materials were used as a solute and NaNO<sub>3</sub> was used as a flux. The dry powders were made into a paste using small amounts of water and coated onto a glass surface. The substrates were heated to 350 or 400 °C for 5 or 10 hours allowing the solute powders to dissolve into the flux and resulting in nucleation of upconverting NaYF<sub>4</sub>:Yb,Er crystals and deposition of a 5  $\mu$ m layer onto the glass. After cooling, the flux was washed away with water.

#### 2.4.2 Solution-Based Methods

In the last 10 years, solution-based method have become the preferred method for production of NaYF<sub>4</sub>:Yb,Er upconverting phosphors as they allow much greater control over particle size and shape, enabling a number of different technological applications.

#### 2.4.2.1 Co-precipitation

Co-precipitation is a simple synthesis in which particles are precipitated from a solution at room temperature. This has been done for NaYF<sub>4</sub>:Yb,Er powders by injecting aqueous solutions of metal chlorides in stoichiometric proportion into a NaF precipitant using EDTA as a chelating agent [77], [78]. The resulting particles are spherical  $\alpha$ -phase particles ranging from 30-150 nm, depending on EDTA concentration. The upconversion luminescence in these particles is initially low; however, increased drastically upon annealing at 400-800 °C. As the temperature was increased, a phase transition from  $\alpha$  to  $\beta$  occurred for temperatures above 400 °C and a transition back to  $\alpha$  occurred for temperatures above 700 °C, and the green-to-red ratio of the emission generally followed the phase ratio of  $\beta/\alpha$ , further demonstrating  $\beta$  as primarily green upconverting and  $\alpha$  as primarily red upconverting [78].

## 2.4.2.2 Hydrothermal/Solvothermal Synthesis

Hydrothermal or more generally, solvothermal, synthesis is done in solution under elevated temperatures and pressures. In the context of NaYF<sub>4</sub>:Yb,Er, water is often used as the solvent [46], [67], [68], [72] however other studies have used mixed water-ethanol [69], [79], [80], and polyols [81], [82] as the solvent. The reaction mechanism of solvothermal synthesis follows the dissolution/crystallization mechanism [83]. As the precursor solution is heated up, the solubility of the precursors increases resulting in dissolution. Once the concentration of precursors in solution reaches a critical point, crystallization of the  $\alpha$ -NaYF<sub>4</sub> phase occurs, driven by the difference in solubility of the NaYF<sub>4</sub> phase and the least soluble precursor. This reaction mechanism is illustrated in Figure 2.14(a).

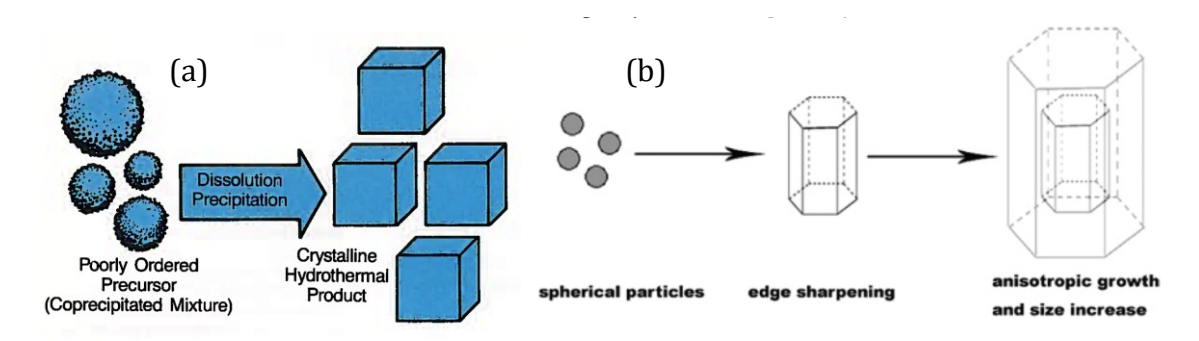


Figure 2.14: Illustration showing (a) the general solvothermal reaction mechanism [83] and (b) the transformation mechanism from  $\alpha$  to  $\beta$  phase [67]

Phase control is possible and is dependant on the hydrothermal synthesis parameters. In hydrothermal synthesis, the  $\alpha$ -phase is the first phase formed as spherical nanoparticles due to isotropic nucleation and growth of the cubic lattice after which growth and transformation to the  $\beta$ -phase occurs, typically forming anisotropic shapes as illustrated in Figure 2.14(b), due to crystal anisotropy of the hexagonal lattice [69]. The phase of the resulting material can be controlled by the reactant concentration [68] as well as synthesis time or temperature.  $\beta$ -phase formation is typical with temperatures of 180 °C or greater and reaction times of 2 hours or longer [67]. Formation of the  $\beta$ -phase can also be promoted through the use of high F-/Ln<sup>3+</sup> ratios [80].

Organic additives play a strong role in dictating the particle size and shape of the particles produced by hydrothermal synthesis. A number of different organic additives have been employed including oleic acid [69], [79], citrate [67], [68], [80], [84], and EDTA [68], [81], [84]. The main role of the additives is two-fold: first, they act as chelating agents for the RE<sup>3+</sup> ions, and second, they adsorb selectively onto nucleated particles and alter their growth in the solution. In the absence of additives, hydrothermal growth of NaYF4:Yb,Er typically produces long irregularshaped crystals on the order of 10 µm. The use of organic additives tends to hinder growth in the <0001> crystal directions, resulting in production of hexagonal prisms, depending on the starting concentration of the additive [67]. More advanced control over particle shape has been demonstrated through the interaction oleic acid, ethanol, and NaOH, producing honey combs, flower-patterned disks, and nanotubes with hexagonal structure [69], [79]. The influence of the additive is largely dependant on the chelating constant which determines the nucleation rate (lower chelating constants give faster nucleation) and the coordination mode, which determines how the additive will adsorb onto the surface of growing particles [84].

A hydrothermal variant known as liquid-solid-solution (LSS) has been used to make monodispersed NaYF<sub>4</sub> and NaYF<sub>4</sub>:Yb,Er nanocrystals [71], [85], [86]. In this reaction type, an aqueous solution of ethanol, oleic acid, RE<sup>3+</sup> ions, NaF, and NaOH is prepared and treated hydrothermally. Three distinct phases form, a liquid ethanol-oleic acid phase, a solid sodium oleate phase, and a solution phase of water, ethanol, and the RE<sup>3+</sup> ions. The RE<sup>3+</sup> and Na<sup>+</sup> ions interact with the F<sup>-</sup> ions at the interface between the phases and result in precipitation of nanorods.

#### 2.4.2.3 Thermal Decomposition of Trifluoroacetates

Another common solution-based method for production of NaYF<sub>4</sub>:Yb,Er nanocrystals is thermal decomposition of trifluoroacetates [44], [87]–[90]. In this type of synthesis, trifluoroacetates synthesized by the dissolution of rare-earth oxides in trifluoroacetic acid [91] and added into octadecene with corresponding amounts of sodium trifluoroacetate, oleic acid, and sometimes oleylamine. A

comprehensive study by Mai *et al.* on a number of NaREF<sub>4</sub> systems showed that size, shape, and phase control was possible by adjusting the temperature, amount of coordinating solvent, and the Na/RE ratio [89]. In general, formation of particles followed the same mechanism as in hydrothermal synthesis, with small  $\alpha$  nanoparticles first forming (250 °C), and transforming to larger  $\beta$  nanoplates with higher temperatures (330 °C). In general, trifluoroacetate decomposition can produce NaYF<sub>4</sub>:Yb,Er particles of very narrow size distribution. Boyer *et al.* have demonstrated  $\alpha$ -particles (~27±3 nm) that were synthesized by slow addition of the lanthanide solution (1mL/min) to the fluoride solution [44], [88].

This method has also been used for synthesizing NaYF<sub>4</sub>:Yb,Er@ NaYF<sub>4</sub> core-shell nanoparticles to help increase upconversion luminescence [92]–[94]. Smaller nanoparticles introduce quenching defects in part due to surface recombination centers resulting from a drastic increase in surface area [48]. Separating the upconverting core from the quenching surface defects can help increase the upconversion luminescence.

#### 2.4.2.4 High Boiling-Point Solvents

Other synthesis techniques involve using a high boiling-point solvent to facilitate solution-based reaction. Various studies have used N-(2-hydroxyethyl)-ethylenediamine (HEEDA) as solvent for preparation of NaYF<sub>4</sub>:Yb,Er [45], [47]. Separate cationic and anionic solutions were prepared using metal chlorides as the cationic source and ammonium fluoride as the anionic source. The solutions were combined and heated at 200 °C, resulting in production of  $\alpha$ -nanoparticles on the order of 10-30 nm. The upconversion fluorescence of these particles is initially very low, but can be increased by modification of the particle surface with 1-dydroxy-ethane-1,1-diphosphonic acid (HEDP) as well as vacuum distillation at 320 °C to remove the HEEDA [45]. It was postulated that the HEDP reacted with the particle surfaces at high temperature, reducing surface recombination states.

Another approach for producing nanoparticles relies on nucleation and growth of the nanoparticles at a liquid-solid interface [95], [96]. In this method, metal oleates were dissolved into 1-octadecene and injected into a separate dispersion of NaF in 1-octadecene. The reaction mechanism follows the same pathway shown in Figure 2.14(b), with small spherical  $\alpha$  particles ( $\sim$ 7 nm) formed initially at 210 °C followed by growth and partial transformation to  $\beta$  at 230°C and full transformation to  $\beta$  hexagonal nanoplates ( $\sim$ 35 nm) at 260 °C. Highest upconversion was observed at 260 °C. Another study by Dou *et al.* showed that by replacing Na+ with varying amounts of Li+ or K+, the emission characteristics could be controlled resulting in multicolour emission [96]. These differences were attributed to phase transitions arising from the different ionic radii of Na+, Li+, and K+. This method has also been used for producing core-shell particles similar to those mentioned in Section 2.4.2.3, except with an ABA (Yb,Tm@Yb,Er@Yb,Tm) doping profile that enabled simultaneous multicolour upconversion due the existence of both Yb,Er and Yb,Tm pairs [97]. This approach was necessary as the luminescence from Tm³+ was quenched when doped in a homogenously doped NaYF4:Yb,Er/Tm particles.

## 2.5 References

- [1] W. Shockley and H. J. Queisser, "Detailed Balance Limit of Efficiency of p-n Junction Solar Cells," *Journal of Applied Physics*, vol. 32, no. 3, p. 510, 1961.
- [2] "Best Research-Cell Efficiencies," *NREL*, 2013. [Online]. Available: http://www.nrel.gov/ncpv/images/efficiency\_chart.jpg. [Accessed: 17-Jun-2013].
- [3] A. Shalav, B. S. Richards, and M. A. Green, "Luminescent layers for enhanced silicon solar cell performance: Up-conversion," *Solar Energy Materials and Solar Cells*, vol. 91, no. 9, pp. 829–842, 2007.
- [4] B. O'Regan and M. Grätzel, "A low-cost, high-efficiency solar cell based on dye-sensitized colloidal TiO<sub>2</sub> films," *Nature*, vol. 353, no. 6346, pp. 737–740, 1991.
- [5] C. Charbonneau, "Aqueous Solution Synthesis of Nanocrystalline TiO<sub>2</sub> Powders: Kinetics, Characterization and Application to Fabrication of Dye-Sensitized Solar Cell Photoanodes," 2011.
- [6] M. Liu, Y. Lu, Z. B. Xie, and G. M. Chow, "Enhancing near-infrared solar cell response using upconverting transparent ceramics," *Solar Energy Materials and Solar Cells*, vol. 95, no. 2, pp. 800–803, 2011.
- [7] F. Auzel, "Compteur quantique par transfert d'energie entre deux ions de terres rares dans un tungstate mixte et dans un verre," *C.R. Acad. Sci.*, no. 262, p. 1016, 1966.
- [8] F. Auzel, "Upconversion and anti-Stokes processes with f and d ions in solids.," *Chemical Reviews*, vol. 104, no. 1, pp. 139–73, 2004.
- [9] M. Pollnau and D. Gamelin, "Power dependence of upconversion luminescence in lanthanide and transition-metal-ion systems," *Physical Review B*, vol. 61, no. 5, 2000.
- [10] T. Riedener and H. U. Güdel, "Upconversion dynamics of Er<sup>3+</sup> doped RbGd<sub>2</sub>Br<sub>7</sub>," *The Journal of Chemical Physics*, vol. 107, no. 7, p. 2169, 1997.
- [11] X. Liu, F. Wang, R. Deng, J. Wang, Q. Wang, Y. Han, H. Zhu, and X. Chen, "Tuning upconversion through energy migration in core–shell nanoparticles," *Nature Materials*, vol. 10, no. 12, pp. 968–973, 2011.
- [12] J. Ohwaki and Y. Wang, "Efficient 1.5um to Visible Upconversion in Er<sup>3+</sup>-Doped Halide Phosphors," *Japanese Journal of Applied Physics*, vol. 33, pp. L334–L337, 1994.
- [13] D. Gamelin and H. U. Güdel, "Upconversion processes in transition metal and rare earth metal systems," *Topics in Current Chemistry*, vol. 214, 2001.
- [14] C. Strümpel, M. McCann, G. Beaucarne, V. Arkhipov, a. Slaoui, V. Švrček, C. del Cañizo, and I. Tobias, "Modifying the solar spectrum to enhance silicon solar cell efficiency—An overview of available materials," *Solar Energy Materials and Solar Cells*, vol. 91, no. 4, pp. 238–249, 2007.

- [15] J. F. Suyver, A. Aebischer, D. Biner, P. Gerner, J. Grimm, S. Heer, K. W. Krämer, C. Reinhard, and H. U. Güdel, "Novel materials doped with trivalent lanthanides and transition metal ions showing near-infrared to visible photon upconversion," *Optical Materials*, vol. 27, no. 6, pp. 1111–1130, 2005.
- [16] H. Sternlicht and G. Nieman, "Triplet—Triplet Annihilation and Delayed Fluorescence in Molecular Aggregates," *The Journal of Chemical Physics*, vol. 38, p. 1326, 1963.
- [17] J. de Wild, A. Meijerink, J. K. Rath, W. G. J. H. M. van Sark, and R. E. I. Schropp, "Upconverter solar cells: materials and applications," *Energy & Environmental Science*, vol. 4, no. 12, pp. 4835–4848, 2011.
- [18] S. A. Pollack and D. B. Chang, "Ion-pair upconversion pumped laser emission in Er<sup>3+</sup> ions in YAG, YLF, SrF<sub>2</sub>, and CaF<sub>2</sub> crystals," *Journal of Applied Physics*, vol. 64, no. 6, p. 2885, 1988.
- [19] J. P. van der Ziel, L. G. Van Uitert, W. H. Grodkiewicz, and R. M. Mikulyak, "1.5-μm infrared excitation of visible luminescent in Y<sub>1-x</sub>Er<sub>x</sub>F<sub>3</sub> and Y<sub>1-x-y</sub>Er<sub>x</sub>Tm<sub>y</sub>F<sub>3</sub> via resonant-energy transfer," *Journal of Applied Physics*, vol. 60, no. 12, p. 4262, 1986.
- [20] S. Lüthi, M. Pollnau, H. Güdel, and M. Hehlen, "Near-infrared to visible upconversion in Er3+-doped Cs<sub>3</sub>Lu<sub>2</sub>Cl<sub>9</sub>, Cs<sub>3</sub>Lu<sub>2</sub>Br<sub>9</sub>, and Cs<sub>3</sub>Y<sub>2</sub>I<sub>9</sub> excited at 1.54 μm," *Physical Review B*, vol. 60, no. 1, pp. 162–178, 1999.
- [21] J. Zhou, W. Zhang, J. Li, B. Jiang, W. Liu, and Y. Pan, "Upconversion luminescence of high content Er-doped YAG transparent ceramics," *Ceramics International*, vol. 36, no. 1, pp. 193–197, 2010.
- [22] M. Pokhrel, G. A. Kumar, P. Samuel, K. I. Ueda, T. Yanagitani, H. Yagi, and D. K. Sardar, "Infrared and upconversion spectroscopic studies of high Er<sup>3+</sup> content transparent YAG ceramic," *Optical Materials Express*, vol. 1, no. 7, p. 1272, 2011.
- [23] M. J. V Bell, W. G. Quirino, S. L. Oliveira, D. F. de Sousa, and L. A. O. Nunes, "Cooperative luminescence in Yb<sup>3+</sup> -doped phosphate glasses," *Journal of Physics: Condensed Matter*, vol. 15, no. 27, pp. 4877–4887, 2003.
- [24] R. Kolesov, R. Reuter, K. Xia, R. Stöhr, A. Zappe, and J. Wrachtrup, "Superresolution upconversion microscopy of praseodymium-doped yttrium aluminum garnet nanoparticles," *Physical Review B*, vol. 84, no. 15, pp. 1–4, 2011.
- [25] S. Hubert, C. L. Song, M. Genet, and F. Auzel, "Up conversion process in U<sup>4+</sup>-doped ThBr<sub>4</sub> and ThCl<sub>4</sub>," *Journal of Solid State Chemistry*, vol. 61, no. 2, pp. 252–259, 1986.
- [26] P. J. Deren, R. Mahiou, and J. C. Krupa, "Strong and weak up-conversion rate in LaCl<sub>3</sub>: U<sup>3+</sup> single crystal," *Journal of Alloys and Compounds*, vol. 380, no. 1–2, pp. 357–361, 2004.
- [27] O. S. Wenger, C. Wickleder, K. W. Krämer, and H. U. Güdel, "Upconversion in a divalent rare earth ion: optical absorption and luminescence spectroscopy of Tm<sup>2+</sup> doped SrCl<sub>2</sub>," *Journal of Luminescence*, vol. 94–95, pp. 101–105, 2001.

- [28] P. Müller, M. Wermuth, and H. U. Güdel, "Mechanisms of near-infrared to visible upconversion in CsCdBr<sub>3</sub>:Ho<sup>3+</sup>," *Chemical Physics Letters*, vol. 290, no. 1–3, pp. 105–111, 1998.
- [29] B. S. Richards and A. Shalav, "Enhancing the Near-Infrared Spectral Response of Silicon Optoelectronic Devices via Up-Conversion," *IEEE Transactions on Electron Devices*, vol. 54, no. 10, pp. 2679–2684, 2007.
- [30] B. Ahrens, P. Löper, J. C. Goldschmidt, S. Glunz, B. Henke, P.-T. Miclea, and S. Schweizer, "Neodymium-doped fluorochlorozirconate glasses as an upconversion model system for high efficiency solar cells," *Physica Status Solidi (a)*, vol. 205, no. 12, pp. 2822–2830, 2008.
- [31] J. F. Suyver, J. Grimm, K. W. Krämer, and H. U. Güdel, "Highly efficient near-infrared to visible up-conversion process in NaYF<sub>4</sub>: Er<sup>3+</sup>, Yb<sup>3+</sup>," *Journal of Luminescence*, vol. 114, no. 1, pp. 53–59, 2005.
- [32] Y. Mita, T. Ide, T. Katase, and H. Yamamoto, "Energy transfer and migration processes in Yb<sup>3+</sup>-ion-sensitized rare-earth-ion-activated luminescent materials," *Journal of Luminescence*, vol. 74, pp. 959–960, 1997.
- [33] K. Kramer, D. Biner, G. Frei, and H. Gudel, "Hexagonal sodium yttrium fluoride based green and blue emitting upconversion phosphors," *Chemistry of Materials*, vol. 16, no. 7, pp. 1244–1251, 2004.
- [34] N. Menyuk, K. Dwight, and J. W. Pierce, "NaYF<sub>4</sub>: Yb,Er—an efficient upconversion phosphor," *Applied Physics Letters*, vol. 21, no. 4, p. 159, 1972.
- [35] P. Gibart, F. Auzel, J.-C. Guillaume, and K. Zahraman, "Below Band-Gap IR Response of Substrate-Free GaAs Solar Cells Using Two-Photon Up-Conversion," *Japanese Journal of Applied Physics*, vol. 35, no. Part 1, No. 8, pp. 4401–4402, 1996.
- [36] A. C. Pan, C. del Cañizo, and A. Luque, "Characterization of up-converter layers on bifacial silicon solar cells," *Materials Science and Engineering: B*, vol. 159–160, pp. 212–215, 2009.
- [37] J. de Wild, J. K. Rath, A. Meijerink, W. G. J. H. M. van Sark, and R. E. I. Schropp, "Enhanced near-infrared response of a-Si:H solar cells with β-NaYF<sub>4</sub>:Yb<sup>3+</sup> (18%), Er<sup>3+</sup> (2%) upconversion phosphors," *Solar Energy Materials and Solar Cells*, vol. 94, no. 12, pp. 2395–2398, 2010.
- [38] G.-B. Shan, H. Assaaoudi, and G. P. Demopoulos, "Enhanced Performance of Dye-Sensitized Solar Cells by Utilization of an External, Bifunctional Layer Consisting of Uniform β-NaYF<sub>4</sub>:Er<sup>3+</sup>/Yb<sup>3+</sup> Nanoplatelets," *ACS Applied Materials & Interfaces*, vol. 3, no. 9, pp. 3239–3243, 2011.
- [39] G.-B. Shan and G. P. Demopoulos, "Near-infrared sunlight harvesting in dyesensitized solar cells via the insertion of an upconverter-TiO<sub>2</sub> nanocomposite layer.," *Advanced Materials*, vol. 22, no. 39, pp. 4373–7, 2010.

- [40] J. Wu, J. Wang, J. Lin, Z. Lan, and Q. Tang, "Enhancement of the Photovoltaic Performance of Dye- Sensitized Solar Cells by Doping Y<sub>0.78</sub>Yb<sub>0.20</sub>Er<sub>0.02</sub>F<sub>3</sub> in the Photoanode," *Advanced Energy*, pp. 78–81, 2011.
- [41] L. Liang, Y. Liu, and X.-Z. Zhao, "Double-shell β-NaYF<sub>4</sub>:Yb<sup>3+</sup>, Er<sup>3+</sup>/SiO<sub>2</sub>/TiO<sub>2</sub> submicroplates as a scattering and upconverting layer for efficient dye-sensitized solar cells.," *Chemical Communications*, vol. 49, no. 38, pp. 3958–60, 2013.
- [42] J. Zhang, H. Shen, W. Guo, S. Wang, C. Zhu, F. Xue, J. Hou, H. Su, and Z. Yuan, "An upconversion NaYF<sub>4</sub>:Yb<sup>3+</sup>,Er<sup>3+</sup>/TiO<sub>2</sub> core–shell nanoparticle photoelectrode for improved efficiencies of dye-sensitized solar cells," *Journal of Power Sources*, vol. 226, pp. 47–53, 2013.
- [43] F. Auzel and D. Pecile, "Rare Earth Doped Vitroceramics: New, Efficient, Blue and Green Emitting Materials for Infrared Up-Conversion," *Journal of the Electrochemical Society*, vol. 122, no. 1, 1975.
- [44] J. C. Boyer and L. A. Cuccia, "Synthesis of colloidal upconverting NaYF<sub>4</sub>: Er<sup>3+</sup>/Yb<sup>3+</sup> and Tm<sup>3+</sup>/Yb<sup>3+</sup> monodisperse nanocrystals," *Nano Letters*, vol. 7, no. 3, pp. 847–852, 2007.
- [45] H. Schäfer, P. Ptacek, K. Kömpe, and M. Haase, "Lanthanide-doped NaYF<sub>4</sub> nanocrystals in aqueous solution displaying strong up-conversion emission," *Chemistry of Materials*, vol. 19, no. 6, pp. 1396–1400, 2007.
- [46] D. Yuan, G. Shun Yi, and G. M. Chow, "Effects of size and surface on luminescence properties of submicron upconversion NaYF<sub>4</sub>: Yb, Er particles," *Journal of Materials Research*, vol. 24, no. 06, pp. 2042–2050, 2009.
- [47] S. Heer, K. Kompe, H.-U. Gudel, and M. Haase, "Highly Efficient Multicolour Upconversion Emission in Transparent Colloids of Lanthanide-Doped NaYF<sub>4</sub> Nanocrystals," *Advanced Materials*, vol. 16, no. 23–24, pp. 2102–2105, 2004.
- [48] F. Wang, Y. Han, C. S. Lim, Y. Lu, J. Wang, J. Xu, H. Chen, C. Zhang, M. Hong, and X. Liu, "Simultaneous phase and size control of upconversion nanocrystals through lanthanide doping.," *Nature*, vol. 463, no. 7284, pp. 1061–1065, 2010.
- [49] J. F. Suyver, J. Grimm, M. K. van Veen, D. Biner, K. W. Krämer, and H. U. Güdel, "Upconversion spectroscopy and properties of NaYF<sub>4</sub> doped with Er<sup>3+</sup>, Tm<sup>3+</sup> and/or Yb<sup>3+</sup>" *Journal of Luminescence*, vol. 117, no. 1, pp. 1–12, 2006.
- [50] S. a. Miller, "Lattice Vibrations of LiYF<sub>4</sub>," *The Journal of Chemical Physics*, vol. 52, no. 8, p. 4172, 1970.
- [51] L. Min, W. Shiwei, Z. Jian, A. Liqiong, and C. Lidong, "Preparation and Upconversion Luminescence of Y<sub>3</sub>A<sub>5</sub>O<sub>12</sub>: Yb<sup>3+</sup>, Er<sup>3+</sup> Transparent Ceramics," *Journal of Rare Earths*, vol. 24, pp. 732–735, 2006.
- [52] M. Malinowski, M. Joubert, and B. Jacquier, "Infrared to blue up-conversion in Pr<sup>3+</sup> doped YAG and LiYF<sub>4</sub> crystals," *Journal of Luminescence*, vol. 60–61, pp. 179–182, 1994.
- [53] E. Nakazawa and S. Shionoya, "Cooperative Luminescence in YbPO<sub>4</sub>," *Physical Review Letters*, vol. 25, no. 25, pp. 1710–1712, 1970.

- [54] R. H. Page, K. I. Schaffers, P. A. Waide, J. B. Tassano, S. A. Payne, W. F. Krupke, and W. K. Bischel, "Upconversion-pumped luminescence efficiency of rare-earth-doped hosts sensitized with trivalent ytterbium," *Journal of the Optical Society of America B*, vol. 15, no. 3, p. 996, 1998.
- [55] W. Ryba-Romanowski, S. Golab, G. Dominiak-Dzik, P. Solarz, and T. Lukasiewicz, "Conversion of infrared radiation into red emission in YVO<sub>4</sub>:Yb,Ho," *Applied Physics Letters*, vol. 79, no. 19, p. 3026, 2001.
- [56] F. Auzel and D. Pecile, "Comparison and efficiency of materials for summation of photons assisted by energy transfer," *Journal of Luminescence*, vol. 8, no. 1, pp. 32–43, 1973.
- [57] M. A. Chamarro and R. Cases, "Energy up-conversion in (Yb, Ho) and (Yb, Tm) doped fluorohafnate glasses," *Journal of Luminescence*, vol. 42, no. 5, pp. 267–274, 1988.
- [58] J. Ohwaki and Y. Wang, "1.3 μm to visible upconversion in Dy<sup>3+</sup>- and Er<sup>3+</sup>- codoped BaCl<sub>2</sub> phosphor," *Applied Physics Letters*, vol. 65, no. 2, p. 129, 1994.
- [59] T. N. Singh-Rachford and F. N. Castellano, "Photon upconversion based on sensitized triplet-triplet annihilation," *Coordination Chemistry Reviews*, vol. 254, no. 21–22, pp. 2560–2573, 2010.
- [60] V. Yakutkin, S. Aleshchenkov, S. Chernov, T. Miteva, G. Nelles, A. Cheprakov, and S. Baluschev, "Towards the IR limit of the triplet-triplet annihilation-supported up-conversion: tetraanthraporphyrin.," *Chemistry*, vol. 14, no. 32, pp. 9846–50, 2008.
- [61] S. Baluschev, V. Yakutkin, T. Miteva, G. Wegner, T. Roberts, G. Nelles, A. Yasuda, S. Chernov, S. Aleshchenkov, and A. Cheprakov, "A general approach for non-coherently excited annihilation up-conversion: transforming the solar-spectrum," *New Journal of Physics*, vol. 10, no. 1, p. 013007, 2008.
- [62] Y. Y. Cheng, B. Fückel, T. Khoury, R. G. C. R. Clady, M. J. Y. Tayebjee, N. J. Ekins-Daukes, M. J. Crossley, and T. W. Schmidt, "Kinetic Analysis of Photochemical Upconversion by Triplet-Triplet Annihilation: Beyond Any Spin Statistical Limit," *The Journal of Physical Chemistry Letters*, vol. 1, no. 12, pp. 1795–1799, 2010.
- [63] Y. Y. Cheng, B. Fückel, R. W. MacQueen, T. Khoury, R. G. C. R. Clady, T. F. Schulze, N. J. Ekins-Daukes, M. J. Crossley, B. Stannowski, K. Lips, and T. W. Schmidt, "Improving the light-harvesting of amorphous silicon solar cells with photochemical upconversion," *Energy & Environmental Science*, vol. 5, no. 5, pp. 6953–6959, 2012.
- [64] P. Qiu and A. Penzkofer, "Intense ultrashort pulse generation in a two-photon pumped generator-amplifier system," *Applied Physics B Photophysics and Laser Chemistry*, vol. 48, no. 2, pp. 115–124, 1989.
- [65] A. Kwok and W. Hsieh, "Two-photon-pumped lasing in microdroplets," *Optics*, vol. 17, no. 20, pp. 1435–1437, 1992.

- [66] G. Zhou, X. Wang, D. Wang, Z. Shao, and M. Jiang, "Upconversion fluorescence and optical power limiting effects based on the two- and three-photon absorption process of a new organic dye BPAS.," *Applied Optics*, vol. 41, no. 6, pp. 1120–3, 2002.
- [67] C. Li, Z. Quan, J. Yang, P. Yang, and J. Lin, "Highly uniform and monodisperse beta-NaYF<sub>4</sub>:Ln<sup>3+</sup> (Ln = Eu, Tb, Yb/Er, and Yb/Tm) hexagonal microprism crystals: hydrothermal synthesis and luminescent properties.," *Inorganic Chemistry*, vol. 46, no. 16, pp. 6329–37, 2007.
- [68] Y. Sun, Y. Chen, L. Tian, Y. Yu, X. Kong, J. Zhao, and H. Zhang, "Controlled synthesis and morphology dependent upconversion luminescence of NaYF<sub>4</sub>:Yb, Er nanocrystals," *Nanotechnology*, vol. 18, no. 27, p. 275609, 2007.
- [69] F. Zhang, J. Li, and J. Shan, "Shape, Size, and Phase-Controlled Rare-Earth Fluoride Nanocrystals with Optical Up-Conversion Properties," *Chemistry-A European Journal*, vol. 15, pp. 11010–11019, 2009.
- [70] H. Mai and Y. Zhang, "Size-and phase-controlled synthesis of monodisperse NaYF<sub>4</sub>: Yb, Er nanocrystals from a unique delayed nucleation pathway monitored with upconversion spectroscopy," *The Journal of Physical Chemistry C*, vol. 111, pp. 13730–13739, 2007.
- [71] L. Wang and Y. Li, "Na(Y<sub>1.5</sub> Na<sub>0.5</sub>)F<sub>6</sub> single-crystal nanorods as multicolor luminescent materials.," *Nano Letters*, vol. 6, no. 8, pp. 1645–9, 2006.
- [72] F. Zhang and D. Zhao, "Synthesis of Uniform Rare Earth Fluoride (NaMF<sub>4</sub>) Nanotubes by In Situ Ion Exchange from Their Hydroxide [M(OH)<sub>3</sub>] Parents," *ACS Nano*, vol. 3, no. 1, pp. 159–164, 2008.
- [73] R. E. Thoma, G. M. Hebert, H. Insley, and C. F. Weaver, "Phase Equilibria in the System Sodium Fluoride-Yttrium Fluoride," *Inorganic Chemistry*, vol. 2, no. 5, pp. 1005–1012, 1963.
- [74] R. Thoma, H. Insley, and G. Hebert, "The sodium fluoride-lanthanide trifluoride systems," *Inorganic Chemistry*, vol. 1005, pp. 1222–1229, 1966.
- [75] C. Renero-Lecuna, R. Martín-Rodríguez, R. Valiente, F. Rodrígues, J. González, K. W. Krämer, and H. U. Güdel, "Origin of the High Upconversion Green Luminescence Efficiency in β-NaYF<sub>4</sub>: 2% Er<sup>3+</sup>, 20% Yb<sup>3+</sup>," *Chemistry of Materials*, vol. 23, pp. 3442–3448, 2011.
- [76] S. Suzuki, K. Teshima, T. Wakabayashi, H. Nishikiori, T. Ishizaki, and S. Oishi, "Novel fabrication of NIR-vis upconversion NaYF<sub>4</sub>:Ln (Ln = Yb, Er, Tm) crystal layers by a flux coating method," *Journal of Materials Chemistry*, vol. 21, no. 36, p. 13847, 2011.
- [77] G. Yi, H. Lu, S. Zhao, Y. Ge, W. Yang, D. Chen, and L.-H. Guo, "Synthesis, Characterization, and Biological Application of Size-Controlled Nanocrystalline NaYF<sub>4</sub>:Yb,Er Infrared-to-Visible Up-Conversion Phosphors," *Nano Letters*, vol. 4, no. 11, pp. 2191–2196, 2004.

- [78] J. S. Lee and Y. J. Kim, "The effects of preparation conditions on the structural and up-conversion properties of NaYF<sub>4</sub>:Yb<sup>3+</sup>, Er<sup>3+</sup> nano powders," *Optical Materials*, vol. 33, no. 7, pp. 1111–1115, 2011.
- [79] F. F. Zhang, Y. Wan, T. Yu, Y. Shi, S. Xie, Y. Li, L. Xu, B. Tu, and D. Zhao, "Uniform Nanostructured Arrays of Sodium Rare-Earth Fluorides for Highly Efficient Multicolor Upconversion Luminescence," *Angewandte Chemie*, vol. 119, no. 42, pp. 8122–8125, 2007.
- [80] Y. Wang, R. Cai, and Z. Liu, "Controlled synthesis of NaYF<sub>4</sub>:Yb,Er nanocrystals with upconversion fluorescence via a facile hydrothermal procedure in aqueous solution," *CrystEngComm*, vol. 13, pp. 1772–1774, 2011.
- [81] Y. Wei, F. Lu, X. Zhang, and D. Chen, "Polyol-mediated synthesis and luminescence of lanthanide-doped NaYF<sub>4</sub> nanocrystal upconversion phosphors," *Journal of Alloys and Compounds*, vol. 455, no. 1–2, pp. 376–384, 2008.
- [82] C. Mi, Z. Tian, C. Cao, Z. Wang, C. Mao, and S. Xu, "Novel microwave-assisted solvothermal synthesis of NaYF<sub>4</sub>:Yb,Er upconversion nanoparticles and their application in cancer cell imaging.," *Langmuir: the ACS journal of surfaces and colloids*, vol. 27, no. 23, pp. 14632–7, 2011.
- [83] W. Dawson, "Hydrothermal synthesis of advanced ceramic powders," *Ceramic Bulletin*, vol. 67, no. 10, p. 1673, 1988.
- [84] C. Li, J. Yang, and P. Yang, "Two-Dimensional B-NaLuF<sub>4</sub> Hexagonal Microplates," *Crystal Growth and Design*, vol. 8, no. 3, pp. 923–929, 2008.
- [85] L. Wang and Y. Li, "Controlled Synthesis and Luminescence of Lanthanide Doped NaYF4 Nanocrystals," *Chemistry of Materials*, vol. 19, pp. 727–734, 2007.
- [86] X. Wang, J. Zhuang, Q. Peng, and Y. Li, "A general strategy for nanocrystal synthesis.," *Nature*, vol. 437, no. 7055, pp. 121–4, 2005.
- [87] D. Yuan, M. C. Tan, R. E. Riman, and G.-M. Chow, "A Comprehensive Study on the Size Effects of the Optical Properties of NaYF<sub>4</sub>:Yb,Er Nanocrystals," *The Journal of Physical Chemistry C*, vol. 117, no. 25, pp. 13297–13304, 2013.
- [88] J. Boyer and F. Vetrone, "Synthesis of colloidal upconverting NaYF<sub>4</sub> nanocrystals doped with Er<sup>3+</sup>, Yb<sup>3+</sup> and Tm<sup>3+</sup>, Yb<sup>3+</sup> via thermal decomposition of lanthanide trifluoroacetate precursors," *Journal of the American Chemical Society*, pp. 7444–7445, 2006.
- [89] H. Mai, Y. Zhang, and R. Si, "High-quality sodium rare-earth fluoride nanocrystals: controlled synthesis and optical properties," *Journal of the American Chemical Society*, vol. 128, no. 19, pp. 6426–6436, 2006.
- [90] K. A. Abel, J.-C. Boyer, and F. C. J. M. van Veggel, "Hard proof of the NaYF<sub>4</sub>/NaGdF<sub>4</sub> nanocrystal core/shell structure.," *Journal of the American Chemical Society*, vol. 131, no. 41, pp. 14644–5, 2009.
- [91] J. Roberts, "Lanthanum and neodymium salts of trifluoroacetic acid," *Journal of the American Chemical Society*, vol. 83, no. 5, pp. 1087–1088, 1961.

- [92] G. Yi and G. Chow, "Water-Soluble NaYF<sub>4</sub>:Yb,Er(Tm)/NaYF<sub>4</sub>/Polymer Core/Shell/Shell Nanoparticles with Significant Enhancement of Upconversion Fluorescence," *Chemistry of Materials*, vol. 19, no. 3, pp. 341–343, 2007.
- [93] H. Mai and Y. Zhang, "Highly efficient multicolor up-conversion emissions and their mechanisms of monodisperse NaYF<sub>4</sub>: Yb, Er core and core/shell-structured nanocrystals," *The Journal of Physical Chemistry C*, vol. 111, no. 37, pp. 13721–13729, 2007.
- [94] Y. Wang, L. Tu, J. Zhao, and Y. Sun, "Upconversion luminescence of β-NaYF<sub>4</sub>: Yb<sup>3+</sup>, Er<sup>3+</sup>@ β-NaYF<sub>4</sub> core/shell nanoparticles: Excitation power density and surface dependence," *The Journal of Physical Chemistry C*, vol. 113, no. 17, pp. 7164–7169, 2009.
- [95] Y. Wei, F. Lu, X. Zhang, and D. Chen, "Synthesis of oil-dispersible hexagonal-phase and hexagonal-shaped NaYF<sub>4</sub>: Yb, Er nanoplates," *Chemistry of Materials*, vol. 18, pp. 5733–5737, 2006.
- [96] Q. Dou and Y. Zhang, "Tuning of the structure and emission spectra of upconversion nanocrystals by alkali ion doping.," *Langmuir*, vol. 27, no. 21, pp. 13236–41, 2011.
- [97] H.-S. Qian and Y. Zhang, "Synthesis of hexagonal-phase core-shell NaYF<sub>4</sub> nanocrystals with tunable upconversion fluorescence.," *Langmuir*, vol. 24, no. 21, pp. 12123–5, 2008.

# Chapter 3: Size-Dependent Maximization of Upconversion Efficiency of Citrate-Stabilized $\beta$ -phase NaYF<sub>4</sub>:Yb<sup>3+</sup>,Er<sup>3+</sup> Crystals via Annealing

In this chapter, the first of two manuscript based chapters, an investigation into the effect of annealing on the upconversion luminescence, phase, and morphology of various nano-to micro-sized NaYF<sub>4</sub>:Yb<sup>3+</sup>,Er<sup>3+</sup> crystals is presented. The investigation focuses on maximizing the upconversion luminescence while avoiding particle agglomeration and significant changes in particle morphology. Maximization of the upconversion luminescence is very important to technological application, particularly integration into DSSCs, as is discussed further in Chapter 4. Three different crystal sizes (300 nm, 700 nm, 2.3  $\mu$ m) were produced by a citrate-stabilized hydrothermal method. The synthesis parameters of the hydrothermal process were controlled such that all crystals were initially hexagonal,  $\beta$ -phase material. Annealing provides a simple avenue to drastically improve the upconversion performance; however, at elevated temperatures a  $\beta$ -to- $\alpha$ -phase transition occurs at the cost of upconversion performance and should be avoided. The effect of annealing is discussed as it relates to upconversion luminescence, particle growth/agglomeration, and particle phase.

This chapter is intended for submission to a journal in the near future. The following provides the current citation information:

Nathan Dyck, Frank C. J. M. van Veggel, George P. Demopoulos, "Size-Dependant Maximization of Upconversion Efficiency of Citrate-Stabilized  $\beta$ -phase NaYF<sub>4</sub>:Yb<sup>3+</sup>,Er<sup>3+</sup> Crystals via Annealing." *ACS Applied Materials and Interfaces.* Submitted. **2013** 

#### 3.1 Abstract

Upconversion materials show great potential in converting infrared light to visible for many optoelectronic and photovoltaic devices. One of the most promising upconverting materials is Yb³+,Er³+ doped  $\beta$ -NaYF₄. In this study, annealing is shown to have a significant impact on the phase, morphology, and upconversion luminescence of  $\beta$ -NaYF₄:Er³+,Yb³+ crystals of varying sizes (300 nm, 700 nm, and 2.3  $\mu$ m) prepared by hydrothermal synthesis stabilized with sodium citrate. Upconversion luminescence is maximized via annealing while maintaining crystal shape and dispersion up to a temperature dependent on initial size, with NIR-to-visible quantum yields of 2-5%. Further temperature increases result in growth and agglomeration, increasing luminescence, followed by transformation to the  $\alpha$ -cubic phase resulting in decreases in overall upconversion performance and shifts to red emission. This study establishes the critical link between annealing temperature and maximal upconversion luminescence in  $\beta$ -NaYF₄:Er³+,Yb³+ crystals while maintaining particle morphology, which can be very important for technological application.

#### 3.2 Introduction

Upconversion is a process in which two or more low-energy photons are converted to a single high-energy photon. This process is possible in a number of different materials; however, lanthanide doped optical host materials are the most common and efficient upconverters available today [1]. While a number of host materials exist, NaYF<sub>4</sub> is the most efficient thanks to its low phonon energy, minimizing the non-radiative pathways for upconverted energy states [2]. NaYF<sub>4</sub> converts infrared light to green and red when doped with Yb<sup>3+</sup> and Er<sup>3+</sup> with the optimal doping concentration of 18 at% Yb<sup>3+</sup> and 2 at% Er<sup>3+</sup> replacing Y<sup>3+</sup> in the lattice [3].

Upconversion from infrared to visible wavelengths has garnered a great deal of attention in recent years due to potential applications in biological markers [4]–[6], photonic devices [7]–[9], and solar cells [10]–[12]. Many of these studies employ synthesis methods for producing particles on the order of nanometers to

micrometers with many different particle shapes including nanospheres, nanorods, nanotubes, and microplates [4], [6], [13]-[16]. The overall efficiency of bulk NaYF<sub>4</sub>:Er<sup>3+</sup>,Yb<sup>3+</sup> is modest, and when the crystal size is reduced to the micro or nanoscale, the upconversion efficiency also suffers due to a number of different phenomena. Smaller nanoparticles typically have more quenching sites including lattice defects that occur due to lower temperatures associated with colloidal synthesis [17] and surface recombination centers due to a drastic increase in surface area [18]. The diffusion length of the intermediate excited Yb3+ states has been shown to be on the order of microns so when the particle size is smaller than this, it is more difficult for two intermediate states to combine and form an upconverted state before relaxing [19]. In addition, depending on the synthesis technique, the doping profile of the nanoparticles is not necessarily homogeneous [20] and it has been shown that surface segregation of the Er3+ ions in smaller particles can decrease the upconversion efficiency due to an increase in cross relaxation that occurs at higher Er<sup>3+</sup> concentrations [21]. Solution-based synthesis methods also often employ chelating agents such as sodium citrate, oleic acid, or EDTA [14], [17]. It has been suggested that preparation using these ligands can lead to upconversion-quenching defects in the crystal lattice depending on the type of ligand used [17]. These organic molecules also remain on the surface of the produced crystals, and vibrational states can provide further pathways for nonradiative recombination of the upconverted states [22].

Increasing and maximizing the efficiency of the upconversion process is important for many technological applications. A number of strategies exist for increasing the upconversion in small particles. Studies of core-shell structures have shown to increase the upconversion luminescence [23], [24]. In these materials, the shell separates the upconverting core from the surface thereby decreasing the possibility for non-radiative pathways on the surface and can lead to increases in upconversion up to 7 times in NaYF<sub>4</sub>:Er,Yb materials [24]. This same effect also helps to increase the green to red ratio, with values as high as 30 in a study by Mai *et al.* [23]. Another study by Wang *et al.* used time-resolved spectroscopy to investigate the kinetics of

the upconversion process and showed that core-shell upconversion materials have a longer luminescent lifetime compared to their core-only counterparts, providing further evidence of the surface mechanism of enhancement. The same study also pointed out the impact of localized annealing caused by high excitation power (>150 W/cm²), which can alter the upconversion spectrum. Other studies have shown improvement in upconversion luminescence by addition of noble metal nanoparticles [25], [26]. This allows the upconverted states to couple with the plasmon modes of the metal nanoparticles, promoting luminescence thereby increasing luminescence yields as much as 10 times in one study [25]. Both coreshell strategies as well as noble metal nanoparticles increase the complexity of synthesis and potential material cost.

A much simpler strategy for enhancing upconversion of lanthanide-doped crystals is by controlled annealing. Annealing has been shown to increase the luminescence in upconversion phosphors through crystal refinement [4], however care must be taken to avoid crystal agglomeration and phase transformation to the  $\alpha$ -cubic phase, which is known to have poorer upconversion properties compared with the βhexagonal phase [3]. Using chelating agents as crystal modifiers like sodium citrate during hydrothermal synthesis allows for stabilization and size control of the βhexagonal phase but this comes at the expense of upconversion intensity [17]. Recently we reported that annealing can significantly increase the upconversion luminescence of surfactant-modified upconversion crystals [27]; however, the annealing temperature was not optimized and annealing while maintaining crystal morphology was not studied nor achieved. In this study, the effect of annealing on the phase, morphology and upconversion luminescence in citrate-stablized, βhexagonal NaYF<sub>4</sub>:Er<sup>3+</sup>,Yb<sup>3+</sup> phosphors of different sizes is investigated. An effort is made to maximize upconversion while limiting morphological changes, which can be detrimental to technological application of the phosphor powders. Through optimization of the annealing conditions, it is demonstrated that even sub-micronsized nanocrystals (300 nm) can be produced with infrared-to-visible quantum yields (2.5%) that are comparable with bulk crystals  $(\sim3\%)$ .

# 3.3 Experimental Section

## 3.3.1 Crystal Synthesis

The synthesis procedure used is based on prior work accomplished in our lab [27], [28]. NaYF<sub>4</sub>:18%Yb<sup>3+</sup>,2%Er<sup>3+</sup> was produced by a citrate stabilized hydrothermal method. Typically, an amount of sodium citrate (2.3, 11, or 54 mmol) was dissolved into 40 mL of deionized water. Following this, Y(NO<sub>3</sub>)<sub>3</sub>•6H<sub>2</sub>O (1.6 mmol),  $Yb(NO_3)_3 \cdot 5H_2O$  (0.36 mmol), and  $Er(NO_3)_3 \cdot 5H_2O$  (0.04 mmol) was added to the solution and stirred until dissolved. Finally, an amount of NaF (18 mmol) was added to the solution and stirred for 15 minutes. The solution was transferred to a 125 mL stainless steel pressure vessel (Parr Instruments) with Teflon liner and heated hydrothermally at 200°C for 2 or 24 hours, depending on sample type. The citrate concentration and hydrothermal reaction time were set in order to obtain βhexagonal phase particles of specific size according to previous work in our lab. A summary of these parameters is found in Table 3.1. After hydrothermal treatment, the resulting precipitate was separated by centrifugation and then washed 3 times with deionized water and once with ethanol. The resulting solids were dried at 80°C for 24 hours. Each sample type was split into equal portions and annealed for 2 hours at temperatures between 400 °C and 700 °C after which it was air-quenched giving final powder samples for analysis.

Undoped reference samples were made using an identical procedure, without the addition of  $Yb(NO_3)_3$  or  $Er(NO_3)_3$ . The reference samples were subjected to the same annealing conditions as their doped counterparts.

Table 3.1: Hydrothermal synthesis parameters for different size upconversion crystals studied

Sample	[Ln <sup>3+</sup> ]	[NaF]	[Cit <sup>3-</sup> ]	Time	Temperature	Crystal
	(mmol)	(mmol)	(mmol)	(hours)	(°C)	Size (nm)
UC1	2	18	2.3	24	200	2300
UC2	2	18	11	24	200	700
UC3	2	18	54	2	200	300

#### 3.3.2 Characterization

Powders were characterized before and after annealing by powder X-ray diffraction (XRD), scanning electron microscopy (SEM), transmission electron microscopy (TEM), attenuated total internal reflection fourier transform infrared spectroscopy (ATR-FTIR), thermogravimetric analysis (TGA), upconversion luminescence, and absolute quantum yield measurements.

XRD analysis was done using a Bruker Discover D8 diffractometer with  $\lambda_{\text{Cu,K}\alpha}$ =1.5406 Å radiation operated at 40 kV and 20 mA. A VANTEC 2000 2D x-ray area detector was used with a 20 frame width of 23° and angular scanning resolution of 0.05°. Four frames were collected for each sample at 50 seconds/frame. Analysis was done using the Eva software package provided by Bruker. SEM analysis was done using a Hitachi S-4700 FE-SEM operated at 2 kV. TEM analysis was done using a Philips CM200 TEM operated at 200 kV. ATR-FTIR analysis was done using a Perkin-Elmer Spectrum Two IR spectrometer with ATR accessory. Scans were taken from 4000-400 cm<sup>-1</sup>.

Upconversion spectra were collected from 450 nm to 700 nm with 0.5 nm step size and 2 nm emission slit using a Fluoromax-2 spectrophotometer with a 980 nm IR laser diode (100 mW, Startech) as excitation source. The fluorescence was measured using the solid powder; the laser spot size was kept the same when comparing samples, ensuring that the interaction volume and laser intensity was the same from sample to sample. The measurement spectra of all samples were recorded under the same conditions and were corrected for the response of the spectrometer and detector. The position of the laser relative to the samples was identical during all measurements. Each sample was immobilized and pressed between two glass slides to ensure a flat surface and uniform packing, and fixed using a metallic sample holder. All annealed samples were ground using a mortar and pestle prior to measurement to minimize soft agglomeration. Upconversion luminescence was quantified by integrating the emission peaks from the obtained spectra. For simpler comparison purposes, integrated values were normalized to the highest emitting samples for each particle size type.

Quantum yield measurements were performed using a procedure following Boyer et al. [29], using a 100 mW NIR laser as excitation, an integrating sphere, a visible spectrometer and photomultiplier tube for measuring the upconverted visible signal, and a NIR spectrometer and photomultiplier tube for measuring the absorbed NIR light. A neutral density filter (10000x) was used to ensure that the NIR PMT was not saturated. Spectra were taken as an average of 5 individual scans with a monochromator slit size of 0.5 nm and were corrected for the spectral response of the corresponding spectrometer. The relative sensitivity of the visible and NIR spectrometers/detectors was calibrated using a tungsten lamp. A schematic of the experimental setup is shown in Figure 3.1. The laser light was incident on the solid powder sample immobilized in a modified EPR tube. Baffles were employed to ensure no upconverted or scattered light was incident on the detectors without first interacting with the integrating sphere. In order to accurately determine the absorption of the doped sample, an undoped reference sample was used as a baseline, duplicating the scattering effect of the sample powder and ensuring the difference between reference and sample was only due to absorption.

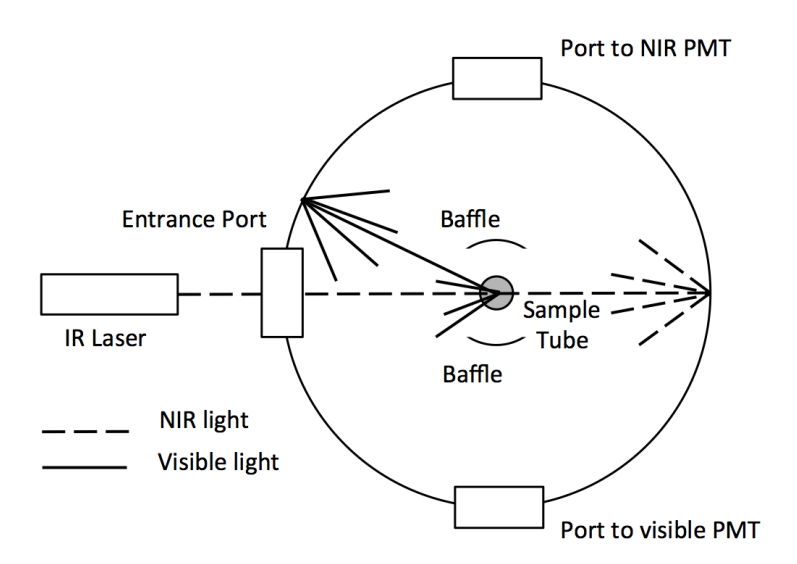


Figure 3.1: Experimental setup schematic for measuring quantum yield of upconversion crystals

#### 3.4 Results and Discussion

Each crystal sample produced was in the form of a white powder. In the case of sample types treated hydrothermally for 24 hours (UC1 and UC2), the hydrothermal

supernatant solution was brown in colour indicating decomposition of residual citrate molecules in solution.

Upconversion luminescence was measured in all samples (a sample emission spectrum can be found in Appendix A, Figure A.1). NaYF<sub>4</sub>:Er³+,Yb³+ emits visible light in two regions: green (510 nm – 560 nm, corresponding to the  ${}^2H_{11/2} \rightarrow {}^4I_{15/2}$  and  ${}^4S_{3/2} \rightarrow {}^4I_{15/2}$  transitions in Er³+) and red (640 nm – 670 nm, corresponding to the  ${}^4F_{9/2} \rightarrow {}^4I_{15/2}$  transition in Er³+). In order to easily compare upconversion between samples, the area under the peaks was integrated, resulting in a single value. For green emission, peaks were integrated from 500 nm to 575 nm, and for red emission, peaks were integrated from 625 to 700 nm. Due to orders of magnitude difference between samples, the integrated values were taken and plotted on a logarithmic scale in Figure 3.2. (Tabulated raw data can be found in Appendix A, Table A.1)

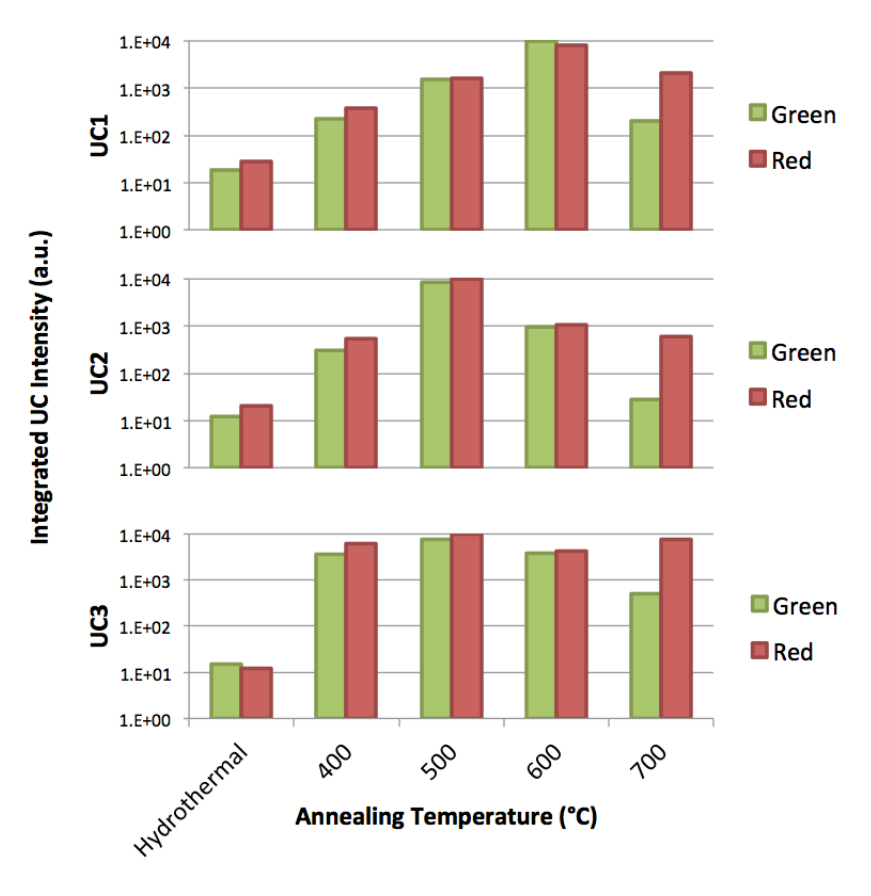


Figure 3.2: Upconversion emission for samples annealed at different temperatures for UC1 (top), UC2 (middle), UC3 (bottom). The log is taken for the integrated peak values, and each gridline represents a decade.

In all the sample types, an increase in upconversion luminescence is observed in both green and red up to a maximum luminescence occurring at 600 °C in UC1 and 500 °C in UC2 and UC3. Increasing the annealing temperature further results in subsequent decrease in upconversion emission. For all sample types annealed at 700 °C, red emission becomes dominant, with red emission more than an order of magnitude greater than green emission.

All samples were found to be pure  $\beta$ -hexagonal phase following hydrothermal treatment as confirmed by XRD. The XRD results presented in Figure 3.3 show a gradual phase change from  $\beta$  to  $\alpha$  with full transformation occurring when the sample is annealed at 700 °C. XRD results are similar for all samples examined in this study and thus only results from the UC2 samples are shown.

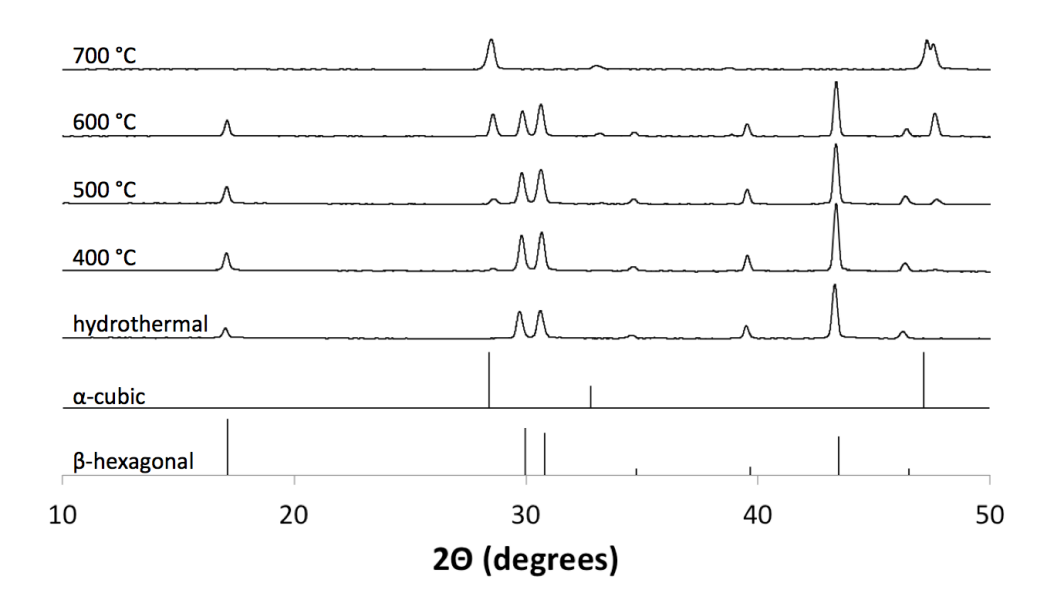


Figure 3.3: XRD results from UC2 showing gradual phase transformation from  $\beta$  to  $\alpha$  via annealing. Reference patterns are shown for cubic (JCPDS 06-0342) and hexagonal (JCPDS 28-1192) phases

Increasing the temperature increases upconversion luminescence to a point, after which upconversion performance diminishes. This is attributed to the  $\beta$  to  $\alpha$  phase transition. The NaF-REF<sub>3</sub> phase diagrams are well known and indicate that this transition temperature should occur at 691 °C, 562 °C, and 702 °C for NaREF<sub>4</sub> (RE=Y, Yb, and Er, respectively) [30]. As such, it is reasonable to assume the phase transformation will occur within this range of temperatures. According to the XRD results presented in Figure 3.3,  $\alpha$ -phase peaks begin to appear at temperatures as

low as 400 °C. With increasing temperature, the strength of the  $\alpha$  peaks increase relative to the  $\beta$  peaks with full transformation to  $\alpha$ -phase at 700 °C. It is well known that the  $\alpha$ -phase is a poorer upconverter compared with its  $\beta$ -phase counterpart [3] so as the material transforms, the overall upconversion performance decreases and red emission cannibalizes green. This explains the decreases seen in annealing temperatures higher than the maximal point where the undesirable effects of the  $\beta$  to  $\alpha$  phase transition overtake the beneficial effects of the annealing.

In order to better understand the relationship between crystal morphology and upconversion fluorescence, the particle morphology as a function of annealing temperature was investigated using SEM. The SEM micrographs are presented in Figure 3.4.

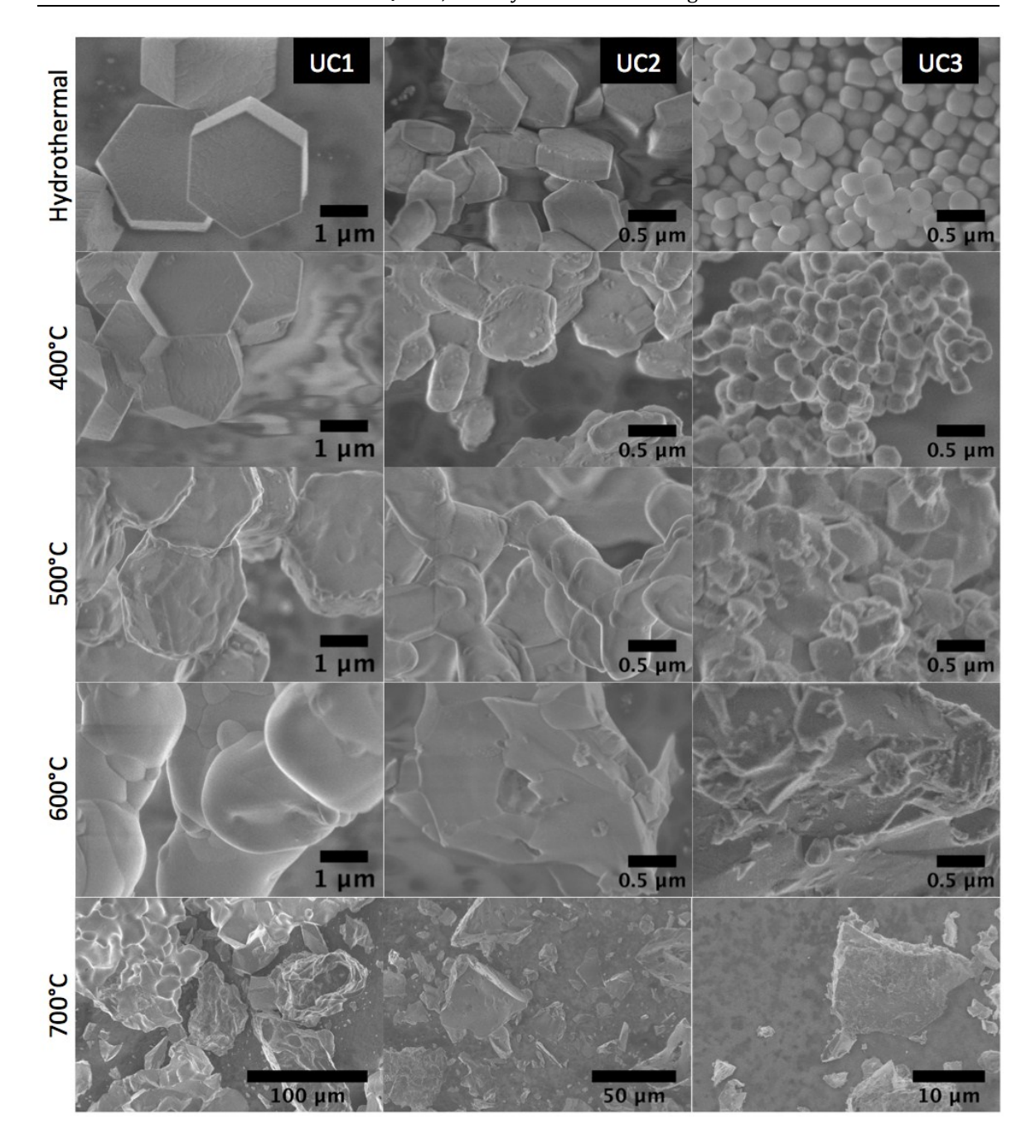


Figure 3.4: SEM micrographs of different size upconversion crystals showing the effect of annealing temperature on morphology (UC1 left, UC2 middle, UC3 right)

It is clear from the SEM micrographs that crystal morphology is changed significantly due to annealing. As the temperature increases, the surface of the particles begins to roughen and particles begin to agglomerate. An additional UC3 sample annealed at 350 °C was prepared to further investigate the agglomeration onset in the sub-micron sized particles. The TEM morphology for UC3-350 is shown

in Figure 3.5. While soft agglomeration is observed, sharp interfaces are still observed between the majority of particles and larger agglomerate networks have yet to form. The upconversion luminescence of this sample is slightly lower than UC3-400 but within the same order of magnitude for both green and red emission (see Appendix A, Table A.1) rendering this material of great interest for technological applications.

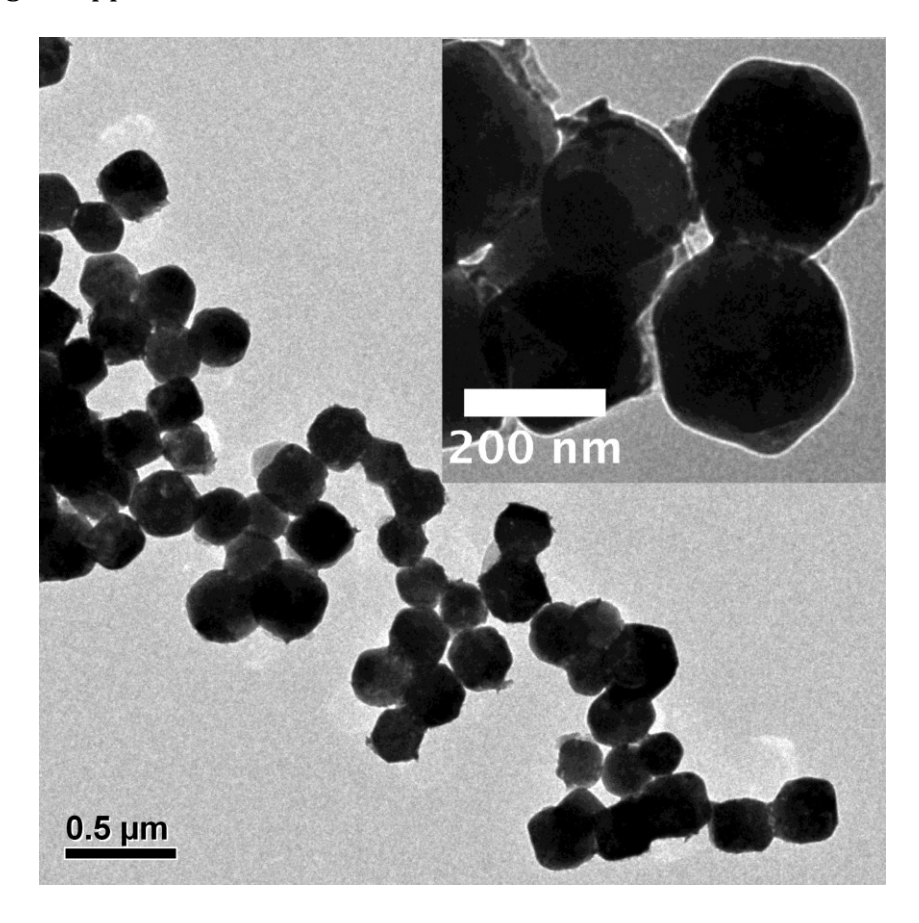


Figure 3.5: TEM micrograph of UC3 crystals annealed at 350 °C for 2 hours

The morphology changes follow the same general mechanism in all size types, first with roughening of the crystal surfaces (onset at 500°C for UC1, 400°C for UC2 and 350°C for UC3), then agglomeration (onset at 600°C for UC1, 500°C for UC2, 400°C for UC3), and finally formation of bulk sized particles (700°C for UC1, 600°C for UC2 and UC3).

The presence of organic molecules can quench the upconversion luminescence as already mentioned. In order to determine the presence of citrate on the surface of

the upconversion particles, ATR-FTIR was performed on the hydrothermal (HT) samples and samples annealed at 400 and 500 °C, shown in Figure 3.6.

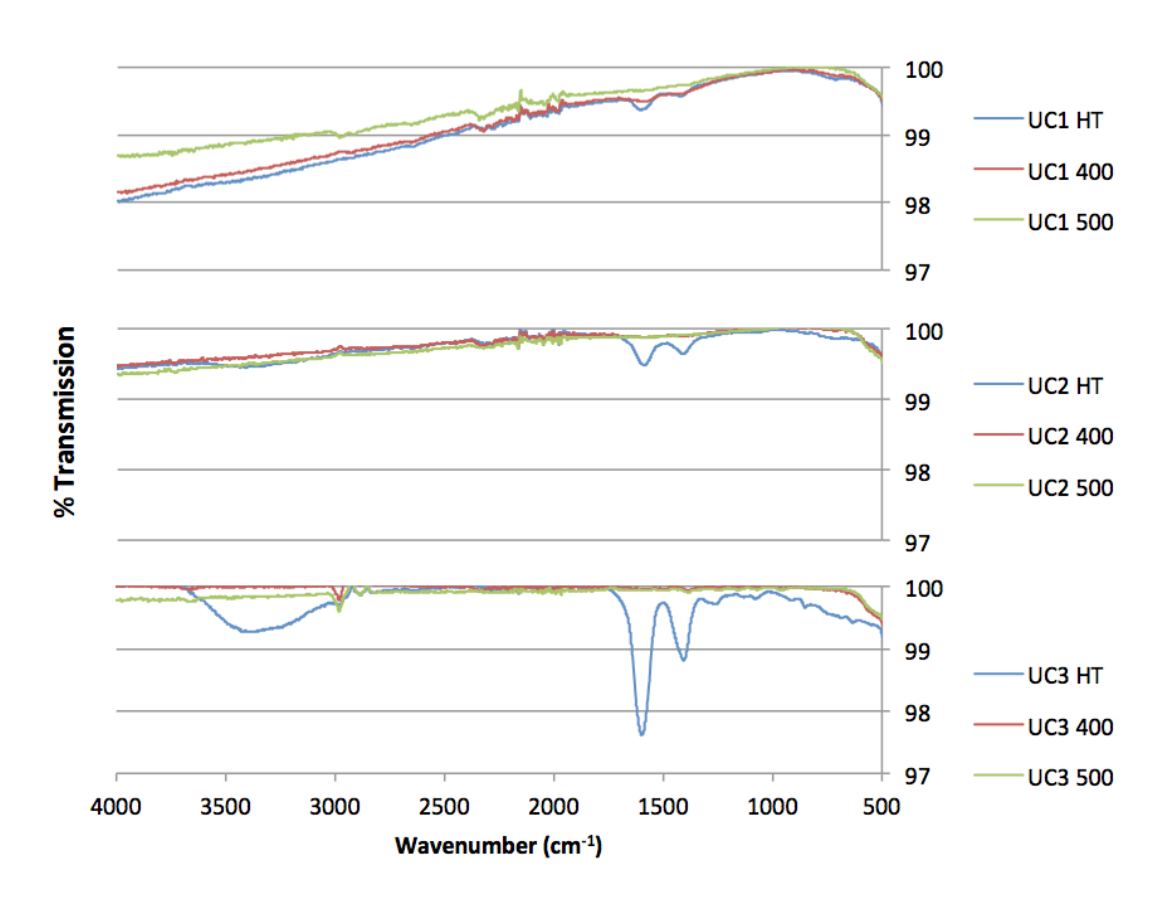


Figure 3.6: ATR-FTIR transmission spectra of hydrothermally produced upconversion samples including samples annealed at 400 and 500  $^{\circ}$ C. All spectra were corrected for the ATR effect using the supplied software.

From the FTIR spectra, peaks are observed at ~1430 cm<sup>-1</sup>, ~1610 cm<sup>-1</sup>, and 3000-3700 cm<sup>-1</sup> that correspond to O-H bending, C=O stretching, and O-H stretching, respectively [27], that confirm the presence of organic citrate moieties. The absorption strength of the peaks corresponds with the amount of citrate initially used in hydrothermal synthesis of the different size crystals (Table 3.1) and the expected increase in surface area available for adsorption in the smaller particles. In the UC1 samples, 500 °C is needed to remove the citrate completely, while in the UC2 and UC3 samples, only 400 °C is needed. The slope present in some of the spectra is due to the scattering effects of the larger particles, which is stronger at shorter wavelengths. Removal of citrate is further evidenced by thermogravimetric analysis (TGA) of sample UC3, presented in Figure A.2 of Appendix A. The plot

reveals a decomposition temperature of 372 °C, supporting the data obtained from FTIR.

Based on these results, it is clear that annealing increases upconversion luminescence. This effect is initially attributed to the removal of the citrate moieties, as seen from the FTIR results. The high-energy vibrational states in the citrate molecules can serve as recombination centers for the upconverted lanthanide states [22], so removing them helps increase the upconversion luminescence. It is also possible that annealing helps to reduce internal defects in the crystal lattice. Higher temperatures increase the diffusion coefficient of atoms in the lattice, which helps to decrease the total number of crystal defects that would otherwise serve as recombination centers for the upconverted states.

Another effect that must be taken into account is agglomeration-driven crystal growth. The general progression of particle morphology is presented schematically in Figure 3.7. As the crystal size decreases in upconversion materials (in particular prior to annealing, refer to Figure 3.2), the upconversion performance also decreases, which is attributed to an increase in surface state recombination centers as well as hindered migration of the intermediate excited states in Yb<sup>3+</sup>. Conversely, when particles grow and agglomerate, a similar increase in upconversion luminescence is expected. According to SEM analysis, crystal agglomeration is observed at 600 °C for UC1, 500 °C for UC2, and 400 °C for UC3. Therefore any increases in upconversion prior to agglomeration can be attributed to citrate removal and crystal refinement however the drastic increase at the maximum point for each sample (600 °C in UC1 and 500 °C in UC2 and UC3) is also due to an effective increase in crystal size accompanied by continued crystal refinement.

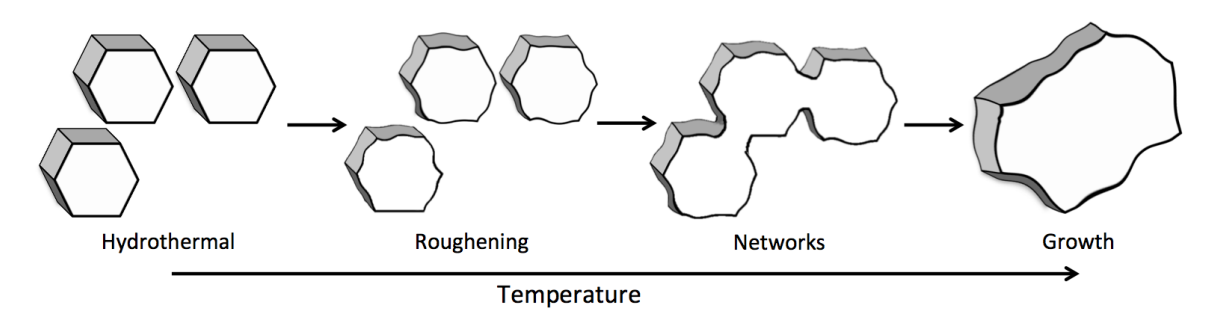


Figure 3.7: Schematic illustrating the changes in particle morphology with increasing temperature

Crystal morphology is very important to certain technological applications and therefore agglomeration should be avoided [4], [28], [31]. The maximum upconversion in our samples without particle agglomeration occurs at 500 °C for UC1, 400 °C for UC2, and 350 °C for UC3. It is highly notable that the initial size of the particles impacts the onset of particle roughening and particle agglomeration. The results show that the smaller the particle size, the sooner the onset of roughening and agglomeration. This can be attributed to greater surface area in smaller particles and therefore greater surface area contact between particles and a greater thermodynamic driving force to reduce the surface free energy. Agglomeration occurs first by a roughening of the particle surface, followed by hard agglomeration, forming interconnected networks of particles, and finally by growth into larger, bulk sized particles.

While the maximum upconversion comes with a loss of the original particle morphology, a stark increase (orders of magnitude) in upconversion is still observed from the hydrothermal samples to samples just before the onset of particle agglomeration, showing that size-dependent controlled annealing can be used to drastically increase upconversion while maintaining the integrity of the original particles. In order to accurately compare the optical properties of the present upconversion crystal samples with those in literature, the quantum yield of the upconversion process was measured in the hydrothermal samples and the annealed samples before the onset of agglomeration.

The quantum yield (QY) is calculated using the following equation [29]:

$$QY = \frac{E_{emission}}{E_{ref} - E_{sample}} \tag{3.1}$$

Here,  $E_{emission}$  is the integrated emission peak (500-575 nm for green or 625-700 nm for red), giving the number of photons emitted,  $E_{ref}$  is the integrated laser peak after absorption and scattering from an undoped reference (NaYF<sub>4</sub>) sample and  $E_{sample}$  is the integrated laser peak of the sample itself, with their difference giving the number of photons absorbed. A sample of the upconverted visible and the NIR laser spectra for an individual measurement is provided in Figure A.3, Appendix A. As upconversion to green or red requires 2 absorbed photons for each emitted photon, the quantum yield will therefore range from 0-50%. For each sample measured, an undoped reference sample was prepared in the exact same manner, including annealing, to most closely reproduce the scattering of the doped sample. The results from these measurements are presented in Table 3.2.

Table 3.2: Quantum yields for hydrothermal samples and highest emitting, non-agglomerated annealed samples

Sample	Annealing Temperature (°C)	Power (W/cm²)	Green QY (%)	Red QY (%)	Total QY (%)	Annealing Enhancement Factor
UC1	N/A	50	0.006 ± 0.001	0.006 ± 0.001	0.01 ± 0.002	
	500	50	1.3 ± 0.3	1.5 ± 0.3	2.7 ± 0.5	270x
UC2	N/A	50	0.01 ± 0.002	0.01 ± 0.002	0.03 ± 0.006	
	400	50	1.8 ± 0.4	3 ± 0.6	4.8 ± 1	160x
UC3	N/A	50	0.02 ± 0.004	0.03 ± 0.006	0.05 ± 0.01	
	350	50	0.9 ± 0.2	1.6 ± 0.3	2.5 ± 0.5	50x

The quantum yield of the upconversion process in the hydrothermal samples is relatively low, on the order of about 0.01-0.05% for all samples studied, however after annealing, the quantum yield can increase by more than 2 orders of magnitude. Notably, the quantum yield of the small-sized UC3 particles ( $\sim$ 300 nm) can be increased to about 2.5%, an achievement that begins to approach that of the larger particles in the current study and bulk particles ( $>4 \mu m$ ,  $\sim$ 3% QY) in other studies

[29], [32]. It should be noted that the power density listed in Table 3.2 was estimated by measuring the distance from the laser to the center of the integrating sphere and using burn paper to measure the laser spot size.

#### 3.5 Conclusions

The size-dependent effect of annealing on phase, morphology, and upconversion luminescence has been investigated systematically by varying the annealing temperature and initial crystal size of NaYF<sub>4</sub>:Er<sup>3+</sup>,Yb<sup>3+</sup> upconversion phosphors. It has been found that a gradual phase transition from the  $\beta$ -hexagonal to the  $\alpha$ -cubic phase occurs beginning with annealing temperatures as low as 400 °C, increasing the relative amount of  $\alpha$ -cubic phase as temperature increases, and resulting in full transformation to the α-phase at 700 °C regardless of initial particle size. In general, as the temperature is increased, particles first begin to roughen, (350 °C in the 300 nm particles, 400 °C in the 700 nm particles, and 500 °C in the 2.3 µm particles), then form interconnected networks (400 °C in the smallest, 500 °C in the mid-sized, 600 °C in the largest particles), and finally transform to bulk-sized particles (600 °C in the smallest and mid-sized particles, 700 °C in the largest). Annealing increases the upconversion luminescence in all samples compared to their hydrothermal counterparts by at least one order of magnitude. Prior to particle agglomeration, this increase is attributed to removal of organic surface molecules and crystal refinement through removal of internal defects that otherwise provide recombination pathways for the excited ion states. The upconversion luminescence reaches a maximum when particles initially form networks, which is a result of the effective increase in particle size in addition to the effects already mentioned. Annealing at higher temperatures will cause a subsequent decrease in upconversion luminescence due to conversion to the  $\alpha$ -phase, which is a poorer upconverter than the β-phase. In summary, the maximum upconversion luminescence while avoiding particle agglomeration is found at 350 °C for the 300 nm particles, 400 °C in the 700 nm particles and at 500 °C for the 2.3 µm particles. Most notably, the quantum yield can be increased by 2 orders of magnitude in the 300 nm particles to about 2.5% while still maintaining particle shape, approaching the quantum yield of much larger particles measured in other studies. This shows that annealing can be used to maximize the upconversion in nano to micro scale upconversion phosphors while maintaining particle shape and that the annealing profile should be tailored depending on the original particle size and shape.

# 3.6 Acknowledgments

This work was funded by NSERC through a strategic project grant to G. P. Demopoulos and sponsored by Targray Technology International, Versatilis, CIS Solar, Hydro-Quebec's IREQ, and Dupont. N. Dyck is also the recipient of an Alexander Graham Bell CGS Scholarship from NSERC. Quantum yield measurements were completed at the University of Victoria under the direction of Prof. van Veggel and Dr. Jothir Mayanantham Pichaandi.

## 3.7 References

- [1] J. F. Suyver, A. Aebischer, D. Biner, P. Gerner, J. Grimm, S. Heer, K. W. Krämer, C. Reinhard, and H. U. Güdel, "Novel materials doped with trivalent lanthanides and transition metal ions showing near-infrared to visible photon upconversion," *Optical Materials*, vol. 27, no. 6, pp. 1111–1130, 2005.
- [2] J. F. Suyver, J. Grimm, M. K. van Veen, D. Biner, K. W. Krämer, and H. U. Güdel, "Upconversion spectroscopy and properties of NaYF<sub>4</sub> doped with Er<sup>3+</sup>, Tm<sup>3+</sup> and/or Yb<sup>3+</sup>," *Journal of Luminescence*, vol. 117, no. 1, pp. 1–12, 2006.
- [3] K. Kramer, D. Biner, G. Frei, and H. Gudel, "Hexagonal sodium yttrium fluoride based green and blue emitting upconversion phosphors," *Chemistry of Materials*, vol. 16, no. 7, pp. 1244–1251, 2004.
- [4] G. Yi, H. Lu, S. Zhao, Y. Ge, W. Yang, D. Chen, and L.-H. Guo, "Synthesis, Characterization, and Biological Application of Size-Controlled Nanocrystalline NaYF<sub>4</sub>:Yb,Er Infrared-to-Visible Up-Conversion Phosphors," *Nano Letters*, vol. 4, no. 11, pp. 2191–2196, 2004.
- [5] Z. Chen, L. Zhang, Y. Sun, J. Hu, and D. Wang, "980-nm Laser-Driven Photovoltaic Cells Based on Rare-Earth Up-Converting Phosphors for Biomedical Applications," *Advanced Functional Materials*, vol. 19, no. 23, pp. 3815–3820, 2009.
- [6] X. Yu, M. Li, M. Xie, L. Chen, Y. Li, and Q. Wang, "Dopant-controlled synthesis of water-soluble hexagonal NaYF<sub>4</sub> nanorods with efficient upconversion fluorescence for multicolor bioimaging," *Nano Research*, vol. 3, no. 1, pp. 51–60, 2010.
- [7] E. Downing, L. Hesselink, J. Ralston, and R. Macfarlane, "A Three-Color, Solid-State, Three-Dimensional Display," *Science*, vol. 273, pp. 1185–1189, 1996.
- [8] F. F. Zhang, Y. Wan, T. Yu, Y. Shi, S. Xie, Y. Li, L. Xu, B. Tu, and D. Zhao, "Uniform Nanostructured Arrays of Sodium Rare-Earth Fluorides for Highly Efficient Multicolor Upconversion Luminescence," *Angewandte Chemie*, vol. 119, no. 42, pp. 8122–8125, 2007.
- [9] R. A. McFarlane, "High-power visible upconversion laser," *Optics Letters*, vol. 16, no. 18, pp. 1397–9, 1991.
- [10] A. Shalav, B. S. Richards, and M. A. Green, "Luminescent layers for enhanced silicon solar cell performance: Up-conversion," *Solar Energy Materials and Solar Cells*, vol. 91, no. 9, pp. 829–842, 2007.
- [11] J. de Wild, A. Meijerink, J. K. Rath, W. G. J. H. M. van Sark, and R. E. I. Schropp, "Upconverter solar cells: materials and applications," *Energy & Environmental Science*, vol. 4, no. 12, pp. 4835–4848, 2011.
- [12] Y. Y. Cheng, B. Fückel, R. W. MacQueen, T. Khoury, R. G. C. R. Clady, T. F. Schulze, N. J. Ekins-Daukes, M. J. Crossley, B. Stannowski, K. Lips, and T. W.

- Schmidt, "Improving the light-harvesting of amorphous silicon solar cells with photochemical upconversion," *Energy & Environmental Science*, vol. 5, no. 5, pp. 6953–6959, 2012.
- [13] C. Li, J. Yang, and P. Yang, "Two-Dimensional B-NaLuF<sub>4</sub> Hexagonal Microplates," *Crystal Growth and Design*, vol. 8, no. 3, pp. 923–929, 2008.
- [14] F. Zhang, J. Li, and J. Shan, "Shape, Size, and Phase-Controlled Rare-Earth Fluoride Nanocrystals with Optical Up-Conversion Properties," *Chemistry-A European Journal*, vol. 15, pp. 11010–11019, 2009.
- [15] J. Zhou, G. Chen, E. Wu, G. Bi, B. Wu, and Y. Teng, "Ultrasensitive polarized upconversion of Tm<sup>3+</sup>-Yb<sup>3+</sup> doped b-NaYF<sub>4</sub> single nanorod," *Nano Letters*, vol. 13, pp. 2241–2246, 2013.
- [16] D. Yuan, M. C. Tan, R. E. Riman, and G.-M. Chow, "A Comprehensive Study on the Size Effects of the Optical Properties of NaYF<sub>4</sub>:Yb,Er Nanocrystals," *The Journal of Physical Chemistry C*, vol. 117, no. 25, pp. 13297–13304, 2013.
- [17] Y. Sun, Y. Chen, L. Tian, Y. Yu, X. Kong, J. Zhao, and H. Zhang, "Controlled synthesis and morphology dependent upconversion luminescence of NaYF<sub>4</sub>:Yb, Er nanocrystals," *Nanotechnology*, vol. 18, no. 27, p. 275609, 2007.
- [18] F. Wang, Y. Han, C. S. Lim, Y. Lu, J. Wang, J. Xu, H. Chen, C. Zhang, M. Hong, and X. Liu, "Simultaneous phase and size control of upconversion nanocrystals through lanthanide doping.," *Nature*, vol. 463, no. 7284, pp. 1061–1065, 2010.
- [19] F. Auzel, "Upconversion and anti-Stokes processes with f and d ions in solids.," *Chemical Reviews*, vol. 104, no. 1, pp. 139–73, 2004.
- [20] C. Dong, J. Pichaandi, T. Regier, and F. C. J. M. van Veggel, "Nonstatistical Dopant Distribution of Ln<sup>3+</sup>-Doped NaGdF<sub>4</sub> Nanoparticles," *The Journal of Physical Chemistry C*, vol. 115, pp. 15950–15958, 2011.
- [21] D. Yuan, G. Shun Yi, and G. M. Chow, "Effects of size and surface on luminescence properties of submicron upconversion NaYF<sub>4</sub>: Yb, Er particles," *Journal of Materials Research*, vol. 24, no. 06, pp. 2042–2050, 2009.
- [22] Y. Wang, L. Tu, J. Zhao, and Y. Sun, "Upconversion luminescence of  $\beta$ -NaYF<sub>4</sub>: Yb<sup>3+</sup>, Er<sup>3+</sup>@  $\beta$ -NaYF<sub>4</sub> core/shell nanoparticles: Excitation power density and surface dependence," *The Journal of Physical Chemistry C*, vol. 113, no. 17, pp. 7164–7169, 2009.
- [23] H. Mai and Y. Zhang, "Highly efficient multicolor up-conversion emissions and their mechanisms of monodisperse NaYF<sub>4</sub>: Yb, Er core and core/shell-structured nanocrystals," *The Journal of Physical Chemistry C*, vol. 111, no. 37, pp. 13721–13729, 2007.
- [24] G. Yi and G. Chow, "Water-Soluble NaYF<sub>4</sub>:Yb,Er(Tm)/NaYF<sub>4</sub>/Polymer Core/Shell/Shell Nanoparticles with Significant Enhancement of Upconversion Fluorescence," *Chemistry of Materials*, vol. 19, no. 3, pp. 341–343, 2007.

- [25] W. Deng, L. Sudheendra, J. Zhao, J. Fu, D. Jin, I. M. Kennedy, and E. M. Goldys, "Upconversion in NaYF<sub>4</sub>:Yb, Er nanoparticles amplified by metal nanostructures.," *Nanotechnology*, vol. 22, no. 32, p. 325604, 2011.
- [26] Z. Li, L. Wang, Z. Wang, X. Liu, and Y. Xiong, "Modification of NaYF<sub>4</sub>: Yb, Er@ SiO<sub>2</sub> nanoparticles with gold nanocrystals for tunable green-to-red upconversion emissions," *The Journal of Physical Chemistry C*, vol. 115, pp. 3291–3296, 2011.
- [27] H. Assaaoudi, G.-B. Shan, N. Dyck, and G. P. Demopoulos, "Annealing-induced ultra-efficient NIR-to-VIS upconversion of nano-/micro-scale  $\alpha$  and  $\beta$  NaYF<sub>4</sub>:Er<sup>3+</sup>,Yb<sup>3+</sup> crystals," *CrystEngComm*, vol. 15, no. 23, pp. 4739–4746, 2013.
- [28] G.-B. Shan, H. Assaaoudi, and G. P. Demopoulos, "Enhanced Performance of Dye-Sensitized Solar Cells by Utilization of an External, Bifunctional Layer Consisting of Uniform β-NaYF<sub>4</sub>:Er<sup>3+</sup>/Yb<sup>3+</sup> Nanoplatelets," *ACS Applied Materials & Interfaces*, vol. 3, no. 9, pp. 3239–3243, 2011.
- [29] J.-C. Boyer and F. C. J. M. van Veggel, "Absolute quantum yield measurements of colloidal NaYF<sub>4</sub>: Er<sup>3+</sup>, Yb<sup>3+</sup> upconverting nanoparticles.," *Nanoscale*, vol. 2, no. 8, pp. 1417–1419, 2010.
- [30] R. Thoma, H. Insley, and G. Hebert, "The sodium fluoride-lanthanide trifluoride systems," *Inorganic Chemistry*, vol. 1005, pp. 1222–1229, 1966.
- [31] C. Han, H. Lee, and K. Lee, "Synthesis of Amorphous Er<sup>3+</sup>-Yb<sup>3+</sup> Co-doped TiO<sub>2</sub> and Its Application as a Scattering Layer for Dye-sensitized Solar Cells," *Bulletin of the Korean Chemical Society*, vol. 30, no. 1, pp. 219–223, 2009.
- [32] D. O. Faulkner, S. Petrov, D. D. Perovic, N. P. Kherani, and G. A. Ozin, "Absolute quantum yields in NaYF<sub>4</sub>:Er,Yb upconverters synthesis temperature and power dependence," *Journal of Materials Chemistry*, vol. 22, no. 46, pp. 24330–24334, 2012.

# Chapter 4: Integration of Upconverting β-NaYF<sub>4</sub>:Yb<sup>3+</sup>,Er<sup>3+</sup>@TiO<sub>2</sub> Nanocomposites as Light Harvesting Layer in Dye-Sensitized Solar Cells

In Chapter 3, the upconversion luminescence of β-NaYF<sub>4</sub>:Yb<sup>3+</sup>,Er<sup>3+</sup> nano and microcrystals was optimized and maximized through the use of annealing. Care was taken to maintain the original crystal morphology for the purposes of internal integration into DSSCs. This chapter outlines the integration of the 300 nm upconversion crystals (UC3 materials of Chapter 3) as an internal, light-harvesting layer in DSSCs. The aim was to have the upconversion layer simultaneously fill the role of infrared-light-harvesting as well as general light scattering, increasing the optical path length and therefore increasing light harvesting over all wavelengths. Due to the electrochemical nature of a DSSC device, integration of these types of materials can interfere with other aspects of device operation, particularly by increasing charge recombination therefore decreasing overall device performance. For this reason, nanocomposite materials were synthesized with a  $\beta$ -NaYF<sub>4</sub>:Yb<sup>3+</sup>,Er<sup>3+</sup>@TiO<sub>2</sub> "core@shell" architecture. A number of materials were prepared and integrated as light harvesting layers. The performance of the resulting solar cells were evaluated both from a light harvesting standpoint and an electrochemical standpoint using IV (current-voltage), incident photon to electron conversion efficiency (IPCE), and electrochemical impedance spectroscopy (EIS) measurements.

This chapter is intended for submission to a journal in the near future. The following provides the current citation information:

Nathan Dyck, George P. Demopoulos, "Integration of Upconverting β-NaYF<sub>4</sub>:Yb<sup>3+</sup>,Er<sup>3+</sup>@TiO<sub>2</sub> Nanocomposites as Scattering Layers in Dye-Sensitized Solar Cells" *Progress in Photovoltaics: Research and Applications*. Submitted. **2013** 

#### 4.1 Abstract

Near-infrared-to-visible upconverting NaYF<sub>4</sub>:Yb<sup>3+</sup>,Er<sup>3+</sup>@TiO<sub>2</sub> nanocomposites were engineered by controlling titanium dioxide coating of citrate-modified β-NaYF<sub>4</sub>:Yb<sup>3+</sup>,Er<sup>3+</sup> nanocrystals of  $\sim$ 300 nm in size and employed as light harvesting layers in dye-sensitized solar cell fabrication. The NIR-to-Vis upconversion response of the as-prepared nanocomposites was enhanced by an increase of 2 orders of magnitude in the upconversion luminescence as a result of annealing effects induced by the thermal processing steps involved in DSSC fabrication. In addition, the TiO<sub>2</sub> coating suppresses the  $\beta$  to  $\alpha$  phase transition in the NaYF<sub>4</sub> thereby maximizing the upconversion response. The as-prepared upconversion crystals as well as 2 types of nanocomposite materials were integrated as internal light-harvesting layers in dyesensitized solar cells (DSSCs). The insertion of the as-prepared or TiO<sub>2</sub>-coated β-NaYF<sub>4</sub>:Yb<sup>3+</sup>,Er<sup>3</sup> crystals with inadequate TiO<sub>2</sub> thickness results in a decrease in photovoltaic performance due to increased charge recombination. By ensuring the β-NaYF<sub>4</sub>:Yb<sup>3+</sup>,Er<sup>3</sup> crystals are fully coated in TiO<sub>2</sub> ("core@shell" configuration), their integration into the DSSC is optimized, resulting in 16% relative increase in powerconversion efficiency over the control devices without the NaYF<sub>4</sub>:Yb<sup>3+</sup>,Er<sup>3+</sup>@TiO<sub>2</sub> nanocomposite internal layer. This increase, as determined by EIS and IPCE under 1 sun illumination, is attributed to recovery of adequate charge recombination resistance and light harvesting enhancement via scattering. Contrary to other reports, the current work shows that despite the successful surface engineering and integration of the optimized upconverting β-NaYF<sub>4</sub>:Yb<sup>3+</sup>,Er<sup>3+</sup> crystals into the DSSC, the effect of upconversion under non-concentrated solar illumination is negligible and other avenues for infrared light harvesting in solar cells need to be pursued.

#### 4.2 Introduction

As the world continues to consume non-renewable sources of fossil fuels, increasing attention is being given to renewable sources of energy such as solar power. The sun is a massive, largely untapped, energy resource. Photovoltaic devices are able to harness the power of the sun by converting the solar energy to electrical energy,

however large-scale deployment is hindered by the relatively high cost of current photovoltaic technologies. The classic efficiency limit of a single junction solar cell is about 30% [1] and research level silicon cells have reached efficiencies as high as 25% [2]. Dye-sensitized solar cells represent a relatively new technology [3] that has seen an explosion in research growth in recent years due largely in part to the promise of low material cost. These types of cells have poorer energy conversion efficiencies compared to established photovoltaic technologies but recently have reached efficiencies of greater than 14% as confirmed by NREL [4], putting DSSCs ahead of competing technologies such as organic PV [5], amorphous silicon [6], and quantum dot solar cells [7].

Many approaches exist for increasing the efficiency of these types of devices, one of which is spectral engineering via upconversion. Dye-sensitized solar cells (DSSCs) absorb light via dye molecules adsorbed onto the surface of nanostructured TiO<sub>2</sub>. Often, this dye is a ruthenium-based complex known as N-719, with a bandgap (HOMO/LUMO gap) of  $\sim$ 1.6 eV. Most of the energy losses at this energy level come from sub-bandgap photons [8], making DSSCs sensitized with these types of dyes ideal candidates for upconversion. Upconversion is a process that converts two or more low energy photons into a single higher energy photon. While many upconversion mechanisms exist, energy transfer upconversion (ETU) via the Yb³+Er³+ lanthanide pair is the most efficient [9]. By far  $\beta$ -NaYF<sub>4</sub> is the most efficient host material for Yb³+-Er³+ upconversion pair, with an optimal doping profile of 18% Yb³+ and 2% Er³+ replacing Y³+ in the host lattice [10]. Infrared-to-visible upconversion has attracted a great deal of attention with potential applications as biological markers [11]–[13], photonic devices [14]–[16], and solar cells [8], [17]–[29].

Recently, application of these materials as internal layers in DSSCs has been the subject of a number of studies [12], [17], [21]–[27]. Shan and Demopoulos investigated the effect of an internal  $LaF_3:Yb^{3+},Er^{3+}-TiO_2$  layer and demonstrated proof-of-concept NIR operation but ultimately saw drops in performance associated with charge recombination [17]. Another study by Wang *et al.* used YOF:Yb<sup>3+</sup>,Er<sup>3+</sup> upconversion materials in the TiO<sub>2</sub> photoanode layer to increase overall conversion

efficiency by a factor of 1.23 [26]. More recently, Zhang *et al.* fully replaced the TiO<sub>2</sub> photoanode material with a NaYF<sub>4</sub>:Yb<sup>3+</sup>,Er<sup>3+</sup>@TiO<sub>2</sub> core-shell composite material, attaining enhancement of the conversion efficiency by a factor of 1.23 [27]. In all these studies, however, insufficient effort has been placed on understanding the best way to integrate these materials, and to the best of the authors knowledge, no studies have adequately determined the relative contributions of upconversion and internal light scattering, therefore doing a poor job of justifying the use of such exotic materials.

In the present study,  $\beta$ -NaYF<sub>4</sub>:Yb<sup>3+</sup>,Er<sup>3+</sup> nanocrystals were prepared using a citrate-stabilized hydrothermal approach to control particle size and morphology. These nanocrystals were coated with TiO<sub>2</sub> ("core@shell" configuration type) to aid with integration into DSSCs as a scattering layer in such way that prevents charge recombination losses. The upconversion properties of the nanocomposite material are investigated, with attention given to the effect of the DSSC thermal processing steps and the true magnitude of upconversion contribution to light harvesting enhancement in the solar cell devices. The cells prepared were tested using a host of photovoltaic and electrochemical testing procedures, including performance under simulated solar illumination as well as NIR laser illumination.

#### 4.3 Experimental Section

#### 4.3.1 Upconverter Synthesis

## 4.3.1.1 NaYF<sub>4</sub>:Yb<sup>3+</sup>,Er<sup>3+</sup> Synthesis

NaYF<sub>4</sub>:18%Yb<sup>3+</sup>,2%Er<sup>3+</sup> was produced by a citrate-modified, hydrothermal method, with a target particle size of 300 nm based on previous work in our lab [30]. Sodium citrate (54 mmol) was first dissolved into 40 mL of deionized water. Following this, Y(NO<sub>3</sub>)<sub>3</sub>•6H<sub>2</sub>O (1.6 mmol), Yb(NO<sub>3</sub>)<sub>3</sub>•5H<sub>2</sub>O (0.36 mmol), and Er(NO<sub>3</sub>)<sub>3</sub>•5H<sub>2</sub>O (0.04 mmol) was added to the solution and stirred until they dissolved. Finally, an amount of NaF (18 mmol) was added to the solution and stirred for 15 minutes. The solution was transferred to a 125 mL stainless steel pressure vessel (Parr Instruments) with

Teflon liner and heated hydrothermally at 200°C for 2 hours, producing  $\beta$ -hexagonal phase particles, about 300 nm in size (refer to characteristic TEM image in Chapter 3, Figure 3.5). After hydrothermal treatment, the resulting precipitate was separated by centrifugation and then washed 3 times with deionized water and once with ethanol. The resulting solids were dried at 80 °C for 24 hours.

#### 4.3.1.2 UC@TiO₂ Nanocomposite Synthesis

For production of the nanocomposite upconverter material a modified process was adopted from Zhang *et al.* [31]. Amorphous titanium dioxide was deposited on the surface of suspended particles in solution based on hydrolysis of titanium ethoxide in ethanol followed by condensation of titanium dioxide. Typically 0.03 g of the NaYF<sub>4</sub>:Yb<sup>3+</sup>,Er<sup>3+</sup> nanocrystals produced were taken and dispersed in 30 mL of anhydrous ethanol using an ultrasonic horn. Following this, 3 mmol of titanium ethoxide (TEOT) was added to the suspension under vigorous stirring. A separate solution was prepared with 30 mL of anhydrous ethanol and an amount of deionized water (DIW, 9 mmol or 18 mmol), which was then added drop wise to the first solution to give an overall DIW:TEOT molar ratio of 3:1 or 6:1 depending on sample. The resulting solution was stirred with a magnetic stir bar, at room temperature, for 2 hours, after which the solids were separated by centrifugation (6000 RPM, 5 min) and washed twice with anhydrous ethanol. The resulting solids were dried at 80 °C for 24 hours.

#### 4.3.2 Dye-Sensitized Solar Cell Fabrication

DSSC photoanodes were prepared using screen-printing. Transparent FTO glass was washed ultrasonically in an aqueous detergent solution (Micro 90) for 15 minutes and rinsed with water and ethanol. Two layers of transparent  $TiO_2$  (18NR-T, Dyesol) were screen printed (AT-25PA, ATMA), drying the layers for 15 minutes at 80 °C between print runs (typically 6  $\mu$ m/run), giving a total transparent layer thickness of 12  $\mu$ m. Depending on the cell type, an additional scattering layer of 4  $\mu$ m was screen printed, using either an industrial benchmark paste (WER2-O, Dyesol) or using pastes prepared with the as-is NaYF<sub>4</sub>:Yb<sup>3+</sup>,Er<sup>3+</sup> crystals or the

NaYF<sub>4</sub>:Yb<sup>3+</sup>,Er<sup>3+</sup>@TiO<sub>2</sub> nanocomposite particles. The procedure used for preparing pastes is published elsewhere [32], [33]. The photoanode was annealed at 450 °C for 30 minutes according to a heating profile (Figure B.1, Appendix B). The photoanode was then submerged in a 40 mM TiCl<sub>4</sub> aqueous solution at 80 °C for 30 minutes, and annealed a second time at 450 °C for 30 minutes. In the case of cells prepared using the NaYF<sub>4</sub>:Yb<sup>3+</sup>,Er<sup>3+</sup> and the NaYF<sub>4</sub>:Yb<sup>3+</sup>,Er<sup>3+</sup>@TiO<sub>2</sub> (DIW:TEOT, 3:1) scattering pastes, the TiCl<sub>4</sub> treatment removes the scattering layer. As such, in these cells the scattering layer was printed after the TiCl<sub>4</sub> treatment and second annealing in order to avoid removal by the TiCl<sub>4</sub> treatment. These cells were annealed a 3<sup>rd</sup> time using the same profile.

The photoanode was then sensitized using a 0.5 M N-719 dye solution in ethanol for 24 hours. In the case of cells prepared using the NaYF<sub>4</sub>:Yb<sup>3+</sup>,Er<sup>3+</sup> and NaYF<sub>4</sub>:Yb<sup>3+</sup>,Er<sup>3+</sup>@TiO<sub>2</sub> (DIW:TEOT, 3:1) scattering pastes, a longer sensitization time of 72 hours was needed.

A platinized counter-electrode was produced using pre-drilled FTO glass cleaned in a similar fashion to the photoanode. A drop ( $\sim 8~\mu L$ ) of H<sub>2</sub>PtCl<sub>6</sub> (50 mM in isopropanol) was spread across the surface of the counter electrode and annealed at 400 °C for 30 minutes.

The cells were then sealed in a sandwich type configuration using a hot melt ionomer film (Surlyn, 30  $\mu$ m) using a cell assembly machine (E002-1233, Dyesol). The cells were injected with an I<sub>3</sub>-/I- liquid electrolyte (EL-HPE, Dyesol) through the pre-drilled holes, filling via capillary forces. The holes were sealed using a coverslip and the hot melt ioner film.

#### 4.3.3 Characterization

#### 4.3.3.1 Upconvertor Characterization

Powders were characterized before and after annealing by powder x-ray diffraction (XRD), transmission electron microscopy, and upconversion luminescence.

XRD analysis was done using a Bruker Discover D8 diffractometer with  $\lambda_{\text{Cu},K\alpha}$ =1.5406 Å radiation operated at 40 kV and 20 mA. A VANTEC 2000 2D x-ray area detector was used with a 20 frame width of 23° and angular scanning resolution of 0.05°. Four frames were collected for each sample at 50 seconds/frame. Analysis was done using the Eva software package provided by Bruker. TEM analysis was done using a Philips CM200 TEM operated at 200 kV.

Upconversion spectra were collected from 450 nm to 700 nm with 0.5 nm step size and 2 nm emission slit using a Fluoromax-2 spectrophotometer with a 980 nm IR laser diode (100 mW, Startech) as excitation source. The fluorescence was measured using the solid powder; the laser spot size was kept the same when comparing samples, ensuring that the interaction volume and laser intensity was the same from sample to sample. The measurement spectra of all samples were recorded under the same conditions. The position of the laser relative to the samples was identical during all measurements. Each sample was immobilized and pressed between two glass slides to ensure a flat surface and uniform packing, and fixed using a metallic sample holder. All annealed samples were ground using a mortar and pestle prior to measurement to minimize soft agglomeration.

#### 4.3.3.2 Dye-Sensitized Solar Cell Characterization

All DSSCs were characterized using a solar simulator (Class ABA, PV Measurements) calibrated using a silicon reference photodiode. The solar cell characteristics were calculated as an average of the forward and backward voltage sweeps with a voltage settling time of 100 ms for each voltage point in order to properly account for the slow response typical in DSSCs [34]. Cells were properly masked in order to eliminate extra scattered light and edge effects [35]. The active area of all cells measured was 0.25 cm<sup>2</sup>.

Incident photon to electron conversion efficiency (IPCE) was measured using a QEX10 measurement system (PV Measurements) from 300 nm to 1400 nm using silicon and germanium photodiodes with known photoresponse for calibration. Monochromated light was chopped at a frequency of 4 Hz to account for the slow

response of DSSCs. In order to roughly simulate 1 sun conditions in the IPCE, a light bias was used, biasing each cell to its short-circuit current obtained from the IV curve under solar simulation.

Dye loading was calculated by immersing sensitized films in 0.1 M aqueous NaOH dye-desorption for 10 minutes. The UV-visible absorption was measured (Cary 5000), and the concentration calculated using a 0.01 mM dye solution in 0.1 M aqueous NaOH as reference.

Electrochemical impedance spectroscopy was measured using a VSP-potentiostat system (BioLogic) using a Mott-Schottky staircase potential measurement sweep under 1 sun illumination with 12 steps between -0.35 and -0.9 V applied to the photoanode with an additional AC bias of 10 mV applied over a frequency range from 100 kHz to 1 Hz with 6 points per decade. The data was fit using the commercially available Z-View software.

#### 4.4 Results and Discussion

#### 4.4.1 Upconversion Nanocomposites

Hexagonal β-phase NaYF<sub>4</sub>:Yb<sup>3+</sup>,Er<sup>3+</sup> crystals (~300 nm in size) were produced by a citrate modified hydrothermal process [30]. These crystals were then incorporated into a core-shell type nanocomposite material with  $TiO_2$  via directed hydrolysis of titanium ethoxide in ethanol. The water hydrolyzes the titanium ethoxide after which a condensation reaction occurs, depositing amorphous  $TiO_2$  onto the upconverter particle surfaces, according to the following reactions (R =  $C_2H_5$ ) [36]:

$$Ti(OH)_4 + 3H_2O \rightarrow Ti(OR)(OH)_3 + 3ROH$$

and

$$Ti(OR)(OH)_3 \rightarrow TiO_2 \cdot xH_2O + (1-x)H_2O + ROH$$

The rate of reaction and therefore the amount of TiO<sub>2</sub> deposited as a shell depends on the molar ratio of DIW:TEOT and therefore the extent of the hydrolysis reaction.

TEM images are presented in Figure 4.1, showing the difference between the 3:1 DIW:TEOT ratio (UC@T1) and the 6:1 DIW:TEOT ratio (UC@T2) materials.

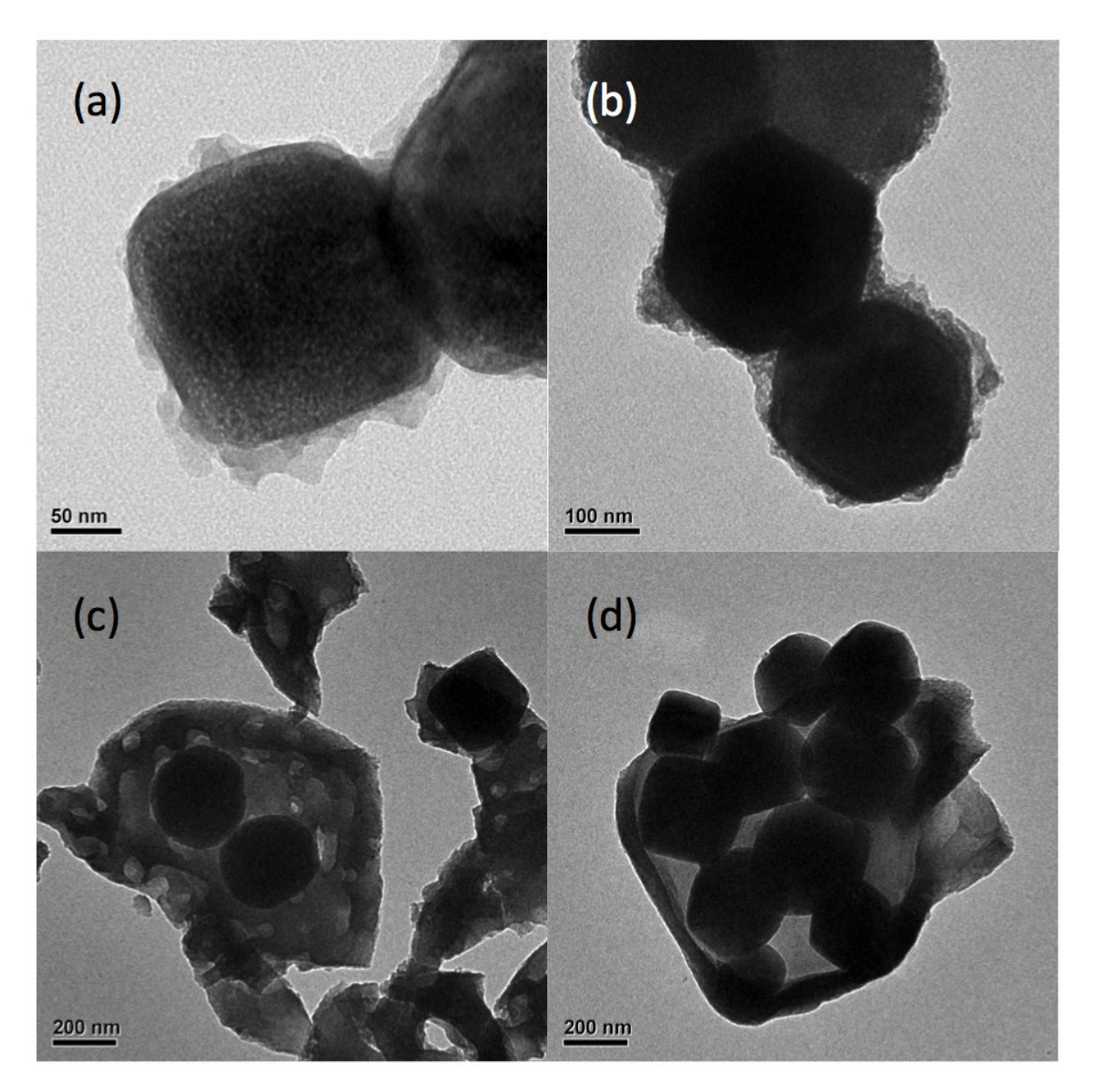


Figure 4.1: TEM images of the UC@TiO<sub>2</sub> nanocomposite materials showing UC@T1 particles produced with 3:1 DIW:TEOT ratio (a,b), and UC@T2 particles produced with 6:1 DIW:TEOT ratio (c,d)

As can be seen, the particles in UC@T1 are covered by an incomplete shell of amorphous  $TiO_2$ , while the particles in UC@T2 are either completely covered by a thicker amorphous  $TiO_2$  shell or embedded into a larger amorphous  $TiO_2$  matrix on the order of  $\sim 1~\mu m$ .

NaYF<sub>4</sub>:Yb<sup>3+</sup>,Er<sup>3+</sup> upconversion materials convert infrared light to both red and green visible light. Both the shape and intensity of the upconversion spectrum is important for proper technological application. The phase of the UC material is also very important in determining both these aspects. The  $\beta$ -hexagonal phase of NaYF<sub>4</sub> is a much better upconverter compared with its  $\alpha$ -cubic counterpart [10]. In addition, the  $\beta$ -phase emits predominantly green light while the  $\alpha$ -phase emits predominantly red. This is an important aspect when engineering these materials for DSSCs as the dye absorbs green light more strongly than red and as a result, the DSSC performs better under green illumination [17], [37]. Since the red and green upconversion processes are competitive, it is important to ensure that the amount of  $\alpha$ -phase is minimized in order to maximize the coupling of the upconverted light to the solar cell. The upconversion fluorescence spectra of the as-prepared UC nanocrystals and the nanocomposite UC materials are shown in Figure 4.2(a).

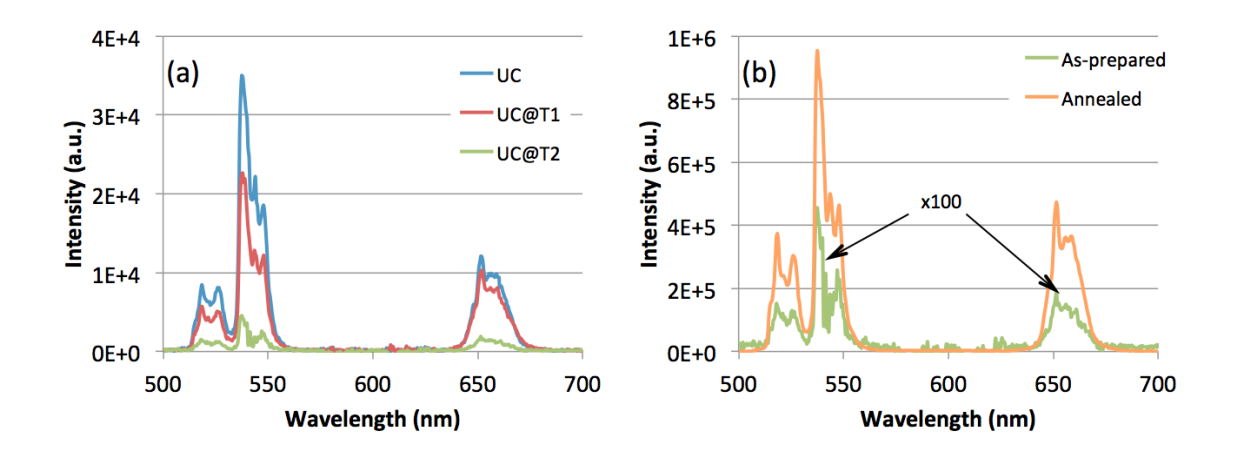


Figure 4.2: Upconversion fluorescence spectra under 980 nm NIR laser illumination showing (a) the difference between the as-prepared UC and the UC@TiO<sub>2</sub> materials, and (b) the difference between the as-prepared UC@T2 material (spectrum multiplied by 100 for easier visual comparison) and the annealed UC@T2 material

The efficiency of the upconversion process in bulk NaYF<sub>4</sub>:Yb<sup>3+</sup>,Er<sup>3+</sup> is modest, and decreases further when the particle size of the crystals is smaller than a few microns [9], as is the case in this study and studied in more detail in Chapter 3. Other studies have increased the upconversion fluorescence intensity by using a core-shell

approach to eliminate non-radiative pathways by separating the upconverting core from the quenching surface states [38], [39]. In the current study, a decrease is observed in Figure 4.2(a) with addition of a  $TiO_2$  shell in the nanocomposite materials. UC@T1 has about 2/3 the upconversion intensity of the as-prepared UC material, while UC@T2 only has about 1/10 the upconversion intensity. This decrease is largely attributed to the decreasing absolute mass of UC crystals being excited due to the lower fraction of UC material in the composite powder as a whole. While it is possible to decouple these effects to see how the presence of the  $TiO_2$  affects upconversion in an equivalent number of excited crystals, in the context of solar cell integration, especially that of internal DSSC application, there are limitations placed on the amount of material that can be used within the cell itself based on the volume of the internal chamber, meaning that the primary concern should be the upconversion of an equivalent volume of scattering material rather than volume of upconverting material. Therefore examining the upconversion fluorescence of the composite powder as a whole is justified.

Another important consideration with regards to upconversion is the presence of organic molecules on the surface of the upconversion particles. The as-prepared particles were modified with citrate in order to control both the particle shape and size [30] (See also Chapter 3). The presence of organic molecules on the surface of upconversion particles has been shown to quench the upconversion fluorescence due to high-energy vibrational modes, and is something that should be avoided for solar cell integration. Annealing is a very effective way to increase the upconversion fluorescence of citrate-modified UC particles both through removal of organics as well as removal of internal defects in the crystal lattice that otherwise quench the upconverted energy states [40] (also demonstrated in Chapter 3). In the case of the DSSCs assembled in this study, a standard DSSC annealing process (at 450 °C) was used to sinter the TiO<sub>2</sub> nanocrystalline layer and remove the organic additives from the pastes used for screen-printing (Figure B.1, Appendix B). Very advantageously, the same sintering process also serves to anneal the printed upconversion scattering layer, resulting in an impressive increase of the upconversion

fluorescence of the UC@T2 material by over 2 orders of magnitude as can be seen in Figure 4.2(b).

Although annealing clearly increases the upconversion fluorescence in the material, it can also cause partial transformation from the  $\beta$ -phase to the  $\alpha$ -phase at temperatures as low as 400 °C [30]. In order to investigate possible phase transformations, XRD was performed on the as-prepared and annealed UC and UC@T2 materials, as shown in Figure 4.3.

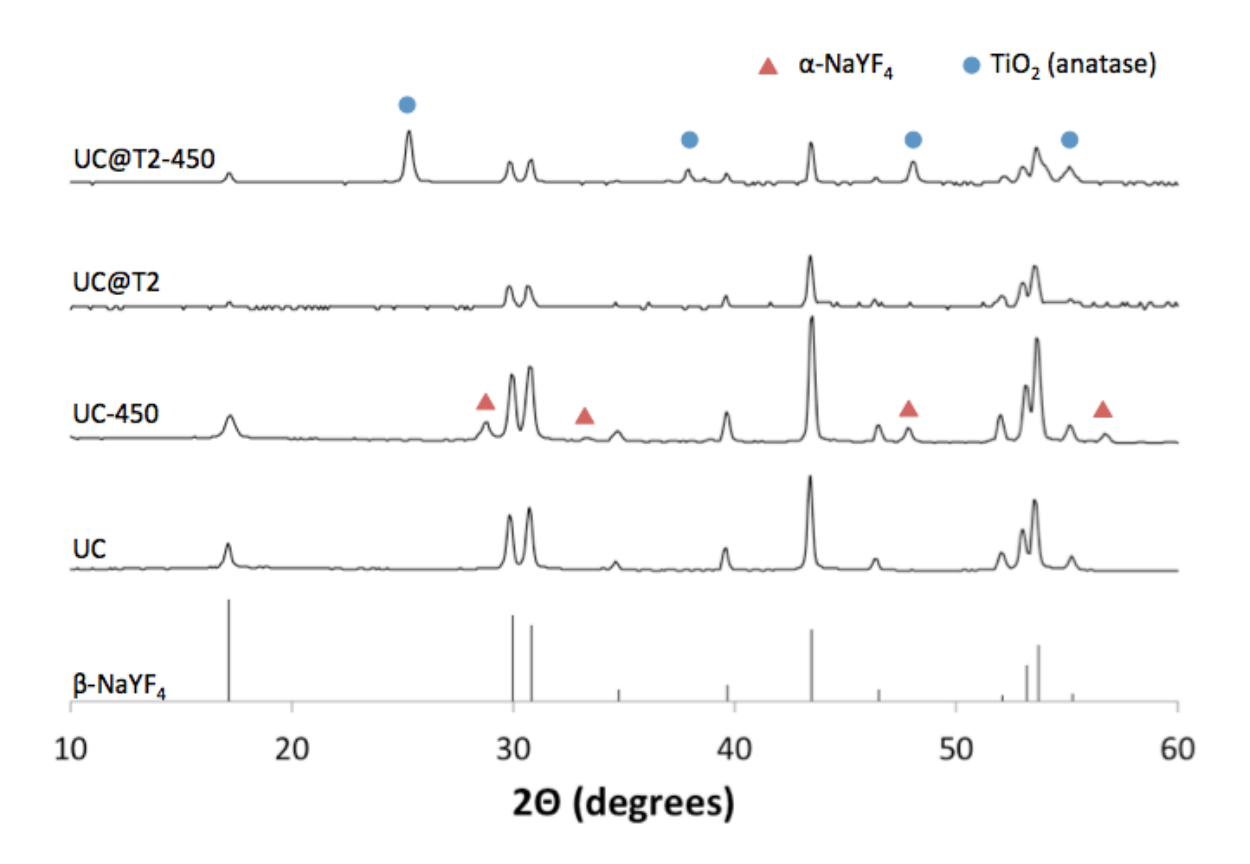


Figure 4.3: Powder XRD results showing the effect of annealing at 450 °C on the uncoated UC material and the UC@TiO<sub>2</sub> material. Reference pattern for  $\beta$ -NaYF<sub>4</sub> (JCPDS 28-1192) is included and peaks corresponding to  $\alpha$ -NaYF<sub>4</sub> and TiO<sub>2</sub> (anatase phase) are indicated with markers

From the XRD traces it can be seen that both UC and UC@T2 as-prepared materials are pure  $\beta$ -NaYF<sub>4</sub>. When sample UC is annealed at 450 °C, a partial transformation to  $\alpha$ -phase is observed as indicated in Figure 4.3, however for the UC@T2 material, we see that the phase transition is suppressed. This preserves the  $\beta$ -phase NaYF<sub>4</sub> of the core particles and helps to maintain a high green-to-red ratio [10]. From the XRD

results we also see appearance of crystalline  $TiO_2$  peaks (anatase) in the annealed UC@T2 material, indicating that the amorphous shell is converted to crystalline  $TiO_2$ .  $TiO_2$  has a number of polymorphs, although anatase has been shown to have the best performance in DSSC devices due to its preferable bandgap and conduction band edge [41], and its presence is important for internal application of upconverter materials [27]. In summary, the annealing process serves as a multifunctional tool, sintering the nanotitania-based photoanode, increasing the upconversion fluorescence, and converting the amorphous  $TiO_2$  to anatase, while the presence of the  $TiO_2$  shell helps to suppress the  $\beta$ -to- $\alpha$  phase transformation, maintaining a high green-to-red ratio.

#### 4.4.2 Dye-Sensitized Solar Cell Integration

The upconvertor materials were incorporated into pastes and screen-printed as scattering layers in DSSC devices. In addition to the 3 types of upconversion materials investigated, 2 types of control devices were also fabricated, one type without a scatter layer, and another using a commercially available scatter paste comprised of ~200 nm anatase nanoparticles. For each type of scatter layer, multiple cells were made and tested under 1 sun illumination. The results are tabulated in Table 4.1, with the current-voltage relationships of selected devices from each series presented in Figure 4.4.

Table 4.1: Detailed PV characteristics for different UC/scattering layers studied. All values are an average of multiple cells made under the same conditions, with the standard deviation of each device set listed as the error on each value.

Scatter Layer	Thickness¹ (μm)		2			4-11	Dye Loading
	tr	sc	$J_{sc}$ (mA/cm <sup>2</sup> )	<i>V<sub>oc</sub></i> (V)	FF	η (%)	(10 <sup>-7</sup> mol/cm <sup>2</sup> )
None	12		12.6 ± 0.6	0.7 ± 0.02	0.71 ± 0.03	6.21 ± 0.5	1.64
UC	12	4	4.1 ± 0.4	0.76 ± 0.01	0.79 ± 0.01	2.48 ± 0.2	1.50
UC@T1	12	4	4.4 ± 0.5	0.76 ± 0.02	0.76 ± 0.05	2.5 ± 0.2	1.36
UC@T2	12	4	13.4 ± 0.2	0.73 ± 0.005	0.74 ± 0.01	7.22 ± 0.1	1.75
WER2-O	12	4	14.6 ± 0.1	0.72 ± 0.01	0.73 ± 0.01	7.73 ± 0.1	1.70

<sup>&</sup>lt;sup>1</sup> tr = transparent, sc = scattering

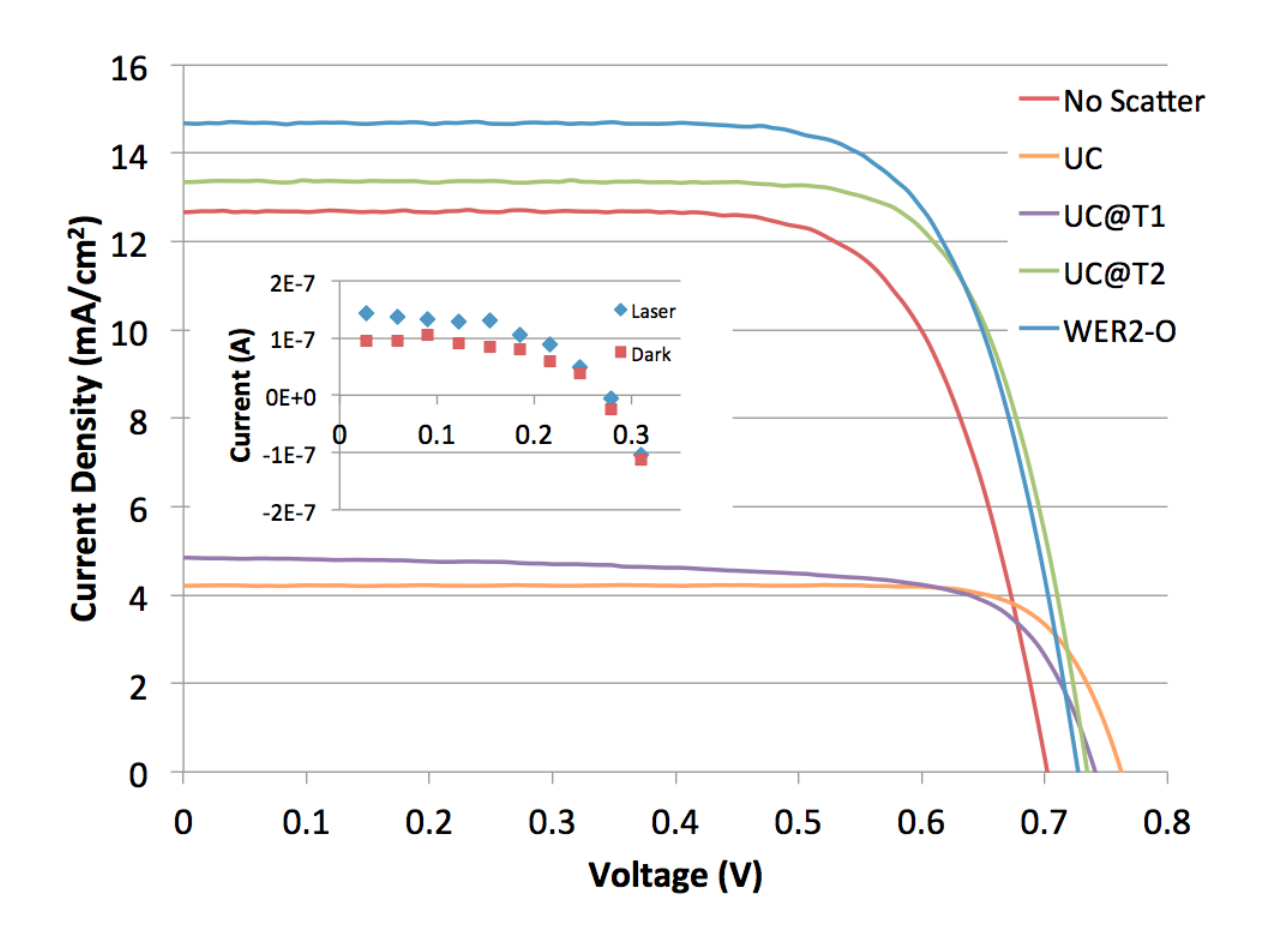


Figure 4.4: Current-voltage characteristics for different UC/scattering layers investigated. Inset: current voltage relationship for UC@TiO2 device under 980 nm laser illumination, illustrating proof-of-concept IR function.

The transparent control device without a scatter layer has an efficiency ( $\eta$ ) of 6.21%, and it is immediately apparent that both the UC and UC@T1 scatter layers result in a severe drop in efficiency to 2.48% and 2.5%, respectively. This difference is due to a drop in the  $J_{sc}$  of the devices from 12.6 mA/cm<sup>2</sup> in the control to 4.1 and 4.4 mA/cm<sup>2</sup> in the UC and UC@T1 devices, respectively. Part of this drop can be attributed to a lower dye loading in the UC and UC@T1 devices, as can be seen in Table 4.1. Both the UC and UC@T1 devices required longer sensitization times, and despite this, the dye loading is still not as high as in the control devices. It is clear that the presence of these layers interferes with the sensitization process and contributes to the decrease in the  $J_{sc}$ . On the other hand, the UC@T2 devices show efficiencies of 7.22%, a 16% relative increase in efficiency over the transparent

control device without scatter layer. This increase comes from both a higher  $J_{sc}$  and  $V_{oc}$ , both of which are characteristic of scattering layers. NIR performance of the device is demonstrated as proof-of-concept with 980 nm laser illumination and is shown in the inset of Figure 4.4. The difference between the dark current and the current under illumination is small, however this can be partially attributed to the very small spot size of the laser. Although an increase in performance is seen in the UC@T2 devices, it does not match the performance of the commercially available scattering layer, WER2-0, which gave the highest efficiencies observed in this study at 7.73%.

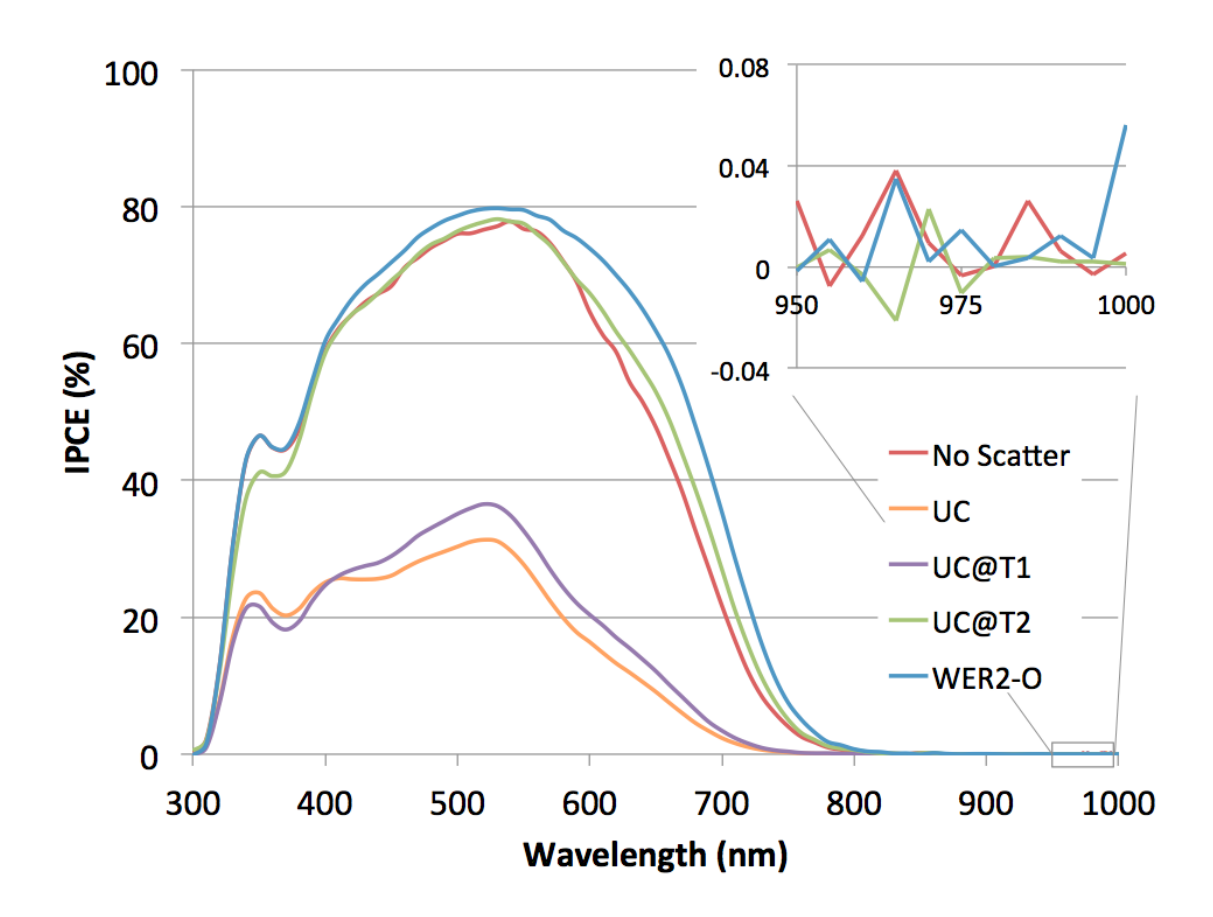


Figure 4.5: Incident photon to electron conversion (IPCE) for different UC/scattering layers studied. All measurements were performed under ~1 sun light bias. Inset: detailed view of device performance in the NIR region.

To further investigate the effect of the  $UC@TiO_2$  scattering layers, the incident photon-electron conversion efficiency (IPCE) was measured, giving the spectral response of the cells. These results are shown in Figure 4.5. From the plot, it can be

seen that the UC and UC@T1 devices have a much lower IPCE than that of the transparent control. The UC@T1 device has a slightly higher IPCE than the UC device, which is attributed to stronger scattering in the UC@T1 device. This was observed visually as a higher degree of transparency observed in the UC scatter layer devices (Figure B.2, Appendix B). The refractive indices of the DSSC electrolyte, NaYF<sub>4</sub>, and TiO<sub>2</sub> are about 1.4, 1.5, and 2.0, respectively. Since scattering relies on large changes in the material refractive index, TiO<sub>2</sub> is a much more effective scattering agent than NaYF<sub>4</sub> and the coated UC@T1 particles scatter more light than the uncoated UC particles.

UC@T2 provides higher IPCE response than the control device without scatter layer in the visible range and even extending slightly into the NIR from 300 nm to 800 nm. The IPCE of the commercial paste shows the highest response.

It is very important to note that the IPCE spectrum shows essentially no response near the absorption range of the  $Yb^{3+}$  ion as shown in the inset of Figure 4.5. If a response is present, it does not exceed the noise of the measurement, corresponding to  $\pm 0.05\%$ . Even if the contributions of upconversion were equivalent to the noise level, it would be negligibly small compared to the benefit coming from scattering. It should be noted that there was also no observable NIR response from the UC and UC@T1 devices (results not shown).

The efficiency,  $\eta_{UC}$ , of an *n*-photon upconversion process is as follows,

$$\eta_{UC} \propto irradiance^{n-1}$$
(4.1)

Where n is the number of photons required for a single upconverted photon (in this case, n = 2). The irradiance power density is therefore very important for evaluating the upconversion performance. The IPCE measurements were carried out using a bias light to roughly simulate 1 sun illumination. Even under the maximum bias light voltage (corresponding only to about 2.5 sun), a measureable response (>0.05%) in the 950-1000 nm region was unattainable. It is possible that higher solar concentration may be able to increase the upconversion contribution, as has been seen experimentally in amorphous silicon solar cell devices [28] as well as in

theoretical calculations in a similar NaYF<sub>4</sub>:Er<sup>3+</sup> upconversion system [8]; however light concentration can cause elevated temperatures in DSSCs, which can cause subsequent problems with other areas of DSSC functioning if not properly handled [42].

While NIR laser illumination can been used to show proof-of-concept upconversion coupling in other studies [21], [22], [27] as well as in the current study, its use should be avoided unless the technological application warrants the power densities used. In the case of photovoltaic application, in the absence of light concentration, this is clearly not the case. Other studies have additionally used an IR-pass filter for demonstration of NIR DSSC performance [21], [26], however this type of measurement is often unable to decouple the scattering effect from the upconversion if the cut-off wavelength of the filter is not selected properly. IPCE measurements under anticipated illumination provide the best assessment of the true contribution from upconversion. As has been seen from the results presented here, that contribution is negligible.

#### 4.4.2.1 Electrochemical Impedance Spectroscopy (EIS)

In order to further understand the impact of the UC scattering layers on the internal functioning of the DSSC, a technique known as electrochemical impedance spectroscopy (EIS) was employed. EIS is a very versatile technique that reveals information about electronic and ionic kinetics at work in the solar cell.

In order to extract the various operational parameters of the solar cell, an equivalent circuit originally developed by Fabregat-Santiago *et al.* [43], [44], was used to fit the impedance data. The model, shown in Figure 4.6 includes a number of useful performance parameters including the series resistance of the solar cell,  $R_{s}$ , the transport resistance,  $r_{tr}$ , the chemical capacitance,  $c_{\mu}$ , and the charge transfer resistance from the TiO<sub>2</sub> to the electrolyte,  $r_{CT}$ . For the fitting, all capacitors were treated as constant phase elements.

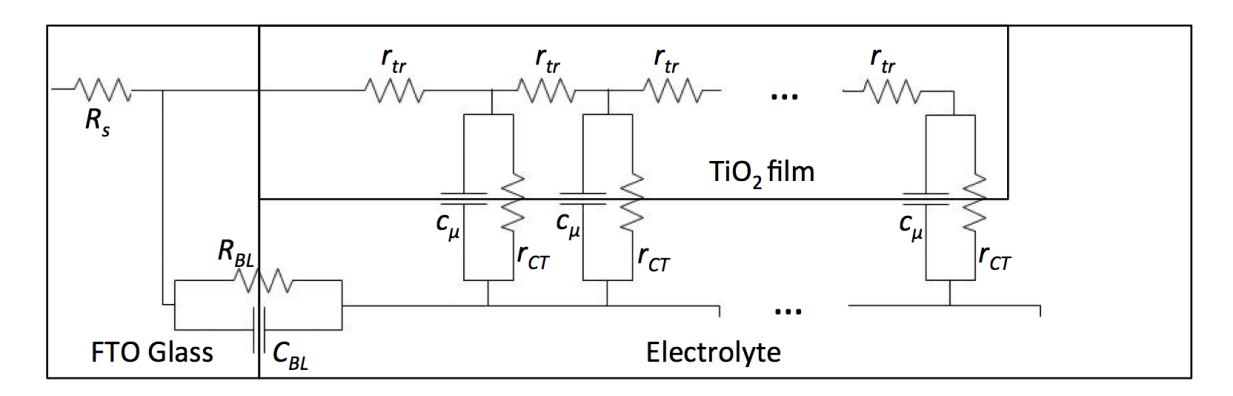


Figure 4.6: Equivalent circuit used for extraction of solar cell performance parameters, originally developed by Fabregat-Santiago *et al.* [43], [44]

The chemical capacitance of the film,  $C_{\mu}$  (=  $c_{\mu}L$ ) is plotted in Figure 4.7(a) against the Fermi voltage ( $V_F$ ) of the film.  $V_F$  is proportional to the Fermi level of the electrons in the nanocrystalline TiO<sub>2</sub> and is calculated by removing the voltage drop due to series resistance ( $R_S$ ) in the solar cell by using the following equation [44]:

$$V_F = V_{app} - V_S = V_{app} + jR_S (4.2)$$

The primary pathway for loss of excited carriers is via electron recombination from the conduction band of the  $TiO_2$  to the electrolyte, which is dictated by the recombination resistance,  $R_{rec}$  (=  $r_{CT}/L$ ). The recombination resistance is proportional to the position of the  $TiO_2$  conduction band, which can be displaced through the use of different dyes, electrolytes, and pastes [44]. As such, a voltage shift,  $\Delta E_c$ , must be introduced, with  $R_{rec}$  being plotted against an "equivalent conduction band" potential,  $V_{ecd} = V_F - \Delta E_C / q$ .

This is accomplished by shifting the  $C_{\mu}$  plot so that all curves overlap in relation to a reference sample (in this case, the control without scatting layer), as is seen in Figure 4.7(b).

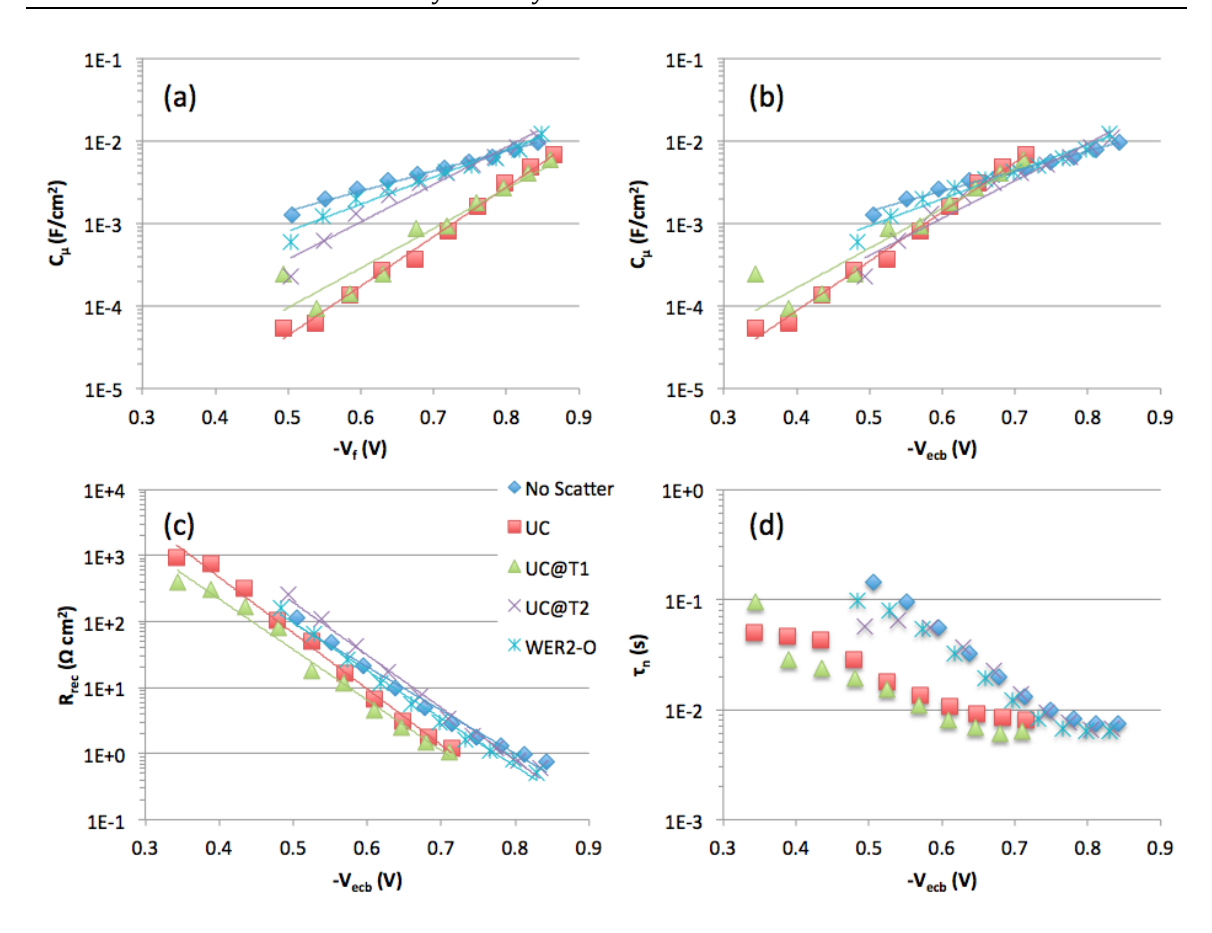


Figure 4.7: Electrochemical impedance spectroscopy (EIS) of different UC/scattering layers investigated under 1 sun illumination, showing (a) chemical capacitance,  $C_{\mu}$ , plotted against  $V_{F}$ , (b) chemical capacitance,  $C_{\mu}$ , plotted against  $V_{ecb}$ , (c) recombination resistance,  $R_{rec}$ , plotted against  $V_{ecb}$ , and (d) carrier lifetime,  $\tau_n$ , plotted against  $V_{ecb}$ .

 $R_{rec}$  can now be plotted vs.  $V_{ecb}$  as shown in Figure 4.7(c). The recombination resistance is similar in the control device without scattering layer, the UC2@T2, and the WER2-O devices, while it is lower in the UC and UC@T1 devices indicating increased recombination rates. These increased recombination rates are the primary reason for the  $J_{sc}$  decreases seen in the UC and UC@T1 devices (see Figure 4.4 and Table 4.1). Similarly, the electron lifetime can be calculated using the equation,  $\tau_n = R_{rec}C_\mu$  and is plotted in Figure 4.7(d), showing lower electron lifetimes in the UC and UC@T1 devices. These results agree with other similar studies that have suggested the presence of internal NaYF4 upconversion particles contributes to electron recombination and therefore a reduction in overall device efficiency [22]. The UC device has the lowest efficiency (2.48%), which only

marginally increases with the UC@T1 device (2.5%). Both the UC and UC@T1 devices have poor recombination resistance, and the UC@T1 device actually has lower electron lifetimes, so the marginal increase in efficiency must be primarily attributed to the difference coming from scattering as already discussed. It is only in the UC@T2 devices, when the UC particles are fully coated/embedded into TiO<sub>2</sub>, that the recombination resistance and electron lifetime of the control device is recovered.

While integration of these upconversion materials provides essentially no added benefit via upconversion, the method used for integrating them allows recovery of the recombination resistance as well as reasonably effective light scattering. This approach could be applicable to other efforts to maximize light harvesting such as the use of quantum dots or plasmonic light coupling [45]–[47].

#### 4.5 Conclusions

Citrate-modified NaYF<sub>4</sub>:Yb<sup>3+</sup>,Er<sup>3+</sup> NIR-to-visible upconversion nanocrystals as well as NaYF<sub>4</sub>:Yb<sup>3+</sup>,Er<sup>3+</sup>@TiO<sub>2</sub> nanocomposite materials have been integrated into DSSC devices as internal scattering layers. The upconversion effect of the materials has been demonstrated. The upconversion fluorescence of the  $TiO_2$  coated UC@T2 nanocomposite material was 10 times lower than its uncoated nanocrystals counterpart, which was attributed to lower upconverting material mass in an equivalent volume. This drop in fluorescence was more than compensated for when the material is subjected to an annealing profile used in DSSC sintering, with over 2 orders of magnitude increase in the upconversion fluorescence.

Integration of the as-prepared UC nanocrystals as an internal layer causes a dramatic decrease in efficiency that is attributed to an increase in electron recombination from the TiO<sub>2</sub> to the electrolyte caused by the presence of the NaYF<sub>4</sub> upconversion crystals. Coating the upconversion particles with a layer of TiO<sub>2</sub> ("core-shell" configuration) helps to eliminate the charge recombination as well as resulting in an overall efficiency of 7.22%, a relative increase of 16% over a control device without a scattering layer (6.21%). This increase is attributed entirely to

scattering, with no measurable IPCE response (>0.05%) in the 950-1000 nm region, where upconversion via the Yb³+-Er³+ couple should, in principle, be occurring. In addition to this, the UC@TiO₂ device is unable to match the efficiency of a commercially available scattering paste, WER2-O (7.73%). While the concept of upconversion is theoretically compelling, and a number of studies have endeavoured to integrate upconversion materials into solar cell devices, its use is highly impractical with currently available materials. Despite this, the methods for integration of upconversion materials through deposition of TiO₂ can be applied to maximize light harvesting in other materials such as novel plasmonic and semiconductor nanostructures.

#### 4.6 Acknowledgments

This work was funded by NSERC through a strategic project grant to G. P. Demopoulos and sponsored by Targray Technology International, Versatilis, CIS Solar, Hydro-Quebec's IREQ, and Dupont. N. Dyck is also the recipient of an Alexander Graham Bell CGS Scholarship from NSERC.

#### 4.7 References

- [1] W. Shockley and H. J. Queisser, "Detailed Balance Limit of Efficiency of p-n Junction Solar Cells," *Journal of Applied Physics*, vol. 32, no. 3, p. 510, 1961.
- [2] J. Zhao, A. Wang, M. A. Green, and F. Ferrazza, "19.8% Efficient 'Honeycomb' Textured Multicrystalline and 24.4% Monocrystalline Silicon Solar Cells," *Applied Physics Letters*, vol. 73, no. 14, p. 1991, 1998.
- [3] B. O'Regan and M. Grätzel, "A low-cost, high-efficiency solar cell based on dye-sensitized colloidal TiO<sub>2</sub> films," *Nature*, vol. 353, no. 6346, pp. 737–740, 1991.
- [4] "Best Research-Cell Efficiencies," *NREL*, 2013. [Online]. Available: http://www.nrel.gov/ncpv/images/efficiency\_chart.jpg. [Accessed: 17-Jun-2013].
- [5] R. F. Service, "Solar energy. Outlook brightens for plastic solar cells.," *Science*, vol. 332, no. 6027, p. 293, 2011.
- [6] S. Benagli, D. Borrello, E. Vallat-Sauvain, J. Meier, U. Kroll, J. Hötzel, J. Bailat, J. Steinhauser, M. Marmelo, G. Monteduro, and L. Castens, "High-Efficiency Amorphous Silicon Devices on LPCVD-ZnO TCO Prepared in Industrial KAI TM-M R&D Reactor," in *European Photovoltaic Solar Energy Conference and Exhibition*, 2009, no. September, pp. 21–25.
- [7] A. H. Ip, S. M. Thon, S. Hoogland, O. Voznyy, D. Zhitomirsky, R. Debnath, L. Levina, L. R. Rollny, G. H. Carey, A. Fischer, K. W. Kemp, I. J. Kramer, Z. Ning, A. J. Labelle, K. W. Chou, A. Amassian, and E. H. Sargent, "Hybrid passivated colloidal quantum dot solids.," *Nature Nanotechnology*, vol. 7, no. 9, pp. 577–82, 2012.
- [8] A. Shalav, B. S. Richards, and M. A. Green, "Luminescent layers for enhanced silicon solar cell performance: Up-conversion," *Solar Energy Materials and Solar Cells*, vol. 91, no. 9, pp. 829–842, 2007.
- [9] F. Auzel, "Upconversion and anti-Stokes processes with f and d ions in solids.," *Chemical Reviews*, vol. 104, no. 1, pp. 139–73, 2004.
- [10] K. Kramer, D. Biner, G. Frei, and H. Gudel, "Hexagonal sodium yttrium fluoride based green and blue emitting upconversion phosphors," *Chemistry of Materials*, vol. 16, no. 7, pp. 1244–1251, 2004.
- [11] G. Yi, H. Lu, S. Zhao, Y. Ge, W. Yang, D. Chen, and L.-H. Guo, "Synthesis, Characterization, and Biological Application of Size-Controlled Nanocrystalline NaYF<sub>4</sub>:Yb,Er Infrared-to-Visible Up-Conversion Phosphors," *Nano Letters*, vol. 4, no. 11, pp. 2191–2196, 2004.
- [12] Z. Chen, L. Zhang, Y. Sun, J. Hu, and D. Wang, "980-nm Laser-Driven Photovoltaic Cells Based on Rare-Earth Up-Converting Phosphors for Biomedical Applications," *Advanced Functional Materials*, vol. 19, no. 23, pp. 3815–3820, 2009.

- [13] X. Yu, M. Li, M. Xie, L. Chen, Y. Li, and Q. Wang, "Dopant-controlled synthesis of water-soluble hexagonal NaYF<sub>4</sub> nanorods with efficient upconversion fluorescence for multicolor bioimaging," *Nano Research*, vol. 3, no. 1, pp. 51–60, 2010.
- [14] E. Downing, L. Hesselink, J. Ralston, and R. Macfarlane, "A Three-Color, Solid-State, Three-Dimensional Display," *Science*, vol. 273, pp. 1185–1189, 1996.
- [15] F. F. Zhang, Y. Wan, T. Yu, Y. Shi, S. Xie, Y. Li, L. Xu, B. Tu, and D. Zhao, "Uniform Nanostructured Arrays of Sodium Rare-Earth Fluorides for Highly Efficient Multicolor Upconversion Luminescence," *Angewandte Chemie*, vol. 119, no. 42, pp. 8122–8125, 2007.
- [16] R. A. McFarlane, "High-power visible upconversion laser," *Optics Letters*, vol. 16, no. 18, pp. 1397–9, 1991.
- [17] G.-B. Shan and G. P. Demopoulos, "Near-infrared sunlight harvesting in dyesensitized solar cells via the insertion of an upconverter-TiO<sub>2</sub> nanocomposite layer.," *Advanced Materials*, vol. 22, no. 39, pp. 4373–7, 2010.
- [18] J. de Wild, A. Meijerink, J. K. Rath, W. G. J. H. M. van Sark, and R. E. I. Schropp, "Upconverter solar cells: materials and applications," *Energy & Environmental Science*, vol. 4, no. 12, pp. 4835–4848, 2011.
- [19] G.-B. Shan, H. Assaaoudi, and G. P. Demopoulos, "Enhanced Performance of Dye-Sensitized Solar Cells by Utilization of an External, Bifunctional Layer Consisting of Uniform β-NaYF<sub>4</sub>:Er<sup>3+</sup>/Yb<sup>3+</sup> Nanoplatelets," *ACS Applied Materials & Interfaces*, vol. 3, no. 9, pp. 3239–3243, 2011.
- [20] Y. Y. Cheng, B. Fückel, R. W. MacQueen, T. Khoury, R. G. C. R. Clady, T. F. Schulze, N. J. Ekins-Daukes, M. J. Crossley, B. Stannowski, K. Lips, and T. W. Schmidt, "Improving the light-harvesting of amorphous silicon solar cells with photochemical upconversion," *Energy & Environmental Science*, vol. 5, no. 5, pp. 6953–6959, 2012.
- [21] Y. Li, K. Pan, G. Wang, B. Jiang, C. Tian, W. Zhou, Y. Qu, S. Liu, L. Feng, and H. Fu, "Enhanced photoelectric conversion efficiency of dye-sensitized solar cells by the incorporation of dual-mode luminescent NaYF<sub>4</sub>:Yb<sup>3+</sup>/Er<sup>3+</sup>.," *Dalton Transactions*, vol. 42, no. 22, pp. 7971–9, 2013.
- [22] L. Liang, Y. Liu, and X.-Z. Zhao, "Double-shell β-NaYF<sub>4</sub>:Yb<sup>3+</sup>, Er<sup>3+</sup>/SiO<sub>2</sub>/TiO<sub>2</sub> submicroplates as a scattering and upconverting layer for efficient dyesensitized solar cells.," *Chemical Communications*, vol. 49, no. 38, pp. 3958–60, 2013.
- [23] Y. Li, G. Wang, K. Pan, B. Jiang, C. Tian, W. Zhou, and H. Fu, "NaYF<sub>4</sub>:Er<sup>3+</sup>/Yb<sup>3+</sup>– graphene composites: preparation, upconversion luminescence, and application in dye-sensitized solar cells," *Journal of Materials Chemistry*, vol. 22, no. 38, p. 20381, 2012.
- [24] C. Yuan, G. Chen, P. N. Prasad, T. Y. Ohulchanskyy, Z. Ning, H. Tian, L. Sun, and H. Ågren, "Use of colloidal upconversion nanocrystals for energy relay solar

- cell light harvesting in the near-infrared region," *Journal of Materials Chemistry*, vol. 22, no. 33, p. 16709, 2012.
- [25] C. Han, H. Lee, and K. Lee, "Synthesis of Amorphous Er<sup>3+</sup>-Yb<sup>3+</sup> Co-doped TiO<sub>2</sub> and Its Application as a Scattering Layer for Dye-sensitized Solar Cells," *Bulletin of the Korean Chemical Society*, vol. 30, no. 1, pp. 219–223, 2009.
- [26] J. Wang, J. Lin, J. Wu, M. Huang, Z. Lan, Y. Chen, S. Tang, L. Fan, and Y. Huang, "Application of Yb<sup>3+</sup>, Er<sup>3+</sup>-doped yttrium oxyfluoride nanocrystals in dyesensitized solar cells," *Electrochimica Acta*, vol. 70, pp. 131–135, 2012.
- [27] J. Zhang, H. Shen, W. Guo, S. Wang, C. Zhu, F. Xue, J. Hou, H. Su, and Z. Yuan, "An upconversion NaYF<sub>4</sub>:Yb<sup>3+</sup>,Er<sup>3+</sup>/TiO<sub>2</sub> core–shell nanoparticle photoelectrode for improved efficiencies of dye-sensitized solar cells," *Journal of Power Sources*, vol. 226, pp. 47–53, 2013.
- [28] J. de Wild, T. F. Duindam, J. K. Rath, A. Meijerink, W. G. J. H. M. van Sark, and R. E. I. Schropp, "Increased Upconversion Response in a-Si:H Solar Cells With Broad-Band Light," *IEEE Journal of Photovoltaics*, vol. 3, no. 1, pp. 17–21, 2013.
- [29] X. Wu, G. Q. Max Lu, and L. Wang, "Dual-Functional Upconverter-Doped TiO<sub>2</sub> Hollow Shells for Light Scattering and Near-Infrared Sunlight Harvesting in Dye-Sensitized Solar Cells," *Advanced Energy Materials*, vol. 3, no. 6, pp. 704–707, 2013.
- [30] H. Assaaoudi, G.-B. Shan, N. Dyck, and G. P. Demopoulos, "Annealing-induced ultra-efficient NIR-to-VIS upconversion of nano-/micro-scale α and β NaYF<sub>4</sub>:Er<sup>3+</sup>,Yb<sup>3+</sup> crystals," *CrystEngComm*, vol. 15, no. 23, pp. 4739–4746, 2013.
- [31] D. Zhang, D. Zhao, K. Zheng, N. Liu, and W. Qin, "Synthesis and Upconversion Luminescence of NaYF<sub>4</sub>:Yb, Tm/TiO<sub>2</sub> Core/Shell Nanoparticles with Controllable Shell Thickness," *Journal of Nanoscience and Nanotechnology*, vol. 11, no. 11, pp. 9761–9764, 2011.
- [32] C. Charbonneau, R. Gauvin, and G. P. Demopoulos, "Aqueous Solution Synthesis of Crystalline Anatase Nanocolloids for the Fabrication of DSC Photoanodes," *Journal of The Electrochemical Society*, vol. 158, no. 3, p. H224, 2011.
- [33] S. Ito and P. Chen, "Fabrication of screen-printing pastes from TiO<sub>2</sub> powders for dye-sensitised solar cells," *Progress in Photovoltaics: Research and Applications*, vol. 15, no. May, pp. 603–612, 2007.
- [34] X. Yang, M. Yanagida, and L. Han, "Reliable evaluation of dye-sensitized solar cells," *Energy & Environmental Science*, vol. 6, no. 1, p. 54, 2013.
- [35] H. Snaith, "The perils of solar cell efficiency measurements," *Nature Photonics*, vol. 6, no. June, pp. 337–340, 2012.

- [36] E. Barringer and H. Bowen, "High-purity, monodisperse TiO<sub>2</sub> powders by hydrolysis of titanium tetraethoxide. 1. Synthesis and physical properties," *Langmuir*, vol. 1, no. 4, pp. 414–420, 1985.
- [37] K. Fantai, D. Songyuan, and W. Kongjia, "Purification of Bipyridyl Ruthenium Dye and Its Application in Dye-Sensitized Solar Cells," *Plasma Science and Technology*, vol. 8, no. 5, pp. 3–7, 2006.
- [38] H. Mai and Y. Zhang, "Highly efficient multicolor up-conversion emissions and their mechanisms of monodisperse NaYF<sub>4</sub>: Yb, Er core and core/shell-structured nanocrystals," *The Journal of Physical Chemistry C*, vol. 111, no. 37, pp. 13721–13729, 2007.
- [39] G. Yi and G. Chow, "Water-Soluble NaYF<sub>4</sub>:Yb,Er(Tm)/NaYF<sub>4</sub>/Polymer Core/Shell/Shell Nanoparticles with Significant Enhancement of Upconversion Fluorescence," *Chemistry of Materials*, vol. 19, no. 3, pp. 341–343, 2007.
- [40] Y. Wang, L. Tu, J. Zhao, and Y. Sun, "Upconversion luminescence of  $\beta$ -NaYF<sub>4</sub>: Yb<sup>3+</sup>, Er<sup>3+</sup>@  $\beta$ -NaYF<sub>4</sub> core/shell nanoparticles: Excitation power density and surface dependence," *The Journal of Physical Chemistry C*, vol. 113, no. 17, pp. 7164–7169, 2009.
- [41] A. Hagfeldt, G. Boschloo, L. Sun, L. Kloo, and H. Pettersson, "Dye-sensitized solar cells.," *Chemical Reviews*, vol. 110, no. 11, pp. 6595–663, 2010.
- [42] N. Jiang, T. Sumitomo, T. Lee, A. Pellaroque, O. Bellon, D. Milliken, and H. Desilvestro, "High temperature stability of dye solar cells," *Solar Energy Materials and Solar Cells*, p. http://dx.doi.org/10.1016/j.solmat.2013.04.017, 2013.
- [43] F. Fabregat-Santiago, J. Bisquert, G. Garcia-Belmonte, G. Boschloo, and A. Hagfeldt, "Influence of electrolyte in transport and recombination in dyesensitized solar cells studied by impedance spectroscopy," *Solar Energy Materials and Solar Cells*, vol. 87, no. 1–4, pp. 117–131, 2005.
- [44] F. Fabregat-Santiago, G. Garcia-Belmonte, I. Mora-Seró, and J. Bisquert, "Characterization of nanostructured hybrid and organic solar cells by impedance spectroscopy.," *Physical Chemistry Chemical Physics: PCCP*, vol. 13, no. 20, pp. 9083–118, 2011.
- [45] C. Hägglund, M. Zäch, and B. Kasemo, "Enhanced charge carrier generation in dye sensitized solar cells by nanoparticle plasmons," *Applied Physics Letters*, vol. 92, no. 1, p. 013113, 2008.
- [46] J. Qi, X. Dang, P. Hammond, and A. Belcher, "Highly Efficient Plasmon-Enhanced Dye-Sensitized Solar Cells through Metal@Oxide Core-Shell Nanostructure," *ACS Nano*, vol. 5, no. 9, pp. 7108–7116, 2011.
- [47] Z. Yang, C.-Y. Chen, P. Roy, and H.-T. Chang, "Quantum dot-sensitized solar cells incorporating nanomaterials.," *Chemical Communications*, vol. 47, pp. 9561–9571, 2011.

### **Chapter 5: Synopsis**

In this chapter, an overview of the conclusions is presented and recommendations on future work are provided.

#### **5.1** Global Conclusions

In this work the possible enhancement of the conversion efficiency of dye-sensitized solar cells via integration of NIR-to-Vis upconverting NaYF<sub>4</sub>:Yb,Er crystals was investigated. In Chapter 3, maximization of upconversion efficiency was sought via annealing following hydrothermal synthesis of different sized crystals. In Chapter 4, one of the developed UC crystal crops was properly coated with  $TiO_2$  and used as internal scattering layer. The major global conclusions from this dual part study are given below.

Annealing was successfully used to drastically increase the upconversion fluorescence in a number of different sized hexagonal NaYF4:Yb,Er prism-like crystals obtained via the use of sodium citrate as crystal modifying agent during hydrothermal synthesis. Particle morphology is altered as the temperature of the annealing process is increased, following a general progression: first particle roughening, followed by particle agglomeration, followed by particle growth and transformation to bulk sized particles. The onset temperature of these transitions depends on the initial particle size and therefore can be optimized. Annealing serves to increase the upconversion through a number of ways. The increases are primarily attributed to removal of surface organic groups that otherwise serve as recombination centers for the upconverted energy states, however removal of internal crystal defects is also a contributing reason for the increase in upconversion fluorescence.

Through optimization, 300 nm particles were produced and annealed achieving quantum yields of 2.5%, an increase of 2 orders of magnitude over the as-prepared particles. This achievement approaches the quantum yields of corresponding bulk

particles and is especially notable as particles of this size typically suffer from lower upconversion.

The method used illustrates the broad applicability of a simple annealing process to increase the upconversion fluorescence of a given upconversion material. The process should be optimized depending on the particle size and shape of interest as well as technological application.

having established optimum annealing conditions for maximizing After upconversion efficiency, the 300 nm material was selected to be integrated as an internal light-harvesting layer in DSSCs. Integration of NaYF4:Yb,Er crystals alone was found to interfere with the electrical operation of the DSSC, decreasing overall performance due to increased charge recombination at the photoanode/electrolyte interface. When the upconversion materials are coated with an appropriate amount of TiO<sub>2</sub>, the recombination resistance of the cell is recovered, and a relative increase of 16% in overall efficiency under simulated solar illumination is achieved over cells without UC scattering layers. While this result is encouraging for integration of these materials as internal layers, further investigation via IPCE demonstrates that this increase is essentially entirely from light scattering with negligible contribution from upconversion, even under elevated illumination of 2.5 suns. Proof-of-concept upconversion coupling is demonstrated with NIR laser illumination, demonstrating that the upconverted light can be coupled to the DSSC, but only under high NIR power densities not representative of normal solar illumination. As such it is concluded that, at least for the upconverter investigated in this study, upconversion does not seem to hold a lot of practical promise as effective means of enhancing the efficiency of DSSCs via near infrared light harvesting.

Despite the ineffectiveness of upconversion materials to be useful under standard solar illumination, the results and methods from the present study can be valuable in other applications such as use of UC materials in other than PV fields or integration of other than UC light harvesting materials into DSSCs, such as plasmonic nanoparticles and quantum-dots.

#### 5.2 Recommendations for Future Work

Given the essential lack of measurable upconversion effect under standard solar illumination as well as the likely high cost of these relatively exotic materials, other alternative upconversion materials aside from than rare-earth doped upconverters investigated here may need to be considered in future research [1].

Although the upconversion effect is negligible under 1 sun illumination, another avenue of research into the effect of solar concentration could be investigated as was done in a very recent paper by de Wild *et al.* [2]. While solar concentration in classic DSSC technology may not be feasible due to the liquid electrolyte, upconversion may still be useful for emerging mesoscopic solar cell technologies based on the DSSC architecture [3], [4]. There also still may be applicability of current materials under solar concentration, of which little research has been devoted in literature thus far.

It may also be beneficial to further optimize the  $TiO_2$  coating process presented in Chapter 4. This may help to recover a measureable upconversion response, albeit small, in performance under 1 sun illumination. In addition, this optimization could be useful for integration of future functional materials, upconverting or otherwise.

#### 5.3 References

- [1] Y. Y. Cheng, B. Fückel, T. Khoury, R. G. C. R. Clady, M. J. Y. Tayebjee, N. J. Ekins-Daukes, M. J. Crossley, and T. W. Schmidt, "Kinetic Analysis of Photochemical Upconversion by Triplet–Triplet Annihilation: Beyond Any Spin Statistical Limit," *The Journal of Physical Chemistry Letters*, vol. 1, no. 12, pp. 1795–1799, 2010.
- [2] J. de Wild, A. Meijerink, J. K. Rath, W. G. J. H. M. van Sark, and R. E. I. Schropp, "Upconverter solar cells: materials and applications," *Energy & Environmental Science*, vol. 4, no. 12, pp. 4835–4848, 2011.

- [3] M. M. Lee, J. Teuscher, T. Miyasaka, T. N. Murakami, and H. J. Snaith, "Efficient hybrid solar cells based on meso-superstructured organometal halide perovskites.," *Science*, vol. 338, no. 6107, pp. 643–7, 2012.
- [4] H.-S. Kim, C.-R. Lee, J.-H. Im, K.-B. Lee, T. Moehl, A. Marchioro, S.-J. Moon, R. Humphry-Baker, J.-H. Yum, J. E. Moser, M. Grätzel, and N.-G. Park, "Lead iodide perovskite sensitized all-solid-state submicron thin film mesoscopic solar cell with efficiency exceeding 9%.," *Scientific Reports*, vol. 2, p. 591, 2012.

# **Appendix A: Chapter 3 Supporting Information<sup>2</sup>**

A sample upconversion fluorescence spectrum is shown in Figure A.1, demonstrating upconversion from NIR (980 nm) to visible (green and red).

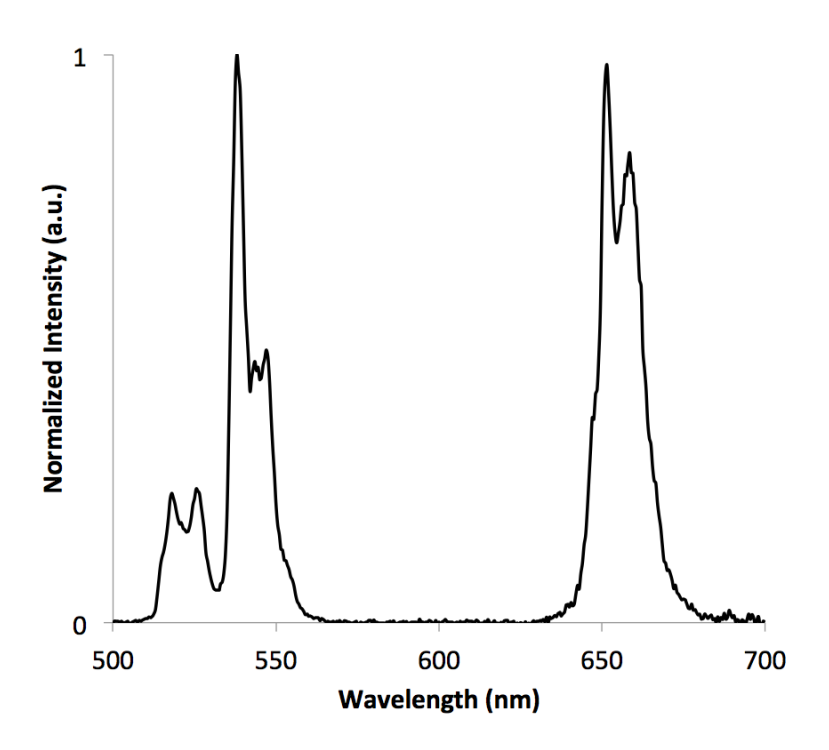


Figure A.1: Upconversion fluorescence under NIR (980nm) laser excitation. Data taken from UC1-600 sample.

Spectra were obtained from all samples. Peaks were integrated to obtain values for green emission (500-575 nm) and red emission (625-700 nm), which are presented in Table A.1, along with the green-to-red ratios of the upconverting samples.

91

 $<sup>^{\</sup>rm 2}$  This section represents the supporting information for the manuscript presented in Chapter 3

Table A.1: Raw integrated values for upconverted fluorescence and green-to-red ratios

Comple	Temperature	Integra	Green-to-		
Sample	(°C)	Green	Red	Total	Red Ratio
	Hydrothermal	1.8E+01	2.9E+01	4.7E+01	0.64
	400	2.2E+02	3.8E+02	6.0E+02	0.60
UC1	500	1.5E+03	1.6E+03	3.1E+03	0.95
	600	1.0E+04	7.9E+03	1.8E+04	1.26
	700	2.0E+02	2.1E+03	2.3E+03	0.09
UC2	Hydrothermal	1.2E+01	2.1E+01	3.3E+01	0.59
	400	3.0E+02	5.4E+02	8.5E+02	0.56
	500	8.3E+03	1.0E+04	1.8E+04	0.83
	600	9.6E+02	1.1E+03	2.0E+03	0.90
	700	2.9E+01	5.9E+02	6.2E+02	0.05
UC3	Hydrothermal	1.5E+01	1.2E+01	2.7E+01	1.28
	350	1.7E+03	3.8E+03	5.6E+03	0.45
	400	3.5E+03	6.0E+03	9.6E+03	0.58
	500	7.4E+03	1.0E+04	1.7E+04	0.74
	600	3.8E+03	4.2E+03	7.9E+03	0.91
	700	4.9E+02	7.8E+03	8.2E+03	0.06

Thermogravimetric analysis (TGA) was performed for the UC3 sample to determine the temperature at which the organic citrate groups were removed from the particle surfaces. As is shown in Figure A.1, this temperature was determined to be  $\sim 372$  °C based on the first derivative peak.

Quantum yield was calculated from the data presented in Figure A.3.  $E_{emission}$  was calculated as the integral of the corresponding peaks in Figure A.3(a): green emission (500-575 nm) and red emission (625-700 nm).  $E_{ref}$  and  $E_{sample}$  were calculated as the integral of the dotted and solid lines, respectively, in Figure A.3(b).

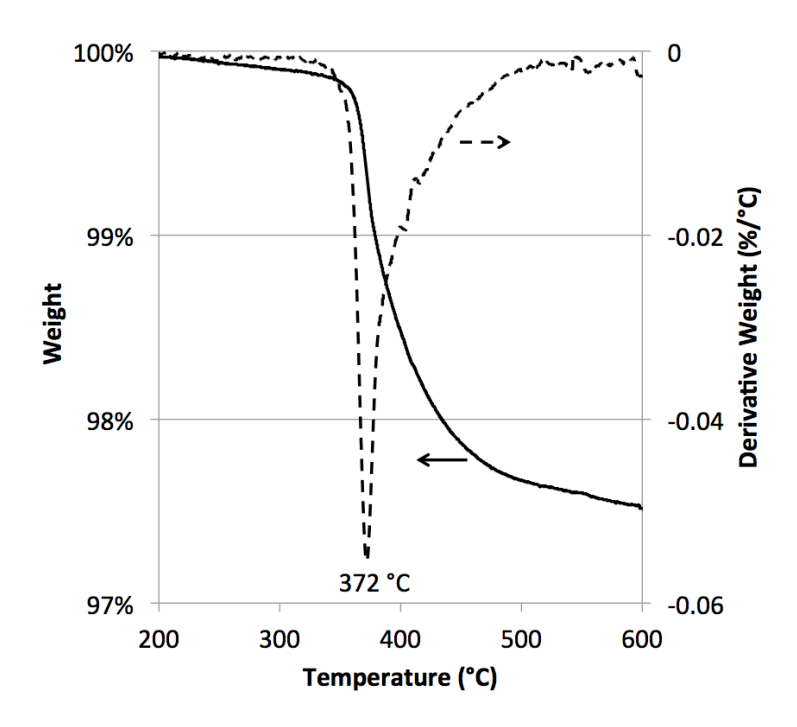


Figure A.2: TGA scan at  $20^{\circ}$ C/min for UC3 sample. Solid line indicates weight % and dashed line indicates first derivative, showing maximum weight loss at ~372°C.

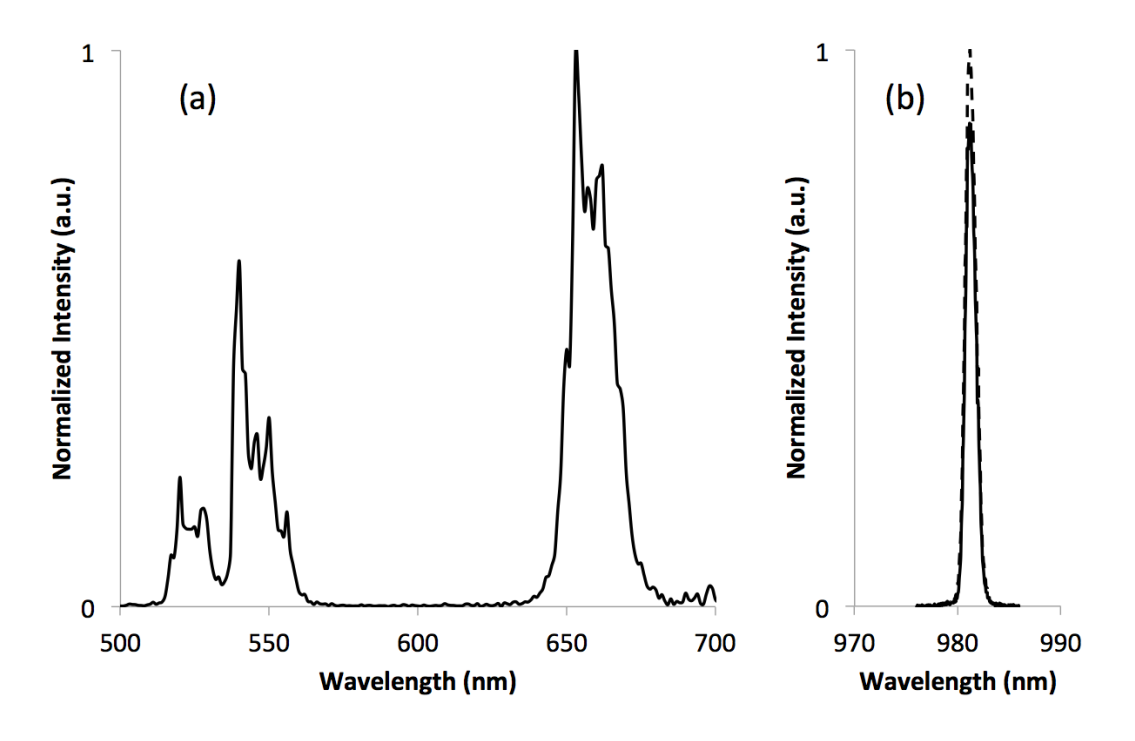


Figure A.3: Quantum yield raw data for (a) visible upconversion under 50W/cm<sup>2</sup> NIR excitation and (b) NIR laser profile shown for sample (solid line) and reference (dashed line). Data taken from UC3 hydrothermal sample.

#### **Appendix B: Chapter 4 Supporting Information**

The annealing profile is as follows: the electrode was heated from room temperature to  $150\,^{\circ}\text{C}$  at a rate of  $120\,^{\circ}\text{C}/\text{hr}$  and held for  $15\,^{\circ}\text{min}$ , then to  $325\,^{\circ}\text{C}$  at a rate of  $240\,^{\circ}\text{C}/\text{hr}$  and held for  $5\,^{\circ}\text{min}$ , then to  $375\,^{\circ}\text{C}$  at a rate of  $120\,^{\circ}\text{C}/\text{hr}$  and held for  $5\,^{\circ}\text{min}$ , and finally to  $450\,^{\circ}\text{C}$  at a rate of  $60\,^{\circ}\text{C}/\text{hr}$  and held for  $30\,^{\circ}\text{min}$ . After this, was cooled to room temperature at a rate of  $60\,^{\circ}\text{C}/\text{hr}$ . The profile is shown in Figure B.1.

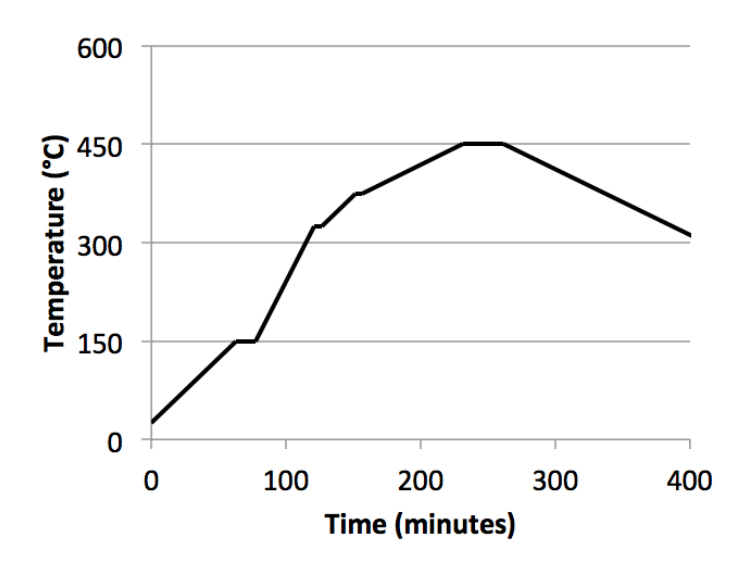


Figure B.1: Heating profile for the DSSC annealing process

The scattering efficacy of the various  $UC@TiO_2$  devices is demonstrated by the degree of transparency as illustrated in the digital photographs shown in Figure B.2. The degree of transparency decreases as the amount of  $TiO_2$  increases (i.e. UC to UC@T1 to UC@T2) demonstrating higher degrees of light scattering in the films with higher amounts of  $TiO_2$ .

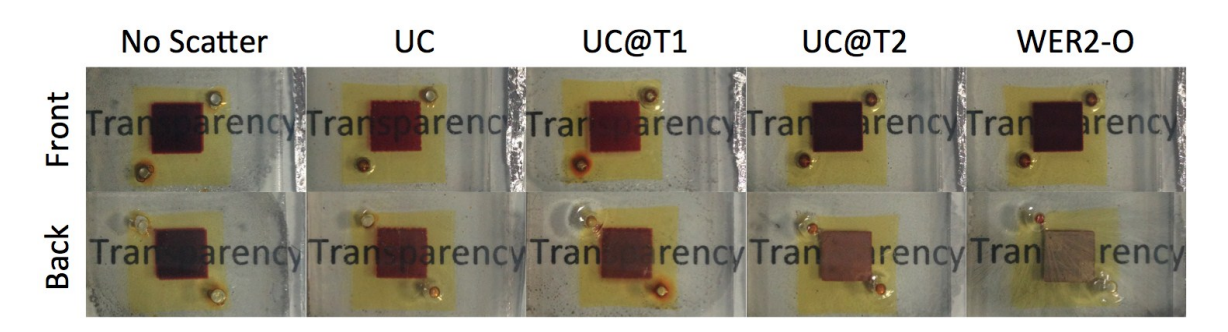


Figure B.2: Digital photographs illustrating the effect of scattering on the transparency of the DSSCs as observed from the front (photoanode) side and the back (counter electrode) side

# Appendix C: Y<sub>3</sub>Al<sub>5</sub>O<sub>12</sub>:Yb<sup>3+</sup>,Er<sup>3+</sup> Upconversion Study

Yttrium aluminum garnet ( $Y_3Al_5O_{12}$ , YAG) is often used as an optical host material for lasers and phosphors, however little research has been devoted to using it as an upconversion host material. A short study was conducted to elucidate the optimal doping profile for YAG doped with the Yb<sup>3+</sup>,Er<sup>3+</sup> upconversion couple replacing Y<sup>3+</sup> in the material lattice.

YAG was prepared by co-precipitation of hydroxide precursors from an aqueous solution of metal nitrate salts. The concentration of metal ions in solution was in stoichiometric ratio (i.e. Y:Al:Er:Yb = 3\*(1-x-y):5:3x:3y) and were precipitated using an appropriate amount of ammonium hydroxide to bring the solution to a pH of  $\sim$ 9.7. The precipitate was filtered and washed with water and ethanol and subsequently dispersed in anhydrous ethanol using an ultrasonic horn. The dispersed solution was transferred to a stainless steel autoclave and treated solvothermally at 280 °C for 2 hours with a 2°/min ramp rate. The resulting precipitate was separated by centrifugation and washed 3 times with deionized water and once with ethanol.

The doping levels were varied using 18% Yb³+, 2% Er³+ as the central point, based on the optimal doping of NaYF₄. All doped samples were separated into equal portions and annealed for 2 hours at 800, 1000 and 1200 °C to increase upconversion. Upconversion fluorescence was measured using a similar method as that listed in Chapter 3 with results tabulated in Table C.1 and shown graphically for the as-is samples and those annealed at 800 and 1000 °C in Figure C.2. Additionally, a sample upconversion spectrum is provided in Figure C.1 using YAG:18%Yb,1%Er annealed at 1200 °C.

Table C.1: Raw integrated intensity values for all YAG:Yb,Er samples studied

Annealing	Doping		Integrated Intensity (a.u.)		Green-to-	
Temperature (°C)	Er <sup>3+</sup> (at%)	Yb <sup>3+</sup> (at%)	Green	Red	red Ratio	
	2	12	2.80E+04	4.24E+04	0.66	
		18	9.83E+03	1.42E+04	0.69	
As-is		24	1.94E+04	3.27E+04	0.59	
A5-15	1		1.23E+04	2.19E+04	0.56	
	2	18	9.83E+03	1.42E+04	0.69	
	4		6.19E+03	1.17E+04	0.53	
	2	12	9.64E+04	1.35E+06	0.07	
		18	7.90E+04	1.61E+06	0.05	
800		24	5.59E+04	2.95E+06	0.02	
800	1		6.15E+04	2.97E+06	0.02	
	2	18	7.90E+04	1.61E+06	0.05	
	4		2.62E+04	4.84E+05	0.05	
	2	12	9.17E+05	1.91E+07	0.05	
		18	4.58E+05	1.98E+07	0.02	
1000		24	4.09E+05	2.34E+07	0.02	
1000	1		4.52E+05	2.13E+07	0.02	
	2	18	4.58E+05	1.98E+07	0.02	
	4		1.90E+05	6.79E+06	0.03	
	2	12	4.45E+06	4.93E+07	0.05	
		18	3.48E+06	6.66E+07	0.02	
1200		24	3.46E+06	8.80E+07	0.02	
1200	1		3.98E+06	7.37E+07	0.02	
	2	18	3.48E+06	6.66E+07	0.02	
	4		4.43E+06	7.20E+07	0.03	

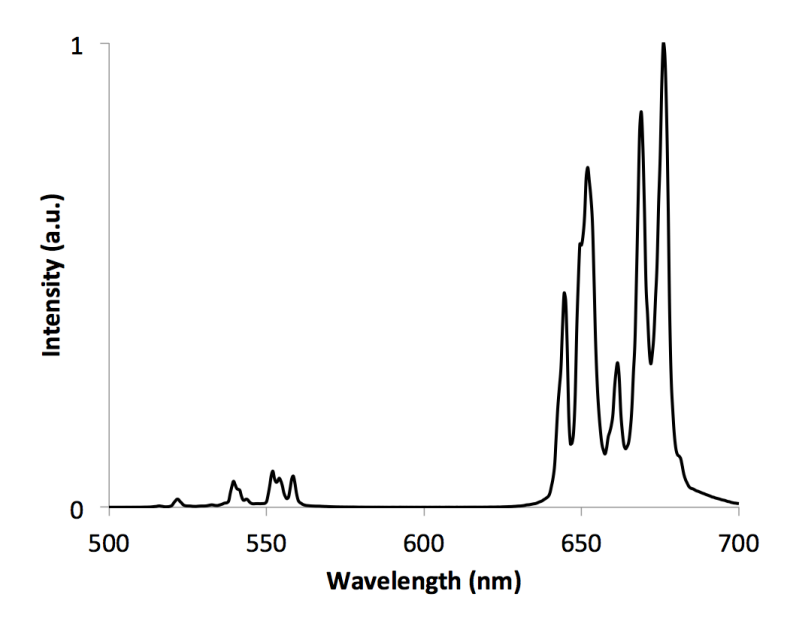


Figure C.1: Upconversion fluorescence spectrum under NIR laser illumination (980 nm) for YAG:18%Yb,1%Er annealed at  $1200\,^{\circ}$ C for 2 hours

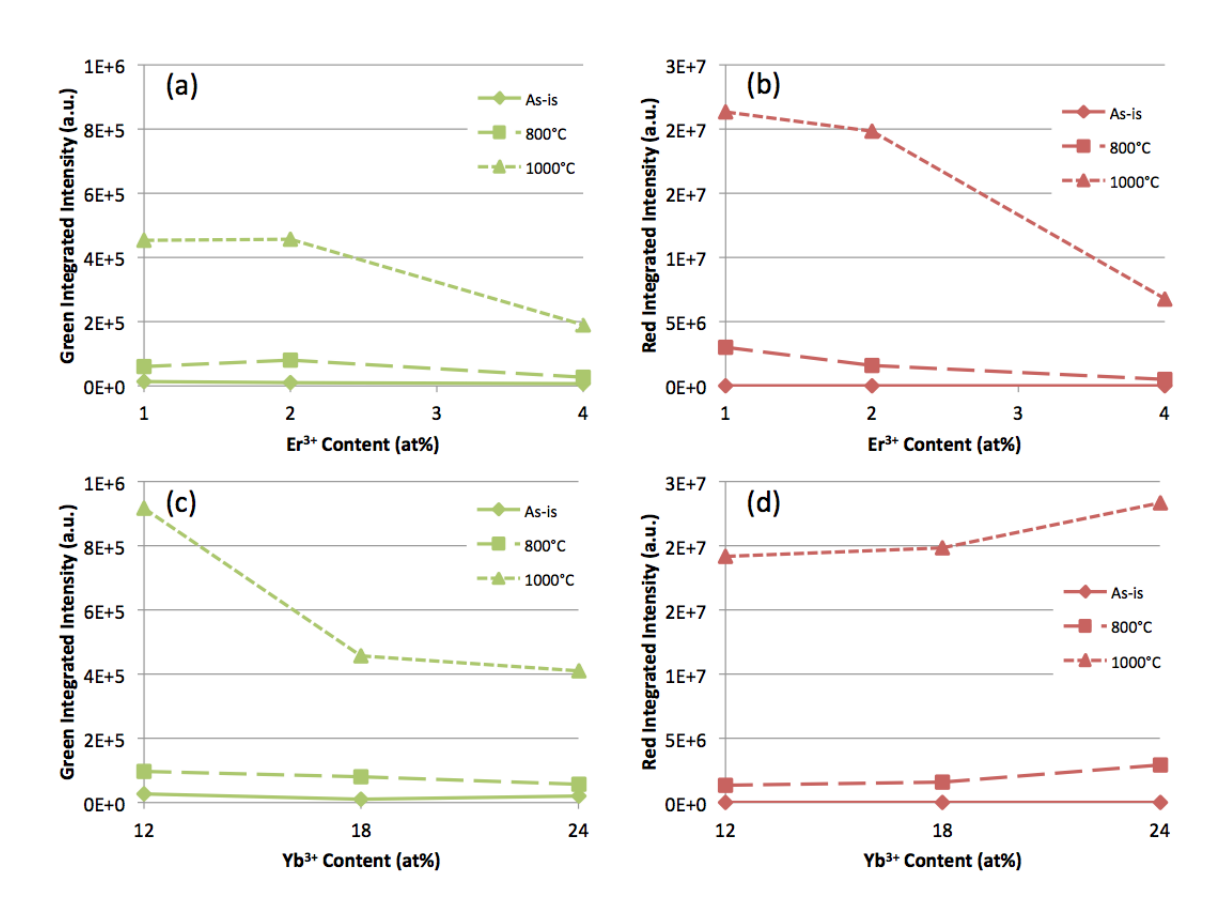


Figure C.2: Integrated upconversion fluorescence values for YAG (a,b)  $Er^{3+}$  doping study and (c,d) Yb<sup>3+</sup> doping study for as-is samples, and samples annealed at 800 and 1000 °C.

From the plots in Figure C.2, it is easiest to see that the optimal doping profile for green upconversion is 12%Yb, 2%Er, while the optimal doping profile red upconversion is 24%Yb, 2%Er. While annealing significantly increases the upconversion fluorescence, the spectral profile is dominated by upconversion to red in all samples, and is not favourable for integration into DSSCs. This is due to relatively high phonon energy of the YAG lattice (see Chapter 2). It should be noted that for the Er doping study, a drop in upconversion is observed at higher doping levels (4%). This is due to cross-relaxation processes that quench the upconversion luminescent processes when the emitting Er<sup>3+</sup> ions are too close in proximity in the crystal lattice.

Despite the increase in upconversion that arises due to doping, the highest green emission is still orders of magnitude lower to similar samples prepared in our lab using the  $NaYF_4$  host lattice. For this reason, these materials were not investigated further for integration into DSSCs.

# Appendix D: Application of External NaYF<sub>4</sub>:Yb<sup>3+</sup>,Er<sup>3+</sup> Upconversion Layers to DSSCs

A short study was conducted, attempting to integrate NaYF<sub>4</sub>:Yb<sup>3+</sup>,Er<sup>3+</sup> upconversion materials as a simple rear reflection layer in DSSC devices. The upconversion materials were prepared using the same procedures presented in Chapter 3 (UC1, UC2, and UC3 types). The powders were annealed at 600 °C for 2 hours, producing highly fluorescent upconversion phosphors. The upconversion fluorescence spectra of the samples are presented in Figure D.1.

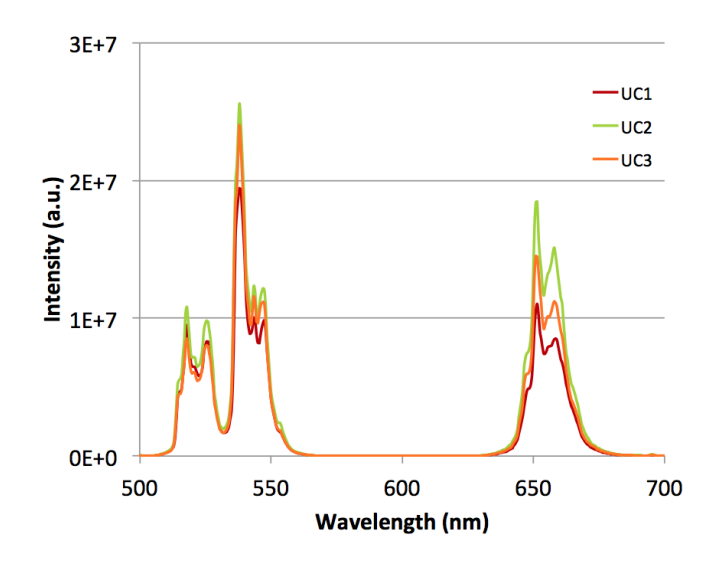


Figure D.1: Upconversion fluorescence spectra of annealed samples under NIR laser illumination (980 nm)

The DSSC devices were prepared using a similar procedure to the one presented in Chapter 4 (See Section 4.3.2) with minor alterations. In this case, DSSC photoanodes were produced using a doctor blade method in place of screen printing. A piece of tape was applied to the cleaned FTO glass surface to define the active area. The nanocrystalline  $TiO_2$  paste (18NR-T, Dyesol) was applied and spread using a hard rubber "blade" such that the thickness of the layer was dictated by the tape thickness. This resulted in printed layers of about 12  $\mu$ m. All other steps are identical to those described in Section 4.3.2.

The upconverting rear reflection layers were made by producing a paste using a procedure published elsewhere [1], [2]. A layer was deposited onto a glass microscope slide using the doctor blade method, using 6 layers of tape to define the thickness. The upconverting layers were then annealed using the same annealing profile listed in Figure B.1, Appendix B. Following this, the annealed layers were protected by glass coverslips in order to protect against scratches.

The UC layers were alternatively placed against the rear of the DSSC device (see Figure D.2(a)) and the performance of the resulting devices were measured using simulated solar light. The PV characteristics are tabulated in Table D.1 and the JV characteristics are shown in Figure D.2(b).

Table D.1: PV Characteristics of DSSC devices with external upconversion layers

Rear Layer	UC Crystal Size	Efficiency (%)	$J_{sc}$ (mA/cm <sup>2</sup> )	V <sub>oc</sub> (V)
Control	N/A	6.33	12.37	0.764
UC1	2.3 μm	6.39	12.61	0.761
UC2	700 nm	6.45	12.78	0.760
UC3	300 nm	6.43	12.76	0.759

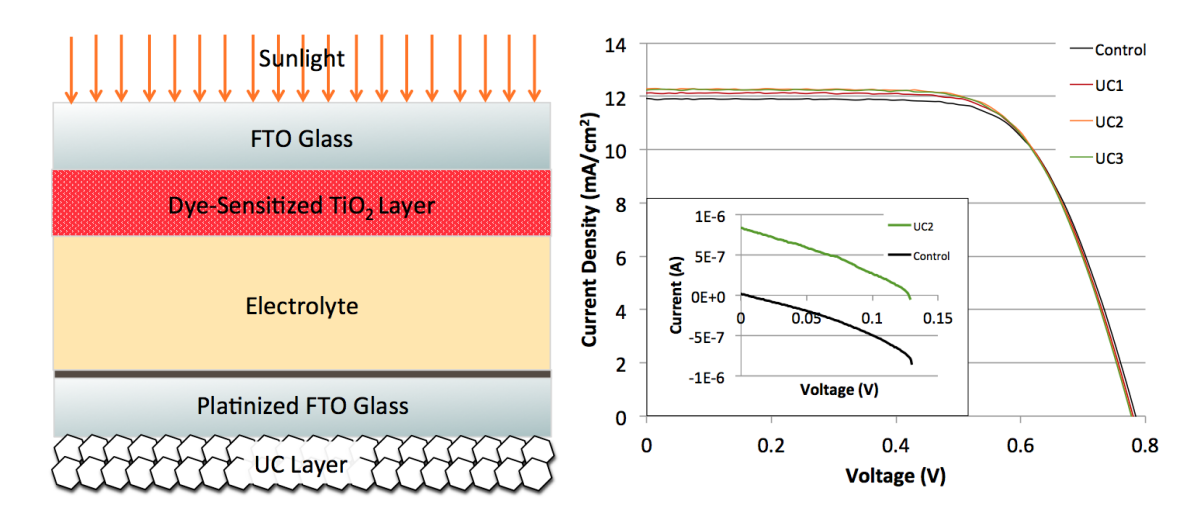


Figure D.2: (a) Schematic illustrating structure of DSSC device and position of the external upconversion (UC) layer, and (b) the JV characteristics of the DSSC devices with proof-of-concept performance under NIR laser illumination shown inset.

As a result of the upconverting rear reflection layers, a marginal increase in photocurrent was attained, representing an average improvement of only 1.015

times the conversion efficiency of the DSSC devices. The inset of Figure D.2 shows the proof-of-concept upconverting performance under illumination with a 980 nm NIR laser. The performance increases observed are marginal. It was for this reason that the internal layer approach presented in Chapter 4 was taken. It was hypothesized that some of the upconverted light was lost due to reflection and absorbance from the platinized counter electrode, electrolyte, and multiple glass interfaces, and that moving the upconverting layer into the cell would help increase potential coupling of upconverted light to the actual solar cell device.

#### References:

- [1] C. Charbonneau, R. Gauvin, and G. P. Demopoulos, "Aqueous Solution Synthesis of Crystalline Anatase Nanocolloids for the Fabrication of DSC Photoanodes," *Journal of The Electrochemical Society*, vol. 158, no. 3, p. H224, 2011.
- [2] S. Ito and P. Chen, "Fabrication of screen-printing pastes from TiO<sub>2</sub> powders for dye-sensitised solar cells," *Progress in Photovoltaics: Research and Applications*, vol. 15, no. May, pp. 603–612, 2007.